Development of a non-assembly 3D printed driving mechanism for a vitreous cutter

by

Maarten Jacob Stolk

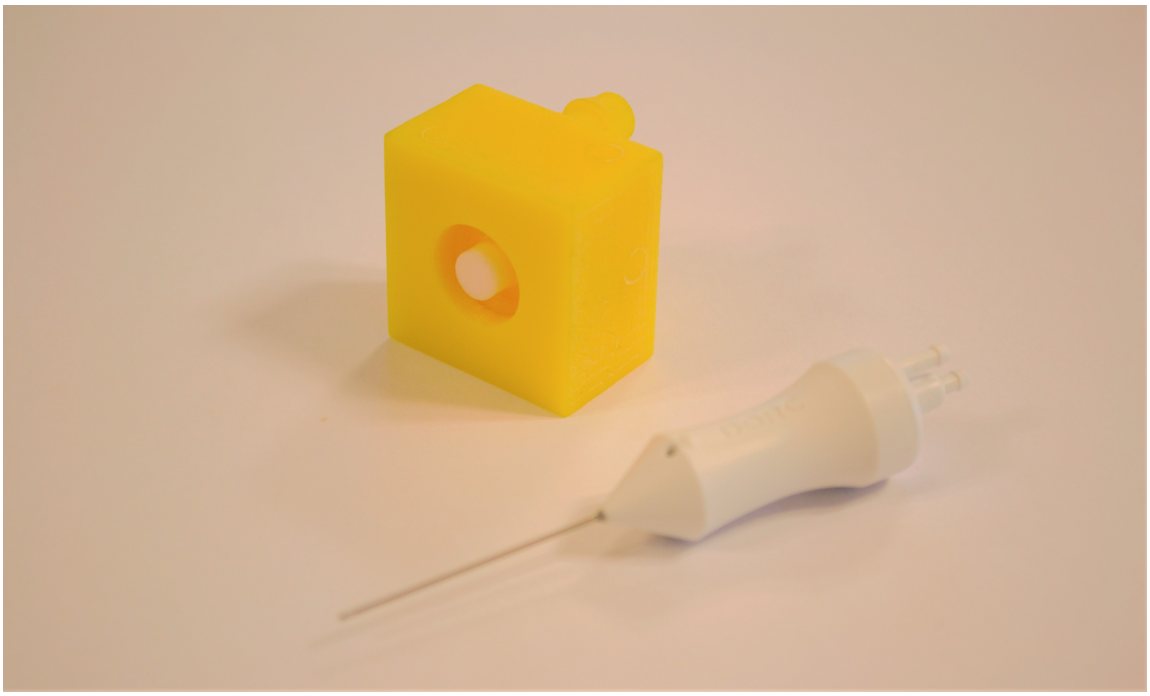

Supervisor TU Delft : Kirsten Lussenburg
Supervisor DORC: Marta Scali

BITE (Bio-Inspired Technology Group)
Technische Universiteit Delft
Delft, The Netherlands
September 15, 2020

TU Delft Delft University of Technology

DORC

Development of a non-assembly 3D printed driving mechanism for a vitreous cutter

by

Maarten Jacob Stolk

To obtain the degree of Master of Science
at the Delft University of Technology,
to be defended on Friday September 25, 2020

Student number: 4276647

Thesis committee: Prof. dr. ir. P. Breedveld, TU Delft
ir. K. M. Lussenburg, TU Delft
ir. M. Mirzaali Mazandarani, TU Delft
dr. ir. M. Scali, DORC International

Abstract

Background During a vitrectomy procedure vitreous is removed from the eye with a vitreous cutter, called a vitrectome. This instrument is comprised of two needles that move to cut the vitreous into small pieces before aspirating them. Vitreous cutters are complex instruments that are light and small in size to increase their accuracy. Because of their small size, and complexity, they are assembled by trained technicians with the help of a microscope. It is believed that new technologies such as additive manufacturing (AM) might be able to reduce the manufacturing complexity associated with vitreous cutters. The goal of this study was therefore; ”To create a non-assembly driving mechanism for a vitreous cutter that is designed for AM”.

Method In order to achieve this goal, the functions of a vitreous cutter were identified, as well as the mechanisms that fulfil these functions in current instruments. Furthermore, the general limitations of AM were researched and listed. Extensive research was done to identify examples in the scientific literature to find linear actuators that were made by means of AM as an integrated assembly. A diaphragm actuator was selected to drive the mechanism based on the limitations of AM, the requirements, and examples found in the scientific literature. An in depth analysis of diaphragm driven vitreous cutters revealed that it would be a challenge to seal the air chamber of the instrument. A new concept was created that used one of the strengths of AM to solve this problem, by creating a compliant interface between the moving needle and the air chamber. A proof of principle prototype was created to quickly test if it would be possible to create movement by sealing the air chamber with differently sized diaphragms. Based on the concept of sealing an air chamber with flexible diaphragms, four concept variations were created. It was decided to make a series of prototypes of one of these concept variations to study its performance. In total, 9 prototypes were manufactured using material jetting, out of Agilus30 and Vero, without the need of post-assembly. The prototypes were tested by applying a range of air pressure pulses, while measuring the force, the displacement, the actuation time, and the spring properties of the mechanism.

Results With the successful manufacturing of the prototypes, it has been shown that it is possible to produce the novel driving mechanism using current AM techniques without any assembly steps other than the sealing of a cleaning hole to remove support material. The tests revealed that the spring force of the mechanism was not linear for all materials, and that there was hysteresis present in the mechanism.

Furthermore, it was shown that none of the samples were capable of operating at the desired speed of 8000 pulses per minute (PPM). The soft samples were seen to have the best response time during the backward motion of the mechanism.

Conclusion A new driving mechanism was created in this study that utilized one of the strengths associated with AM. To the knowledge of the author this mechanism is the first of its kind, and has not been previously applied in another instrument. Additional knowledge on the material properties of digital materials is needed to be able to design a diaphragm mechanism that has the appropriate performance characteristics. With additional design efforts and research it could be possible to produce vitreous cutters using AM in a non-assembly manner. This could lead to a future where surgical instruments are manufactured on site and on demand.

Contents

1. Introduction

1.1. Background

Pars plana vitrectomy (PPV) is one of the most commonly executed eye surgeries used to restore, or improve vision in patients with diseases related to the posterior segment of the eye, such as: diabetic rethinopathy, retinal detachment, vitreous hemorrhage, a macular pucker, a macular hole, or floaters. In the Netherlands, in the year 2017, 2.89 % of the population was diagnosed with a condition of the posterior of the eye [1]. This illustrates the importance of research related to vitreous surgery, and how innovations within this field can have a large impact on healthcare in general.

PPV is the procedure where some or all of the vitreous humour is removed from the posterior segment of the eye. PPV is almost always executed before any intra-ocular posterior surgery, to minimize the disturbance to healthy posterior eye structures. The vitreous body is a jelly-like, transparent substance that gives support to the eye and shapes it. It also limits relative movement between the retina and the anterior eye structures during eye and head movements [2]. Vitreous humour is comprised of water (99%), and a collagen fibre network intermixed with hyaluronan (1%) [3], [4]. The collagen fibre network gives vitreous its characteristic jelly-like structure and accompanying mechanical properties. The vitreous is attached to the retina by the vitro-retinal interface. This interface consists of the inner limiting membrane of the retina (ILM), posterior vitreous cortex, and extracellular matrix [2]. PPV is conducted by an ophthalmic surgeon using a vitreous cutter under local or general anaesthesia [5], [6]. The name pars plana vitrectomy originates from the area through which the instruments are inserted that are used during surgery. The pars plana does not contain retinal tissue, and is relatively avascular when compared to other eye structures. This makes it suitable for instrument insertion and therefore, an important surgical landmark [7]. A photograph of a cross section of a human eye is shown in Figure 1. It shows the pars plana highlighted in red, as well as other anterior and posterior eye structures.

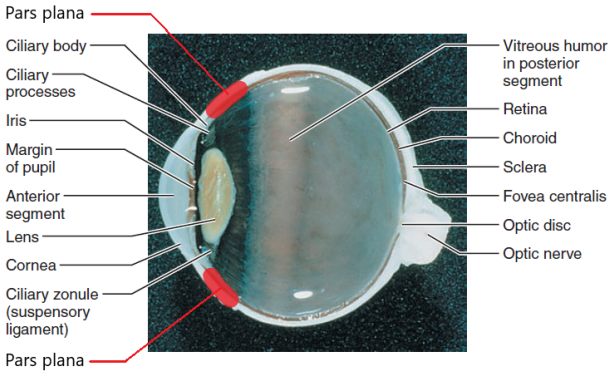

Figure 1. Photograph of the cross section of a human eye, showing the most important anatomical structures. The pars plana is highlighted in red. Adapted from: [8].

The vitreous cutter is inserted into the eye through a trocar port, which is placed in the pars plana of the eye. During surgery, at least two additional trocars are placed: one for an endo-illumination instrument, and one which is connected to a source of saline solution. The endo-illumination probe serves as a light source for the user and allows the surgeon to look into the eye of the patient. The saline solution is used to replace the removed vitreous, and has the function of keeping the intra-ocular pressure at around 20 mmHg during the procedure [9], [10]. A vitrectomy is performed in two steps. The first step consists of removing the central part of the vitreous, this is also called the ”core vitrectomy”. The second step of the surgery focuses on the removal of the vitreous in the more peripheral areas close to the retina. This is also known as ”retinal shaving”. Typically the surgeon uses a high cut rate combined with a low aspiration pressure when performing retinal shaving. This intends to minimize the risk of a retinal detachment when removing the vitreous close to the retina. The surgeon looks through a microscope while performing the surgery. A lens placed on top of the eye can be used to further enhance the vision of the surgeon into the eye. A photo taken during a vitrectomy surgery is shown in Figure 2.

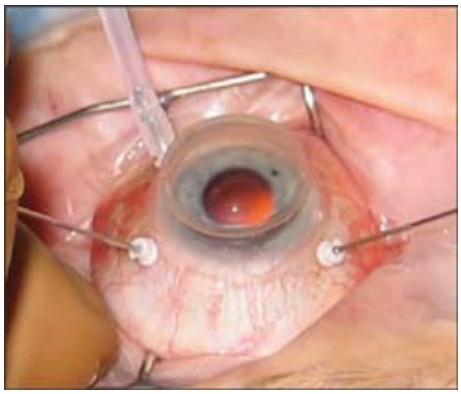

Figure 2. Photo of the eye of a patient during a vitrectomy surgery. Clearly visible are the trocar ports through which instruments are inserted into the eye. Also the magnifying lens on top of the eye, which serves to enhance the view of the surgeon, can be observed. The tube providing saline solution into the eye is also visible. Adapted from: [11]

1.2. Problem Definition

One of the biggest challenges with regards to vitreous cutting instruments is the manufacturing process. Because of their small size and high complexity, vitreous cutters are currently assembled by hand, by trained technicians with the help of a microscope. Therefore, it is a slow and costly process to produce the widely used instruments. When looking at the available information on vitreous cutters in the scientific literature, the focus tends to be on the cutting speed of the instrument, the duty cycle of the instrument, the size of the outer tube, and the aspiration flow rate [12]–[14]. It is understandable that there is a desire to compare these aspects between vitreous cutters, as they are related to the clinical performance of the instrument. However,

little information can be found in the scientific literature on different manufacturing techniques, and the different driving mechanisms of vitreous cutters. It is therefore relevant to conduct more research into these topics as they have not been addressed previously.

New manufacturing techniques such as additive manufacturing (AM) could provide a possible solution to the problem of the high manufacturing complexity associated with vitreous cutters. AM has the ability to produce components that are not possible to produce using conventional techniques, and even to produce entire functional mechanisms [15]–[17]. Functional mechanisms that are produced in a single production step without the need of subsequent assembly steps are referred to as "non-assembly" mechanisms. It would be ideal if future vitreous cutters would be non-assembly instruments, as it would greatly simplify their manufacturing process by removing the need for trained technicians to assemble the instrument. It is indicated in the literature that non-assembly mechanisms are especially suited to be manufactured with AM technologies due to the versatility of the technology [18]. However, before vitreous cutters can be produced in a non-assembly manner using AM, a new design has to be made to facilitate this production process. To the knowledge of the author there have not been previous studies that explore the possibility of creating a non-assembly vitreous cutter.

1.3. Goal of this study

The goal of this study is as follows: "To create a non-assembly driving mechanism for a vitreous cutter that is designed for AM". Because of the limited resolution of current AM techniques it was not deemed feasible to manufacture the needles of the instrument using AM [19]. A set of 5 sub-questions have been formulated to break down the goal in several parts:

1) What are the functions of a vitreous cutter?
2) What are the mechanisms that can perform the functions of a vitreous cutter?
3) What characteristics do driving mechanisms for vitreous cutters need to have to make them suitable for non-assembly AM?
4) What AM processes are available, and which would be most suitable to produce a non-assembly driving mechanism for a vitreous cutter?
5) How do non-assembly AM driving mechanisms for vitreous cutters perform in comparison to conventionally manufactured driving mechanisms?

1.4. Layout of this study

This study is divided into eight sections. The first section contains the introduction and general background information on PPV, the problem definition, as well as the goals. An in depth description and functional analysis of a current vitreous cutter are given in section two. The third section describes the different types of linear pneumatic actuators, and provides examples of these actuators that were produced using AM. A schematic overview is given of all currently known AM methods, and the processes that were used to manufacture the discussed examples. The general limitations of AM are also mentioned in this section. The requirements of the new driving mechanism are provided in Section four, along with a description of the concept development process. Section five discusses the details of producing 9 prototypes which were used in testing. To evaluate the performance of the driving mechanism a series of tests were conducted. The methods, results, and aim of the tests are discussed in Section six. Section seven contains the discussion and reflects on the results described in the previous sections, recommendations for further research are made, and limitations of the current study are indicated. A complete design of a non-assembly vitrectome is also presented. Section eight contains concluding remarks that intend to summarize the findings of this study.

2. Vitreous Cutter Analysis

2.1. State of the Art Vitreous Cutter

Vitreous cutters are also known as vitrectomes, they contain a cutting mechanism to minimize the disturbance to the retina and other posterior structures during vitreous removal. Vitreous cutters are small, highly specialized instruments, that have mechanisms that allow them to make up to 16,000 cuts per minute [20]. A vitreous cutter consists of: a needle section, and a handle with connection ports. An image of a vitreous cutter is shown in Figure 3.

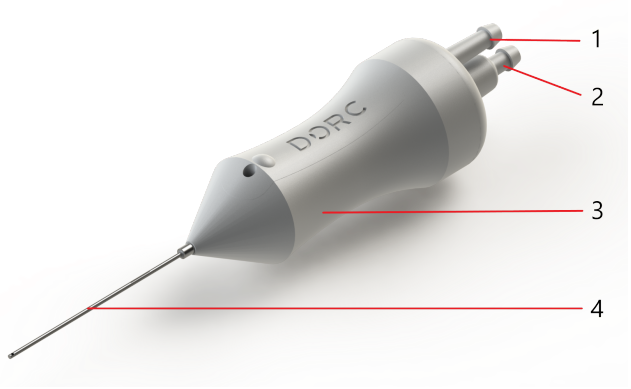

Figure 3. Photo of a vitreous cutter, with numbered components: 1. Pressurized air inlet, 2. Connection to vacuum source 3. Handle with internal drive mechanism, 4. Concentric needles. (DORC International, Zuidland)

The needle portion consists of two concentric hollow needles, where the inner needle can be moved and the outer needle is rigidly fixed to the handle of the instrument. A small opening is located at the distal tip of the outer needle (cutting port), through which vitreous can be aspirated into the instrument by means of an applied vacuum. A photo of the cutting port can be seen in Figure 4.

The cutting mechanism operates by partially sucking in a piece of vitreous through the cutting port. Subsequently, the inner tube is moved in such a way that it closes the port. This creates a shearing action between both needles,

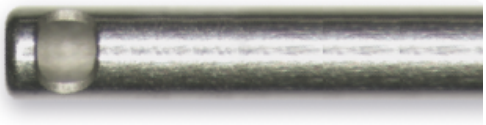

Figure 4. Photo showing the cutting port of a vitreous cutter located in the distal tip of the outer needle. Adapted from: [21]

which cuts off a small piece of vitreous. The severed piece of vitreous then travels through the hollow inner needle to an external collection vessel.

To increase the cutting speed of vitreous cutters, two dimensional cutters (TDC) have been introduced. A TDC has a second cutting port located at the tip of the inner cutting needle, this allows the cutter to cut in both the forward and backward directions. Another benefit of TDC cutters is that the aspiration flow remains more constant and is independent from the cut rate. In Figure 5 a schematic comparison is shown between a TDC and a conventional cutter.

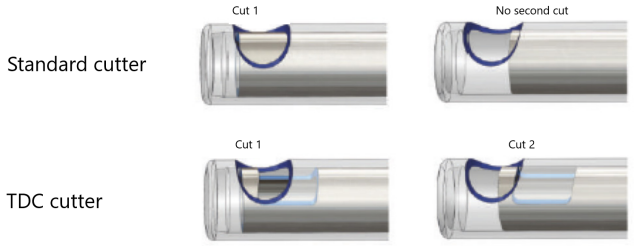

Figure 5. Schematic drawings of the cutting ports of a TDC, and standard cutter. Showing that a TDC cutter cuts on both the forward and backward motion. Adapted from: [22]

The inner cutting needle is driven by a driving mechanism which is located inside the handle of the instrument. There are a variety of different driving mechanisms that are able to generate movement of the cutting needle. Even the type of movement of the inner needle can be varied. Three types of movement have been identified that are able to generate a shearing action between two concentric needles: translation, rotation, and simultaneous translation and rotation. In a previous study an overview was created of all the patented driving mechanisms of vitreous cutters. Each unique driving mechanism was classified according to the output and engine type of the driving mechanism. A schematic overview of this classification is shown in Figure 6. In Appendix A, each unique driving mechanism that was found in the patent literature is described. The most common driving mechanism uses a diaphragm to generate a translating motion of the cutter, in response to air pressure pulses that are applied to the instrument from an external source. A schematic drawing of such a diaphragm mechanism is shown in Figure 7.

The inner cutting needle is attached to the diaphragm, which moves in response to air pressure pulses that are applied to one side of it. This generates the forward movement of the cutting needle. The backward motion is generated by a compression spring in between the diaphragm and the housing. This driving mechanism is therefore referred to as ”spring biased”. There are also instruments on the market that use a diaphragm mechanism that is able to receive pressure pulses on both sides. This eliminates the need for a return spring. A schematic drawing of such a dual actuated diaphragm mechanism is shown in Figure 8. In both driving mechanisms o-ring seals are used to seal the gap between the housing and the cutting needle. This ensures that the diaphragm can be pressurized appropriately, without inhibiting the motion of the cutting needle. An external control system supplies the air pressure pulses, and the vacuum to aspirate the vitreous. The instrument is connected to the control system via flexible tubing. The control system can receive input from the user to set the speed of the cutter,

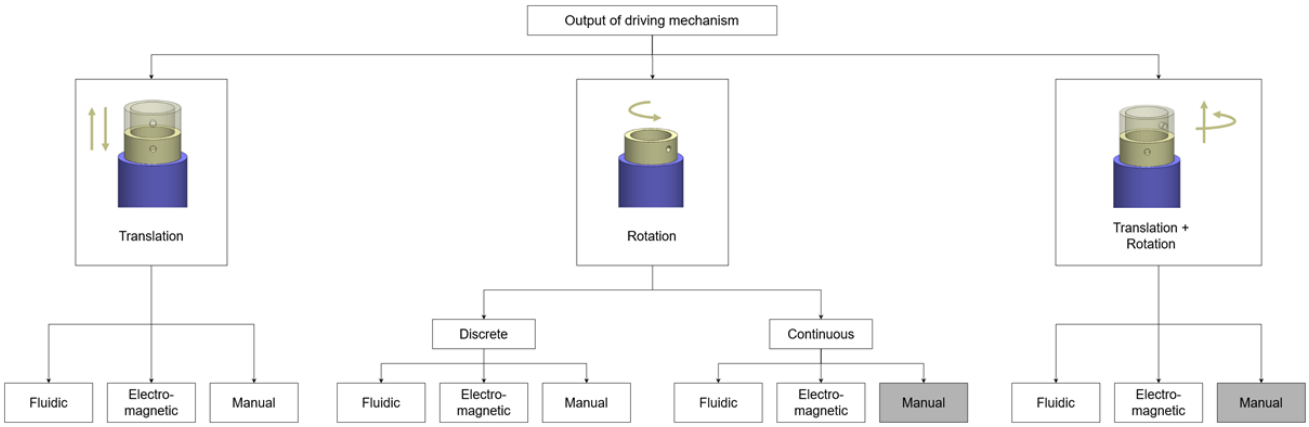

Figure 6. Schematic representation of all the patented cutting needle movements along with the engine types used to in the driving mechanisms that drive these cutting needles. The grey color indicates that no patents were found in a particular category.

as well as the strength of the applied vacuum. Depending on the construction of the instrument other aspects could also be changed such as: the stroke length of the cutter, or the duty cycle (ratio between the amount of time the cutting port is open, and the total duration of a cutting cycle).

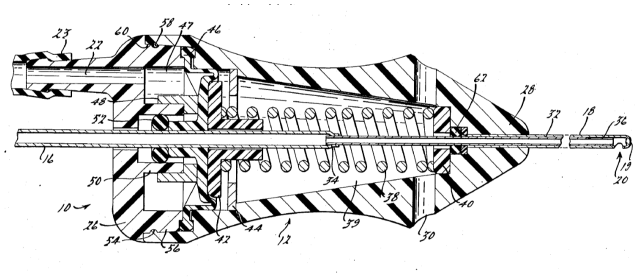

Figure 7. Schematic drawing of the most commonly used driving mechanism for vitreous cutters. Components: 16 = connection tube between diaphragm and cutter, 22 = inlet for pressurized air, 38 = Compression spring, 42 = Force distributor for spring, 46 = Diaphragm, 47 = air-chamber, 52 = rear O-ring seal, 62 = front O-ring seal. Adapted from: [23]

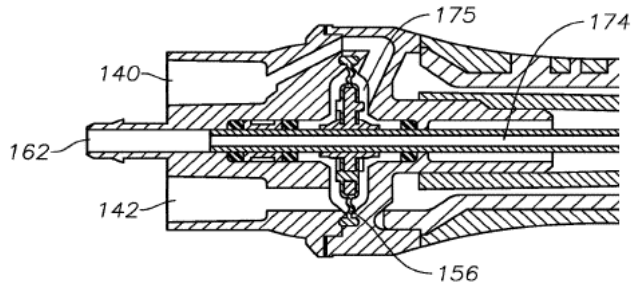

Figure 8. Schematic drawing of a dual actuated diaphragm mechanism. Components: 140 = pressurized air inlet backward movement, 141 = pressurized air inlet forward movement, 156 = diaphragm, 162 = connection to vacuum source, 174 = lumen inner cutting needle, 175 = air chamber. Adapted from: [24]

2.2. Instrument specifications

The specifications of a vitreous cutter that is currently sold are used as a base for the design requirements of the new driving mechanism. The specifications of the 8268.VIT23 instrument, manufactured and sold by D.O.R.C International (Zuidland, the Netherlands) are used. The instrument uses a spring biased driving mechanism and is equipped with TDC cutting needles. The specifications of this instrument are listed in Table 1. Only the specifications that were deemed to be relevant for this study are listed.

2.3. Functional Analysis

To understand the underlying principles that define the design of the current vitreous cutters, a functional analysis was performed. First the main function of the instrument as well as it's inputs and outputs were defined. Two types of inputs were observed: power and material. The only output

TABLE 1. SPECIFICATIONS OF DORC 8268.VIT23 TDC VITREOUS CUTTER

Specifications 8268.VIT 23 TDC	
Description	Value
Cutting speed (max)	16000 [CPM], 8000 [PPM]
Cutting speed (min)	0 [CPM]
Cutting force forward cut	9 [N]
Cutting force backward cut	8 [N]
Movement type used for cutting	Translation
Aspiration pressure (max)	660 [mmHg]
Aspiration pressure (min)	Atmospheric pressure
Dimensions of cutting port in outer needle, length x width	0.40 [mm] x 0.42 [mm]
Dimensions of cutting port in inner needle, length x width	0.43 [mm] x 0.40 [mm]
Stroke length of inner needle assembly	0.8 [mm]
Weight of instrument	5 [g]
Dimensions of handle, length x width (max)	40 [mm] x 16 [mm]

of the instrument, is the separated vitreous. A schematic representation of the functional analysis is shown in Figure 9.

The instrument receives power from a control system to drive the inner needle, this is referred to as "power for actuation". The reason that current instruments use pressurized air from an external source is to keep the instrument as light as possible. Previous instruments used internal electromagnetic means to actuate the needle. However the weight of these instruments was much greater than the current pneumatic instruments [10]. The low weight of the instrument increases the positional accuracy of the instrument within the eye, as well as its usability. The surgeon manually positions the vitreous cutter inside the eye during the procedure. Therefore, manual power is applied to the instrument to position it. The handle is shaped in such a way that it enhances the grip of the user, this helps to prevent unintentional dropping or slipping of the instrument. The only material flow that is observed, is that of the vitreous. It enters the instrument when it is attached to the retina, and comes out as small fragmented pieces. The inputs and outputs serve the main function of the instrument which is: *to remove the vitreous from the eye*.

In Figure 10, a second schematic of the functional analysis is presented, showing the lower level functions of the instrument. The functions are shown in a hierarchical manner, the main function is shown on the left, and on the far right, the lowest level functions are shown. In order to remove the vitreous in a safe manner during a vitro-retinal procedure, there are additional considerations than when the vitreous would be removed full stop. The sub-functions directly below the main function of removing the vitreous were determined to be:

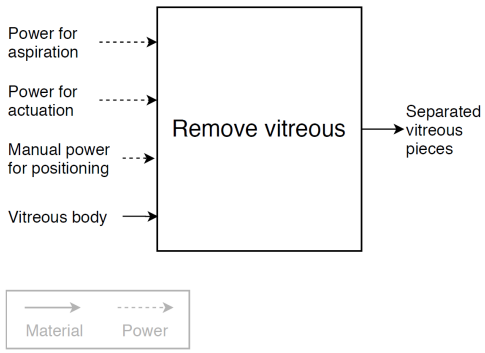

Figure 9. Schematic representation showing the main function of a vitreous cutter and the power and material going in and out of the instrument.

- *Providing access to the vitreous*
- *Preventing harm to the patient*
- *Decoupling the vitreous*
- *Transporting the vitreous*

The access to the vitreous is provided through a trocar port in current vitro-retinal surgeries. The thin needles of the vitreous cutter can pass through this port and remove the vitreous without causing a large amount of trauma to the patient.

The second sub-function is related to minimizing the damage to the patient. In order to achieve minimal damage, the instrument should be bio compatible and able to be sterilized. The trauma to the patient can be further mitigated by minimizing the wound size which is required to insert the instrument, this is closely related to the sub-function of providing access to the vitreous. In order to remove the vitreous safely from the eye, it is important to minimize the force that is applied to the retina to prevent retinal detachment. The collagen fibres inside the vitreous are attached to the retina and therefore, the vitreous can't be simply sucked out. The suction force would be directly transmitted to the retina and could potentially cause severe damage. One of the most important sub-functions of a vitreous cutter is therefore, to decouple the vitreous from the retina. Current vitreous cutters achieve this by separating a small piece of vitreous from the main vitreous body before aspirating it. Vitreous cutters use the shearing action between the cutting ports of the inner and outer cutting needles to separate a piece of vitreous. A translating motion of the inner cutting needle is used to generate this shearing action. In the past there have also been vitreous cutters that use a rotating motion of the inner needle to cut the vitreous. However, a negative side effect occurred in these rotary cutters, as the collagen fibres wound up around the cutter instead of being severed. This led to the exertion of large traction forces on the retina and caused retinal detachments [10].

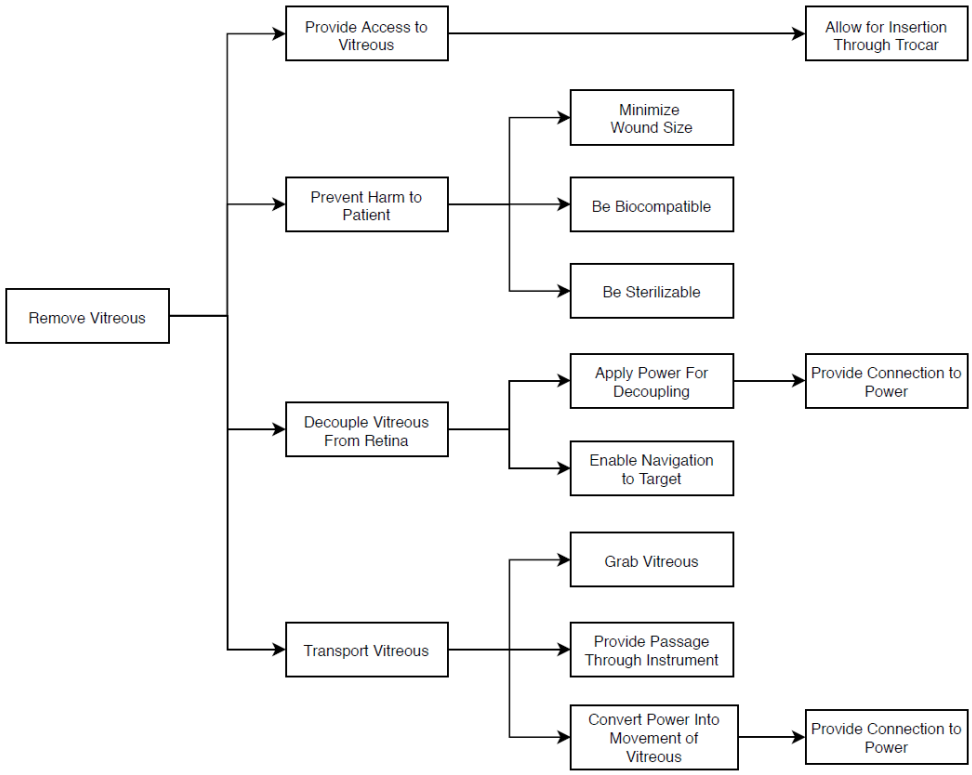

Figure 10. Schematic representation of the low level functions of a vitreous cutter that intends to remove the vitreous in a safe manner during a vitro-retinal surgery.

Another essential sub-function of removing the vitreous is transporting it out of the eye. To achieve this with minimal trauma to the patient, the instrument should provide a passage between the inside and outside of the eye. This passage can then be used to transport the vitreous without requiring additional openings other than the one to insert the instrument. The instrument should also apply power to the vitreous to generate the required movement for transportation. In the current vitreous cutters a vacuum is applied to the inner lumen of the inner cutting needle to move the vitreous out of the eye. In between the decoupling and transportation of vitreous it is important that relative movement between the instrument and the separated vitreous is minimized. Another sub-function of the instrument is therefore, to grab the vitreous. In the current instrument this is achieved by the vacuum that is applied to the vitreous.

2.4. Defining the motion and engine type

From the functional analysis it becomes clear that the functions related to the driving mechanism are; to enable the decoupling of vitreous by moving the inner needle, and to provide a passage through the instrument for transporting the vitreous. This section aims to define the engine type and cutter motion of the new driving mechanism. In Table 2 all the included patents from the aforementioned study on the driving mechanisms of vitreous cutters are listed. The patents are grouped according to the motion of the cutter and the engine type that is used by the drive mechanism. Figure 6 shows a schematic overview of these patents and the classification that was used to group them.

TABLE 2. CLASSIFICATION OF ALL PATENTS DESCRIBING A VITREOUS CUTTER DRIVING MECHANISM

		Cutter Movement			
		Translating	Rotating		Translating + Rotating
			Reciprocating	Continuous	
Engine Type	Fluidic	[23]–[55]	[56], [57]	[58]	[59], [60]
	Electromagnetic	[53], [61]–[83]	[84], [85]	[86]–[88]	[89]–[92]
	Manual	[93], [94]	[95]	No patents	No patents

According to the knowledge of the author there are no studies with the goal of identifying the most efficient movement type to separate the vitreous. The process of identifying the most efficient cutting motion falls out of the scope of this study. Therefore, the translating motion used in state of the art vitreous cutters will be replicated by the new drive mechanism developed in this study. It was observed from the patent literature that there are three engine types which are used to drive vitreous cutters: Electromagnetic, Manual and Fluidic.

Electromagnetic engines, such as for instance an electric motor, transform electrical energy into mechanical motion

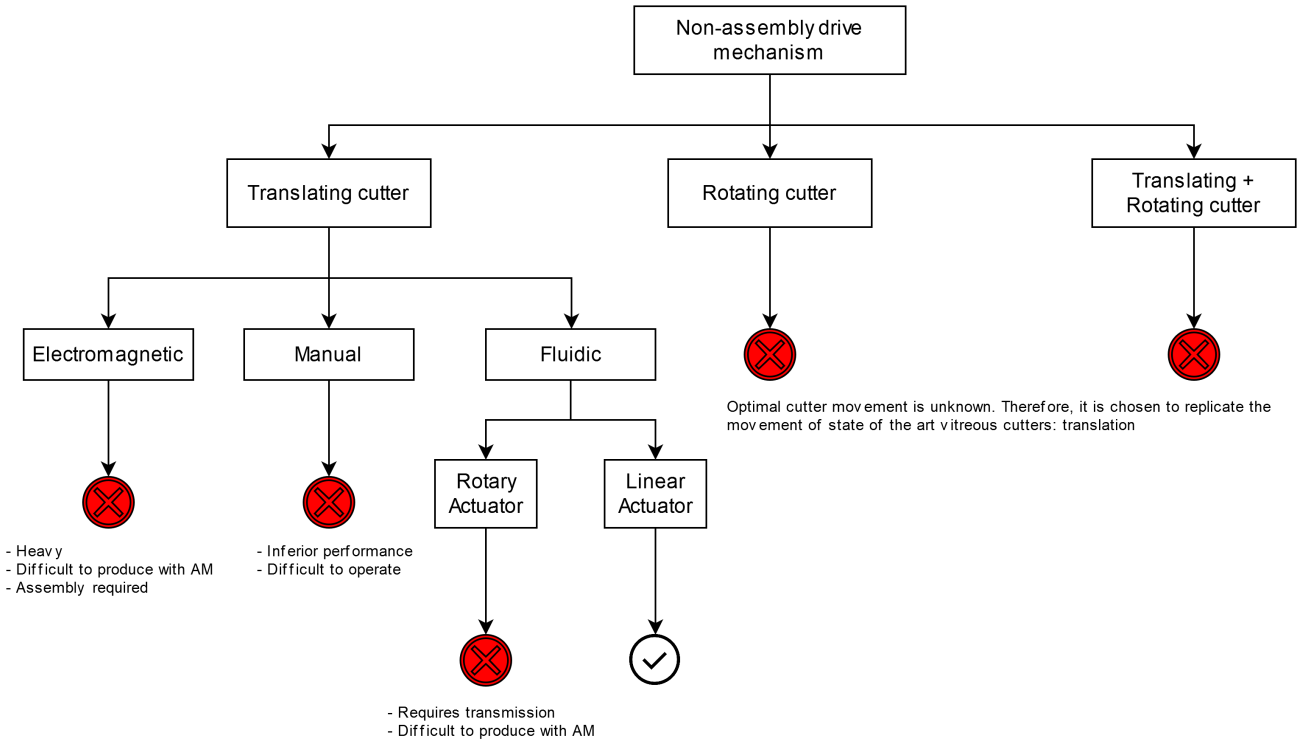

Figure 11. Schematic representation showing the motivation to choose a linear actuator in the new driving mechanism that generates a translating motion of the cutter.

by means of electromagnetism, or the piezoelectric effect. Electromagnetic driven vitreous cutters have been used in the past but have been replaced by fluidic vitreous cutters due to the higher weight associated with them. A downside to electromagnetic actuators with respect to this study is that they are difficult to produce by means of AM [96]. Electromagnetic engines require conductive spools and magnets, or piezoelectric materials to generate movement. Current state of the art AM technologies do allow for the printing of piezoelectric materials or magnets, but these processes are complex, unrefined, and are currently not ready to be used on a large scale [97], [98]. Because of these reasons electromagnetic engines are not suitable to be used in the new driving mechanism.

Manually driven cutters have also been found that drive translating vitreous cutters. Manually driven cutters work by transforming human motion into movement of the cutter to separate the vitreous. There are two main downsides associated with them:

1) the maximum cutting speed of a manual vitreous cutter is lower than that of state of the art vitreous cutters. It is not possible to manually actuate the needle to move in excess of 8000 times per minute without a transmission.
2) the user has an additional task of generating the movement of the cutting needle. Conventional vitreous cutters do this autonomously and therefore, the user can fully focus on performing the operation of removing the vitreous.

These reasons are deemed to make manually driven vitreous cutters obsolete and therefore, the new driving mechanism will not be manually driven.

The last group of engines are fluidic engines, fluidic engines use a difference in pressure of either a fluid or gas to generate movement. Fluidic engines are used to drive state of the art vitreous cutters. The construction of fluidic actuators can be very simple, and examples are known of fluidic actuators that are monolithic. Fluidic actuators can be divided into two groups: rotary actuators and linear actuators. The motion of the cutter that needs to be achieved is linear. However, it is possible to generate linear motion using a rotary actuator. A transmission such as for instance that of a cam and a spring loaded follower, can transform the rotatory output of the engine into a translating output of the cutter. These transmissions greatly increase the level of complexity of the drive mechanism and therefore, make it more difficult to produce them using non-assembly AM. Linear actuators do not require a transmission, as the movement that is generated by the actuator corresponds with the desired movement of the cutter. Because of the added difficulty of producing a transmission system, which is required for rotary actuators, a linear actuator should be used in the new driving mechanism. Figure 11 shows a schematic representation of the aforementioned reasoning and decisions.

3. Additively manufactured linear pneumatic actuators

3.1. Overview of AM processes

Each currently known AM process was listed according to the American Society for Testing and Materials (ASTM) F42 classification [99]. Some examples were found of new printing processes that are not yet officially classified in the ASTM standard, in these cases they were placed in the most appropriate group at the discretion of the author. A schematic representation of the AM processes is shown in Figure 12, references to found examples in the scientific literature are added to the corresponding printing processes. Metal AM methods were deemed unsuitable to be used to construct the new driving mechanism due to the fact that metals have a higher density than polymers. Instruments manufactured using metal AM would therefore be heavier than if they would be constructed using polymers.

3.2. General AM limitations

When designing for AM it is paramount to understand the benefits and limitations of the process in general. There are a lot of requirements that are process- and even printer-dependent, but some are applicable to AM in general. These general limitations were investigated first, to guide the concept development phase of the project. The limitations that were deemed to be most relevant for this study are shown below [17], [100].

- Difficult to manufacture parts that contain enclosed hollow volumes
- Inability to achieve tight tolerances
- Inability to manufacture functional assemblies without large amount of play.
- Minimum feature size should be > 0.5 mm.
- Print resolution is not uniform across build volume.
- Support material is required
- Parts present an-isotropic behaviour due to the influence of printing direction.
- Surface finish of parts is poor

This list gives an overview of the general limitations that are associated with AM. It should be noted that there are nuance differences between the different AM processes with regards to these limitations. For instance support material can be rigid printed material, or loose unused material. The loose material will be easier to remove, and therefore less of a limitation. Enclosed hollow volumes should be avoided if possible, as they are difficult to print and almost always require support material. The design should accommodate large mechanical play to account for printing inaccuracies. Play can be reduced by placing the features with tight tolerances in parallel with the printing plane, as the xy-resolution of printers is often higher than the resolution in the z-direction. Play can be removed entirely by replacing a rigid contact with a compliant interface, or by applying a pre-tension force to the mechanism. The dimensional accuracy of a printed part greatly depends on the chosen

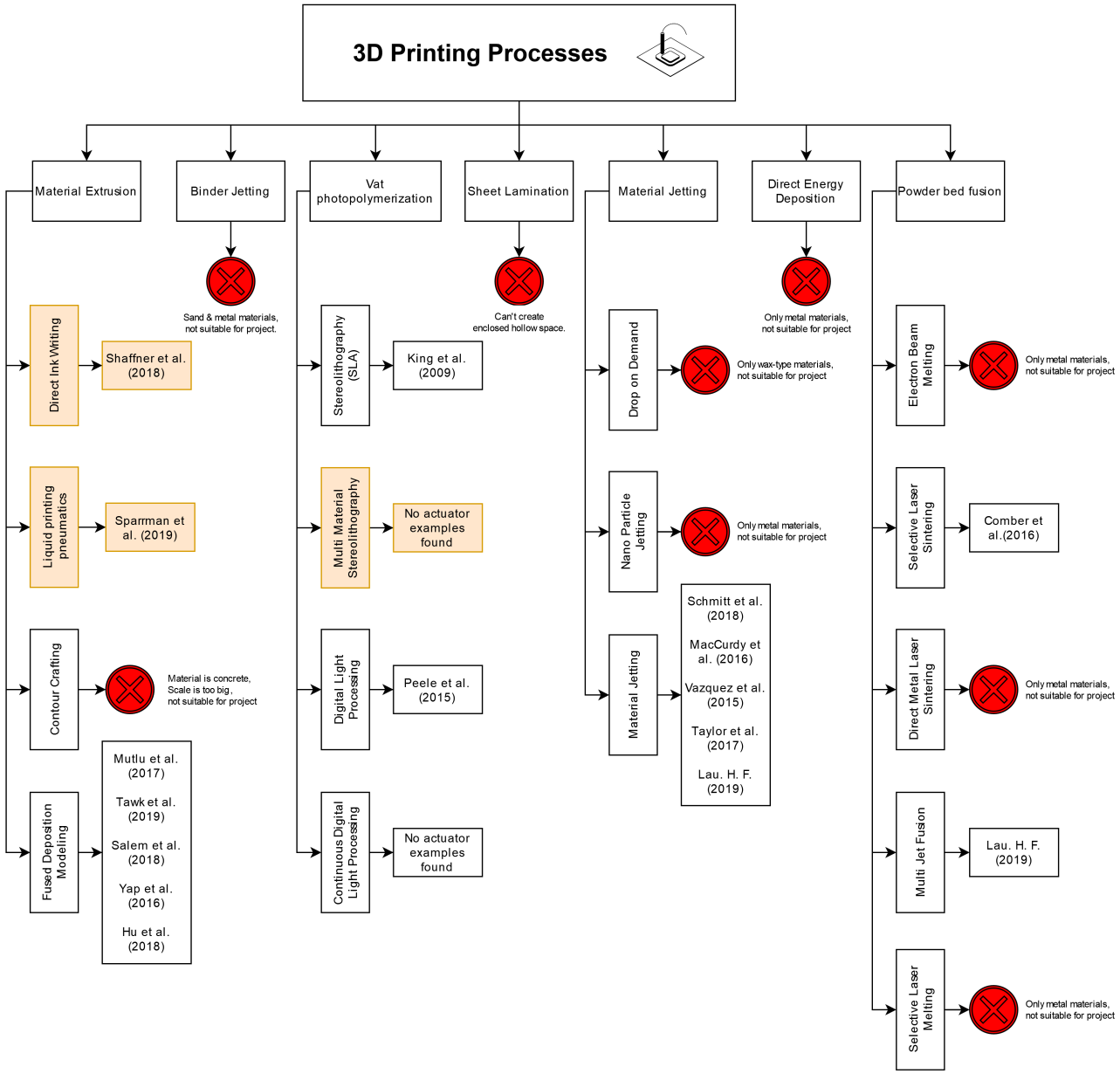

Figure 12. Schematic representation of all known AM processes, with an indication if the process is suitable. References to found examples from the scientific literature are also included of pneumatic actuators that are produced by means of AM.

printing process, and even on the specific printer that is used. The tightest tolerances can be achieved with the material jetting process and have a lower boundary of +- 0.05 mm [19]. Thought should be given on how the part can be supported during the printing process, as this can be done in a variety of different ways. Support material can often be minimized by choosing an optimal orientation of the part in relation to the printing plane [101]. When supports cannot be avoided, sufficient access should be provided to be able to remove them after printing. Components that move relative to each-other should be supported perpendicular to the plane of interaction, and supports should not touch the sliding surfaces. This is because the surface quality is degraded once the support material is removed. This in turn increases friction between the moving components, and hinders smooth movement. AM often results in an-isotropic parts. However, this is dependent on the chosen printing process as there are several processes that are capable of producing isotropic components, such as for instance SLA printing [102]. When an an-isotropic printing process is chosen, such as FDM, it is important to align the 3D printing plane with the dominant load, as parts are strongest in the direction parallel to the printing plane.

3.3. Actuator Classification

In section 2.3 it was determined that the actuator used to generate the motion in the new driving mechanism should be a linear fluidic actuator. The scientific literature was searched to identify the different types of linear pneumatic actuators that exist. Subsequently a search was made to look for examples of linear pneumatic actuators that were manufactured using AM methods.

Based on Krivits et al. [103] and de Volder et al. [104], it is possible to distinguish four types of linear pneumatic actuators.

1) McKibben actuators (elastic)
2) Bellows actuators (elastic)
3) Diaphragm actuators (elastic)
4) Piston actuators

The scientific literature was searched for examples of linear pneumatic actuators that were manufactured by means of non-assembly AM. Three of the four actuator types were found: McKibben actuators, bellows actuators and diaphragm actuators. Examples were also found of 3D printed piston actuators, but they required assembly after printing [105]. Therefore, they were excluded from further evaluation in this study. All the examples of additively manufactured pneumatic actuators were classified according to the their type.

3.4. McKibben actuators

Mckibben actuators are also called pneumatic muscles and can best be described as a cylinder with flexible walls with rigid end caps. When the internal volume of the actuator is subjected to air pressure, the flexible walls expand outward, shortening the length of the actuator, and generating movement. An image that shows the working principle of a McKibben actuator is shown in Figure 13. McKibben actuators have a high power to weight ratio (1kW/kg), as well as a long lifetime (10 million cycles) [103]. Drawbacks of the actuator are that its behaviour is non-linear and the actuators are single acting. This means that an outside force has to be applied to return the actuator to its initial position.

Schaffner et al. [107] describe several pneumatic actuators that were manufactured by means of AM. The specific printing process that was used is called Direct Ink Writing (DIW). The material that was used to manufacture the actuators was Silink, this is a silicone based material with different additives to control the stiffness of the material. Different concentrations of additives were added to create three distinct Silink material types: soft, intermediate and stiff. By combining these materials in a single actuator, in distinct substructures, the researchers were able to preprogram the motion of the actuator. A rendering of both a translating and a rotating McKibben actuator are shown in Figure 14. The translating actuator was able of generating a force of approximately 4.5 N and a displacement of approximately 2 cm. According to the authors there were no signs of inelastic deformation, or loss of performance after an extensive number of cycles [107].

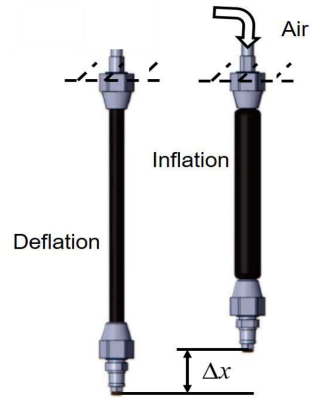

Figure 13. Image showing the working principle of a McKibben actuator. When air pressure is applied to the actuator, the actuator becomes shorter. Adapted from: [106].

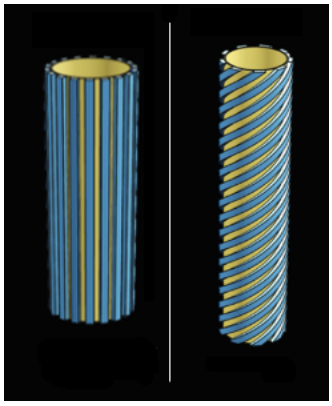

Figure 14. Rendering of two McKibben actuators, the left actuator contracts and therefore exhibits linear motion. The right actuator rotates when pressure is applied to it. Adapted from: [107]

3.5. Bellows actuators

Bellows actuators are similar to McKibben actuators, as they both have flexible walls. However, when air pressure is applied to a bellows actuator, the actuator extends. This is due to the construction of the actuator wall, it contains a corrugated profile that enables the extension of the actuator. When bellows actuators are used, internal stresses occur inside the actuator walls. Because the actuator is used repetitively, it is important to minimize these stresses to prevent failure of the actuator [103].

Over 12 examples were found in the scientific literature that describe bellows actuators manufactured by a range of different printing processes and techniques [108]–[118]. From the search in the scientific literature it became clear that the bellows type actuator is most often manufactured by AM in a non-assembly manner.

Five examples described bellows actuators that were manufactured by means of fused deposition modeling (FDM) [108]–[112]. The material that was used to manufacture these actuators was either TPU or TPE, different brands were used such as Ninjaflex and Filaflex. The reasoning

behind the choice for FDM as the AM method, was the availability of FDM printers, and the low associated costs with them. Figure 15 shows the bellows actuator that is described by Mutlu et al [108]. The wall thickness of the actuators was between 0.5 and 1.2mm, the width was between 20 and 47.7 mm and the length varied between 48 and 300 mm. Some of the actuators were constructed asymmetrically to create a bending actuator. These examples are still listed because they could easily be constructed in a symmetric fashion, resulting in a linear actuator. The lifetime of the actuators was tested in two of the examples [109], [111]. Yap et al. [111] tested the lifetime of their actuator at two different pressures; 250 kPa and 400 kPa. Three samples were tested at each pressure and the average respective lifetimes were; 606 cycles and 82 cycles. Tawk et al. [109] applied 95.7% vacuum to their actuators to actuate them. They determined the lifetimes of five different actuators that varied only in length, all other geometries were equal. On average the lifetime of all five actuators was 23.581 cycles, the difference between the longest and shortest lifetime was 3.475 cycles [109].

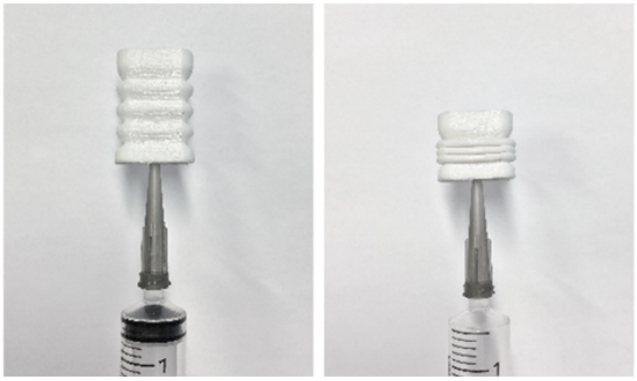

Figure 15. Photo showing a FDM printed bellows in both compressed and uncompressed states. Adapted from: [108]

Sparrman et al. [113], describe a novel AM process that is able to print silicone pneumatic actuators that are very flexible. The printing process works as follows: a needle deposits the build material as it moves through a build volume which is filled with a gel. This gel acts as a support for the build material, and because the gel has self-healing properties, the needle can move through it without effecting the print quality. This technique is still in the research phase, and currently there are no commercial printers available that use this technique. In Figure 16 an image is shown of the liquid printing process while a bellows actuator is being printed.

A bellows actuator that is additively manufactured using the digital light processing method (DLP) is described by Peele et al. [114]. The material that is used to manufacture the actuator was EP spot E resin, made by Spot A materials. A custom built 3D printer was used, that had a resolution of 37 microns in the XY plane, and 50 microns on the Z axis. The actuator was 20 mm in diameter, and had a wall

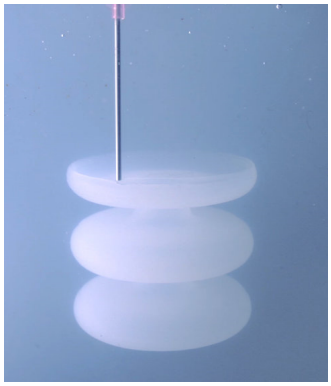

Figure 16. Photo showing the printing of a bellows actuator using the liquid printed pneumatics technique. Adapted from: [119]

thickness of 1.5 mm. Interesting was that they incorporated internal channels and chambers within the actuator to create bending movements in different directions. The smallest diameter of the internal air channel was 2 mm. The lifetime of the actuator was short, at approximately 9 actuation cycles.

One example was found that used the selective laser sintering process to create a bellows actuator [115]. The printing of the actuator was part of the research done by Comber et al. in an effort to create an MRI compatible needle actuator. The material that was used to manufacture the actuator was Nylon, and the printer that was used was a 3-D Systems Sinterstation 2500 Plus. The outer radius of the actuator was 22.2 mm and the wall thickness was 0.762 mm. The maximum operating pressure of the actuator was 550 kPa and the deflection of the actuator at this maximum pressure was 6 mm. The lifetime of the actuator was not mentioned by the authors. To remove the loose unused build material inside the actuator various clean-out holes were placed in the actuator design, which were later sealed with paraffin wax.

Three examples were found that described bellows actuators that were manufactured with the material jetting process [116]–[118]. The research conducted by Schmitt et al. [116] describes a multi-material actuator that is inspired by origami. A combination of rigid and flexible materials was used to create flexible hinges with rigid panels that connect them. The flexible material that was used was TangoBlackPlus and the rigid material was Verowhite. A stratasys connex 350 printer was used to manufacture the actuator. The actuator was capable of generating a peak force of 40 N at a pressure of 25 kPa, however, the lifetime of the actuator was very limited at 30 cycles. MacCurdy et al. [117] described another bellows actuator that was manufactured by means of material jetting. The material used to print the actuator was Rigur (RGD450) manufactured by Stratasys, an Objet 260 connex printer was used, also manufactured by Stratasys. The diameter of the actuator was 24 mm, and the wall thickness varied between 0.4 - 2.0 mm. The most interesting thing about this example is that the authors modified the printer to deposit a fluid that acted

as a support material. This allowed them to create small internal channels, and structures that would not be possible to manufacture with traditional support material.

Lau, H.F described the design process of developing a bellows actuator to drive a robotic arm [118]. During this process actuators were printed using two AM methods: material jetting and multi jet fusion. The materials that were used to print the actuators were Agilus30 for the material jetting process, and HP-Pa12 for the multi jet fusion process. The actuators were subjected to relative pressures from 0 bar to 1.8 bar in steps of 0.2 bar. The height of the actuators was 54.0 mm, and the average radius was 12.5 mm. Actuators with three different wall-thicknesses were constructed: 0.5, 1.5 and 3.0 mm.

3.6. Diaphragm actuators

Diaphragm actuators consist of a thin sheet of flexible material that is clamped, or supported on its circumference. Air pressure is applied to one side of this sheet, which causes the sheet to deform, and bulge outward. The profile of the diaphragm can be modified to increase it's range of motion, or to create a more uniform displacement at the centre. Diaphragm actuators are more compact than most pneumatic actuators, which makes them suitable to be installed in small spaces. They also have a spring rate which returns the actuator to its initial position, after the difference in air pressure between the two diaphragm surfaces is removed. However, their range of motion is generally limited, and the effective area of the diaphragm changes during its stroke. Therefore, the force that is generated by a diaphragm actuator is not constant over it's stroke [103].

Three examples were found of diaphragm actuators that were manufactured by means of AM. A diaphragm actuator in the form of a button is described by Vázquez et al. [120]. The printing process that was used to manufacture the button was material jetting. A schematic rendering of the button, along with a photograph of it, is shown in Figure 17. The printer that was used to manufacture this actuator was an Objet Eden 260 printer with a resolution of 42 microns. For the rigid material Vero Clear was used, and for the flexible material Tango plus. The maximum pressure that could be applied to the button before leakage occurred was 50 kPa. The maximum stroke of the diaphragm was 3.5 mm, and the thickness of the diaphragm was 1 mm [120]. Unfortunately, no information was provided on the lifetime of the actuator.

King et al. [121] describe a diaphragm based actuator that was manufactured by means of stereolithography (SLA). The actuator was part of a microfluidic pump used to transport fluids. The diaphragm had a diameter of 4 mm, a thickness of 70 microns, and was manufactured out of EnvisionTEC R11 resin. The printer that was used, was a EnvisionTEC Perfactory Mini SLA system [121]. The reliability of the diaphragm was tested by applying air pressure pulses with a frequency of 2 Hz to three sets of test diaphragms. A total of 1,000,000 cycles were applied over the course of six days without any failures. The maximum pressure that was applied was 24 kPa, and the maximum

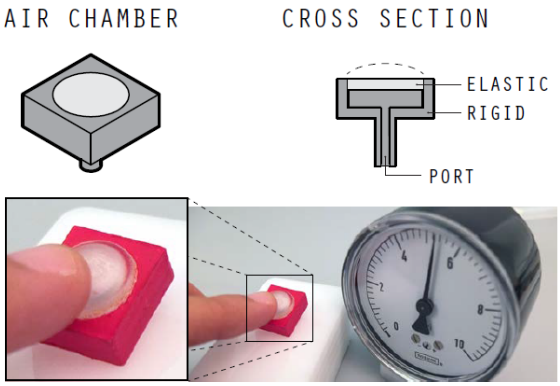

Figure 17. The top of the figure shows a rendering of the button and on the bottom a photograph of the button is shown. The photograph also shows the pressure inside the internal chamber of the button in psi. Adapted from: [120]

deflection at that pressure was observed to be 1.2 mm [121]. An exploded view and photograph of the diaphragm pump are shown in Figure 18.

Figure 18. An exploded view rendering of the diaphragm pump is shown on the left and a photograph of the pump is shown on the right along with a UK 5 pence piece for scale. Adapted from: [121]

The last diaphragm actuator that was found is described in the paper by Taylor et al. [122]. This diaphragm actuator was also part of a monolithic pump and was manufactured with the material jetting process. In this pump there were a total of three diaphragms, of two sizes. Two small diaphragms that opened and closed the inlet and exhaust openings, and one large diaphragm that provided the force for pumping. All three diaphragms had a thickened middle part that acted as a piston. The centre of the diaphragm was therefore more stiff than the surrounding material. A photo of the cross-section of the monolithic diaphragm pump is shown in Figure 19. The outer diameter of the large diaphragm was 20 mm and the diameter of the large piston was 12.8 mm. The outer diameter of the small diaphragms was 6 mm and the diameter of the small piston was 4 mm. The minimum thickness of the diaphragms was set close to 1 mm based on the advice of material jetting experts. The stroke of the large diaphragm was 2.4 mm, and the pressure used to actuate it was 55.4 kPa. The small diaphragms showed a lifetime of over 2 million cycles.

The large diaphragm failed more quickly, but still had a lifetime of over 850 thousand cycles [122]. The material used to construct the pump was TangoBlackPlus, and the pump was printed using a Stratasys Objet 1000. The internal cavities in the mechanism were filled with FullCure 705 support material during printing, this support material was completely removed after manufacturing using 2% NaOH solution in H_2O, and mechanical agitation.

Figure 19. A photograph of the cross-section of the monolithic diaphragm pump, showing the three diaphragms inside. Adapted from: [122]

4. Driving mechanism development

4.1. Requirements

The requirements for the new driving mechanism were formulated based on the goal of this study, the specifications of the 8268.VIT23 TDC cutter manufactured by DORC, by reading the available scientific literature on vitro-retinal surgery, and by discussions with engineers who designed the instrument. The requirements are divided into two groups:

1) Leading design requirements
2) Boundary conditions

4.1.1. Leading design requirements

The requirements in this group should define the design and should reflect its core functions.

[Req 1] The driving mechanism should be manufactured by means of AM as a non-assembly mechanism, no components that are part of the driving mechanism should be assembled after printing.

In section 3.2 the general limitations of AM are discussed. These limitations should be taken into consideration to successfully manufacture the driving mechanism using AM processes.

[Req 2] The inner needle assembly should be driven to translate reciprocally with respect to the outer stationary needle.

It is determined that continuous rotating vitreous cutters can exhibit wind-up of the vitreous around the cutter, resulting in a higher chance of a retinal detachment [10]. The performance of other possible movements of the cutting blade such as reciprocating rotating movement and a combined translating and rotating movement has not been investigated thoroughly. It does not fall within the scope of this research to identify the optimal cutting motion of a vitreous cutter. Therefore, the new driving mechanism should achieve an identical motion to the currently sold vitreous cutters. This is also the reason to only drive the inner needle, as the effects of driving both the inner and outer needles have not been investigated properly.

[Req 3] The maximum pulse rate of the driving mechanism should be 8000 pulses per minute (PPM), due to the TDC needles this results in a cut rate of 16000 CPM.

It has been shown that increasing the cut rate of the instrument while keeping the aspiration pressure constant, leads to less traction on the retina [123]. Manufacturers of vitreous cutters are continuously improving their cut speeds to minimize the retinal traction. The highest cut rate of the DORC 8268.VIT23 instrument is 16000 CPM therefore, the new mechanism should also be able to generate that cut rate.

[Req 4] The stroke length of the driving mechanism should be 0.8 mm

The stroke length of the driving mechanism is based on the geometries of the cutting ports, the tolerances of the cutting ports and a safety factor to ensure that the vitreous cutter always fully opens and closes both cutting ports. It is deemed to be impossible to produce the cutting needles using current AM technologies. Therefore, it is assumed that a set of identical cutting needles to the DORC 8268.VIT23 vitreous cutter will be used. The stroke length of the mechanism should therefore, be equal to that of the DORC 8268.VIT23 vitreous cutter.

[Req 5] The cutting force generated by the driving mechanism should be 9 N in the forward direction and 8 N in the backward direction.

Currently it is unknown how much force is required to separate a piece of vitreous. However, it is known what the maximum forces are with which the needle is actuated in the DORC 8268.VIT23 instrument. It was determined that the new driving mechanism should match this force profile as close as possible.

[Req 6] The driving mechanism is powered by an external pressurized air supply.

In section 2.4 the choice to use a fluidic actuator is motivated extensively. Furthermore, the industry standard is to use instruments which are powered using an external air pressure source.

4.1.2. Boundary conditions

The boundary conditions are set to ensure that the device is usable, these requirements are taken into consideration in the design process, but should not define the design.

[Req 7] The inner needle assembly should be able to be attached to the driving mechanism after/during printing, and should not separate during use.

The general limitations associated with current AM processes do not allow for a reliable production of tightly toleranced needles. Therefore, the needles are attached to the driving mechanism after or during printing. The connection between the needle and the driving mechanism should be strong enough to prevent separation during use.

[Req 8] The lifetime of the driving mechanism should be more than 300,000 cycles.

Vitreous cutters are used intermittently during a vitrectomy procedure and at a variety of different cutting speeds, depending on the location of the instrument inside the eye. Therefore an estimation of the maximum amount of cycles is made during a long vitrectomy procedure. This is then used to quantify the minimal lifetime of the instrument, to ensure that the vitreous cutter will have a minimal lifetime equal to the duration of a single procedure.

It was assumed that 10 minutes of cutting with a speed of 5,000 PPM represents the core vitrectomy step of the procedure. 5 minutes of cutting with the maximum cutting speed of the instrument, was assumed to represent the retinal shaving step. A safety factor of 3 is taken to account for potential deviations from these numbers.

$$5,000 \text{ PPM} * 10 \text{ min} = 50,000 \text{ cycles}$$

$$8,000 \text{ PPM} * 5 \text{ min} = 40,000 \text{ cycles}$$

$$50,000 \text{ cycles} + 40,000 \text{ cycles} = 90,000 \text{ cycles}$$

$$90,000 \text{ cycles} * 3 = 270,000 \text{ cycles} \approx 300,000 \text{ cycles}$$

[Req 9] The driving mechanism should be able to function regardless of the aspiration pressure that is applied to the instrument. The aspiration pressure varies between; atmospheric pressure (no aspiration), and 0.13 bar (maximum aspiration).

Because the design of the cutting needles themselves falls out of the scope of this study, the new driving mechanism should allow for the aspiration of vitreous using an applied vacuum. The aspiration pressure varies during the procedure therefore, the driving mechanism should be able to operate over the aforementioned range of aspiration pressures.

[Req 10] The driving mechanism should be as close to true scale as possible. Therefore, the size of the new driving mechanism should be comparable to the handle of the DORC 8268.VIT23 instrument.

TABLE 3. LIST OF ALL REQUIREMENTS FOR THE NEW DRIVING MECHANISM

Req no.	Requirement
Req 1	The driving mechanism should be manufactured by means of AM as a non-assembly mechanism, no components that are part of the driving mechanism should be assembled after printing.
Req 2	The inner needle assembly should be driven to translate reciprocally with respect to the outer stationary needle.
Req 3	The maximum pulse rate of the driving mechanism should be 8000 [PPM], due to the TDC needles this results in a cut rate of 16000 CPM.
Req 4	The stroke length of the driving mechanism should be 0.8 mm
Req 5	The cutting force generated by the driving mechanism should be 9 N in the forward direction and 8 N in the backward direction.
Req 6	The driving mechanism is powered by an external pressurized air supply.
Req 7	The inner needle assembly should be able to be attached to the driving mechanism after printing, and should not separate during use.
Req 8	The lifetime of the driving mechanism should be more than 300.000 cycles.
Req 9	The vitreous is aspired from the eye by means of an applied vacuum. The minimal aspiration pressure is equal to the atmospheric pressure, the maximum aspiration pressure is 0.13 bar or 660 mmHg.
Req 10	The driving mechanism should be as close to true scale as possible, therefore the size of the new driving mechanism should be comparable to the handle of the 8268.VIT23 instrument

4.2. Actuator selection

In sections 2.3 and 2.4 it is established that the new driving mechanism should generate a linear motion of the cutter by means of a pneumatic actuator. There are three types of linear pneumatic actuators that have been produced using non-assembly AM: McKibben actuators, Bellows actuators, and Diaphragm actuators.

McKibben actuators require a large space to function due to the expansion of the actuator upon actuation. Furthermore, two McKibben actuators would be required in the driving mechanism for a vitreous cutter, since the actuator does not return to its initial position without an externally applied load. The lifetime of a vitreous cutter should be more than 300,000 cycles to last for the duration of a single procedure. Bellows actuators are known for having a shorter lifetime due to the internal stresses that occur inside the actuator walls. Examples from the scientific literature given in section 3.5 show that it is unlikely that a bellows actuator, which is produced using AM, has a sufficiently long lifetime. Because the handles of state of the art instruments are small, it is beneficial if the actuator can be installed in a confined space. Examples from the scientific literature show that it is possible to produce non-assembly diaphragm

mechanisms using AM that have a long lifetime (+1,000,000 cycles) [122]. Diaphragm actuators also have a small range of motion, and require only a small amount of space to function. These attributes make it an ideal actuator for a driving mechanism for a vitreous cutter. As the stroke length of a vitreous cutter is under 1 mm, the range of motion of the actuator does not have to be big. After analysing the advantages and disadvantages of each of these actuators, in combination with the formulated requirements, a diaphragm actuator was selected for further development. In Table 4 the aforementioned aspects are summarized for all linear pneumatic actuators that have previously been produced using non-assembly AM.

TABLE 4. ACTUATOR SELECTION TABLE

	McKibben Actuator	Bellows Actuator	Diaphragm Actuator
Required Space	- -	-	++
Lifetime	+	-	++
Range of motion	Big (-)	Big (-)	Small (++)
Examples produced using AM	Yes	Yes	Yes

Table showing the comparison between all known linear pneumatic actuators that were produced in a non-assembly manner using AM.

4.3. Concept working principle

After determining that a diaphragm actuator was the most suitable actuator to be used in the new driving mechanism, it was decided to analyse the currently used diaphragm mechanisms in vitreous cutters further. This was done by sketching the most simple form of the standard driving mechanism as shown in Figure 7, by leaving out as much components as possible that do not contribute to the working principle of the instrument. The components that are integral to the working of the device on a conceptual level are drawn in in their most simple form. This sketch led to the realisation that the entire instrument could theoretically be manufactured out of only two components that move relative to each other. Component one consists of a handle in which the outer needle is integrated. The second component is the diaphragm with the attached inner cutting needle. A schematic drawing of this two component instrument is shown in Figure 20.

This gave more insight into the problem and the solution on a fundamental level. Because the air chamber of the diaphragm is at the rear of the instrument, and because the inner cutting needle needs to move relative to the housing; a seal is required between the housing and the inner cutting needle. When conventional manufacturing techniques are used, this problem could easily be solved by adding an o-ring seal that is tightly toleranced to allow for movement between the seal and the cutting needle, without generating excessive air leakage. In order for the driving mechanism to be non-assembly, o-ring seals that are manufactured with

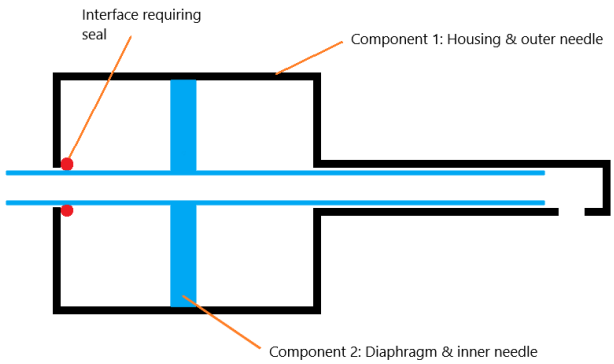

Figure 20. Schematic representation of a vitreous cutter constructed out of only two components.

an alternative manufacturing method and assembled after or during printing cannot be used. Producing the o-ring seals using AM is difficult because of the inability of the technology to produce parts with tight clearances and high tolerances. However, AM can also provide a unique solution to this problem. It is indicated and proven in past research that flexible connections between two components can remove the play between them while still allowing movement [17]. This led to the idea of replacing the o-ring seal in the standard mechanism with another flexible diaphragm that is smaller than the diaphragm that generates the movement of the cutting needle. A schematic drawing of this dual diaphragm instrument is shown in the top image of Figure 21. It is essential that the diaphragms have a sufficiently different surface area, to achieve a force difference when air pressure is applied to the air chamber of the instrument. If both diaphragms would be of equal size, the force on the cutter would be equal in both directions, resulting in no net movement of the cutting needle. A schematic representation of the dual diaphragm mechanism while it is pressurized is shown in the bottom image of Figure 21

4.3.1. Proof of principle

A proof of principle prototype was made to test the working principle. The prototype consisted of a plastic cup which was sealed with a balloon on both sides. An old bicycle tire valve was used to apply air pressure to the cup. A straw was attached to both balloons with tape to create a sealed air chamber. A photograph of the prototype is shown in Figure 22. It was observed that the straw moved in the direction of the large diaphragm when air pressure was applied. This proved that the concept could work in principle. Based on the principle of sealing the air chamber with flexible diaphragms a total of four concept variations were generated for the non-assembly driving mechanism.

4.4. Concept variations

The cutting needle has two directions of movement: forwards and backwards. The movement of the needle can be generated in two ways: 1. An air pressure pulse is applied

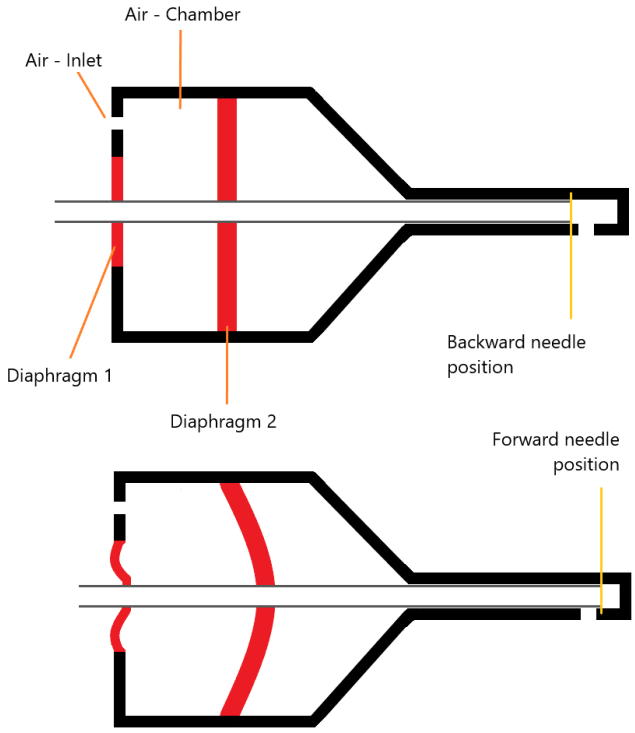

Figure 21. Schematic representation of the dual diaphragm concept in neutral (top image) and pressurized (bottom image) condition. Diaphragm 1 seals the air chamber, Diaphragm 2 generates the motion of the inner cutting needle.

Figure 22. Photograph of the proof of principle prototype that was used to test if movement would be generated if the air chamber was sealed with two differently sized diaphragms.

to one side of the diaphragm, causing it to deform and move the attached cutting needle. 2. The spring rate of the diaphragms can return the needle to its initial position after it is displaced by an air pressure pulse. These two methods to create movement are not completely independent, as the diaphragm spring rate can only be used to move the needle once it is displaced from its neutral position. Therefore, an air pressure pulse should always be used to create an initial displacement of the needle in either the forward, or backward direction. This can be achieved by changing the location of the large diaphragm, as the needle will move in the direction of the large diaphragm once an air pressure pulse is applied to the air chamber. As there are two directions of movement (forwards and backwards), it can be deduced that there are two possible variations of a driving mechanism which uses a combination of a pressure pulse and the spring rate of the diaphragms to move the cutting needle.

It is also possible to move the needle entirely by applying air pressure pulses, this can be achieved by creating two mirrored air chambers that are sealed using a combination of small and large diaphragms. The diaphragms will still apply a spring rate to the needle once it is displaced, however, the mechanism does not rely on it to move the cutting needle. Again, there are two possible combinations for constructing these chambers, as the chambers need to be mirrored, and there are two diaphragm types (big & small). For each combination of the aforementioned aspects, a concept variation was developed. This led to the creation of the four concept variations which are shown in Figure 23. In Table 5 the aforementioned reasoning behind the four variations is shown.

4.4.1. Variation A

Variation A uses a single pressure pulse to generate a forward movement of the cutting needle and uses the internal spring rate of the mechanism to move the needle back to its initial position. The small diaphragm is located in the back of the instrument and the large diaphragm in the front. The mechanism will move in an identical manner to the proof of principle prototype once an air pressure pulse is applied.

4.4.2. Variation B

Variation B uses two pressure pulses applied to either side of the diaphragm to move the needle forwards and backwards. When pressure is applied to the most forward air chamber, the needle will move backward, when pressure is applied to the rear air chamber, the needle will move forward. Two smaller diaphragms seal the air chambers located on opposite sides of the large diaphragm. The most forward diaphragm prevents pressurized air to enter into the eye through the space between the inner and outer cutting needles. This variation does not rely on the spring rate generated by the diaphragms. Therefore the requirements on the material of the diaphragms and its thickness will be of less importance than in variations A and D. This is due

TABLE 5. ORIGIN OF THE FOUR CREATED VARIATIONS

		Movement generation	
		Pulse + spring rate	Dual pulse
Large diaphragm	Front	Variation A	Variation B
	Rear	Variation C	Variation D

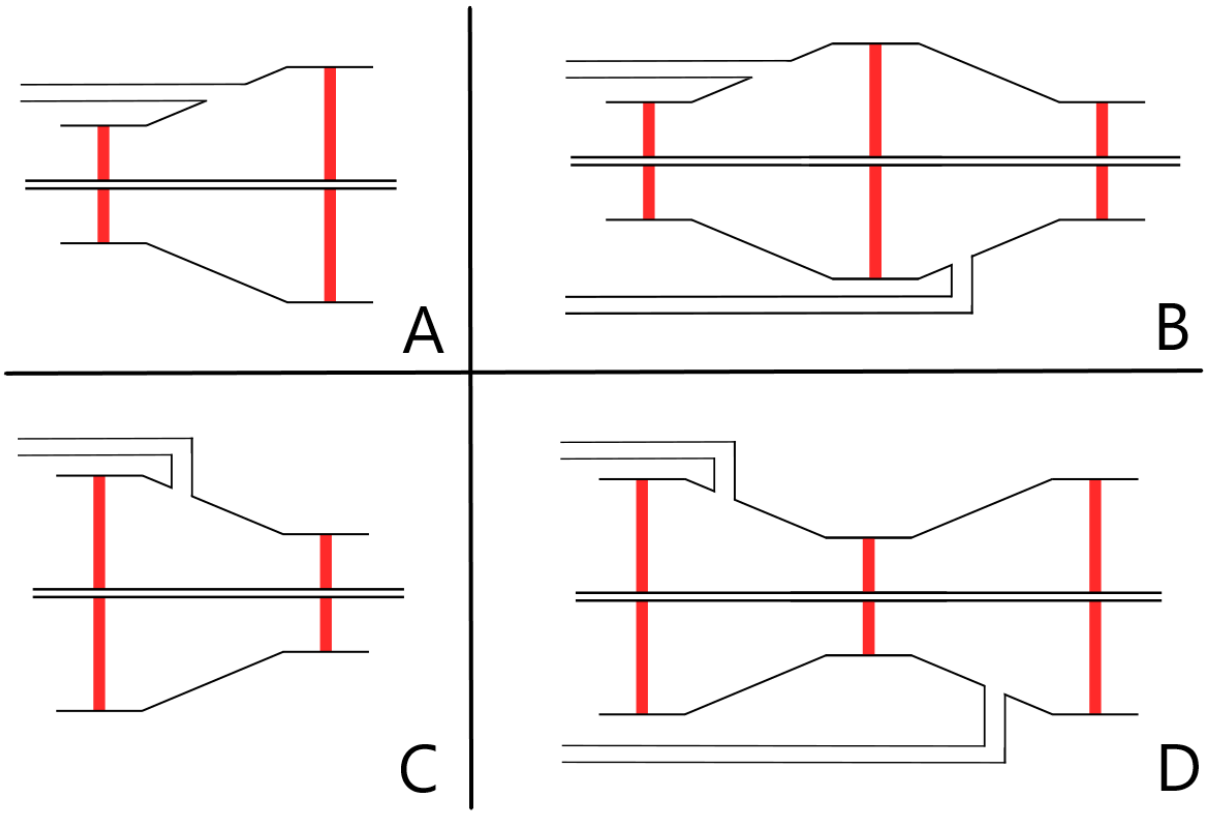

Figure 23. Schematic representation of the four concept variations A, B, C, D.

to the fact that these parameters have a large influence on the spring rate.

4.4.3. Variation C

Variation C again uses a single air pressure pulse to drive the instrument. Due to location of the large diaphragm, the needle will move backwards once air pressure is applied to the air chamber. The small diaphragm in the front prevents air leakage into the eye. The spring rate of the mechanism will move the needle forward once the air pressure in the air chamber is reduced.

4.4.4. Variation D

Variation D also uses two pressurized air pulses to move the cutter. The amount of diaphragms is equal to that of variation B. However, the large diaphragms are now placed in the most forward and backward positions with a small diaphragm in the centre. When air pressure is applied to the most forward air-chamber, the cutting needle will move forward, when air pressure is applied to the rear air-chamber, the needle will move backwards.

4.5. Variation selection

The two variations where the large diaphragm are placed in the back of the instrument are deemed to be less favourable due to the influence of the aspiration pressure. The aspiration pressure is applied to the lumen of the inner cutting needle. This pressure also interacts with the rear most diaphragm, if no other sealing diaphragms are placed between the inner needle and the housing. It is known that a pressure acting on a larger surface will lead to a larger force. This means that the force caused by the aspiration pressure in the backward direction, will be larger if the large diaphragm is subjected to the aspiration pressure.

As a result, variation C will most likely not be usable as the aspiration pressure interacts with the large diaphragm, resulting in a higher force in the backward direction. Furthermore, when a pressure pulse is applied to the mechanism it will move the cutting needle in the backward direction. Other than the spring rate of the diaphragms there is no force in the forward direction. The spring force should therefore be bigger than in variation A. Because of these reasons it was deemed that concept variation C was unsuitable to develop further in this study.

When the aspiration pressure interacts with a large diaphragm the influence of the aspiration pressure will be increased. To compensate for that, the magnitude of the pressure pulse applied to the forward chamber should be increased. The required air pressure pulse is therefore larger, than would be the case if a small diaphragm is under the influence of the aspiration pressure. This increase in pressure

will lead to increased stresses inside the diaphragm material, increasing the probability that the mechanism fails. Variation D is therefore deemed to be inferior to variation B. However, variations A and B both look promising at first glance. The most important difference between both of the variations is that variation A requires a specific spring characteristic of both of the diaphragms to function properly, while variation B does not. Variation B will likely be more complex to manufacture due to the presence of two enclosed hollow volumes instead of a single one in variation A. Variation B will also require a more complex system to supply the pressure pulses to the instrument, as two pulses are required that need to be delivered at particular points during the cutting cycle. To make a final decision on what variation is best suitable to use as a non-assembly driving mechanism for vitreous cutters, it should be investigated if AM materials can generate the appropriate spring characteristic. If this is possible, then variation A will be most likely the best option to use in future instruments, as its construction and actuation is more simple. Creating and testing a series of prototypes made from a range of materials based on variation A, will be able to determine if it is possible to generate the appropriate spring characteristic. In the case that it is not possible to create the appropriate properties of the mechanisms with current materials, the best course of action will be to develop variation B further, as it is less dependent on the properties of the used material.

4.6. AM process selection

In chapter 3, all known AM processes are discussed as well as examples from the scientific literature of linear pneumatic actuators that were produced using AM. The processes that were previously used to print a diaphragm actuator in other studies are: SLA and Material Jetting. These two printing processes have the highest resolution when compared to the other AM processes. In these studies diaphragm mechanisms have been described at a smaller, or similar scale that would be able to fit inside the handle of a vitreous cutter. The SLA printing process works as follows: A tank with a transparent bottom surface is filled with resin. A build platform is inserted into the resin tank and is slightly above the bottom surface, so that a small film of resin is in between the build platform and the bottom of the tank. A laser beam shines through the bottom of the tank and thereby cures the resin film and adheres it to the build platform. When a layer is complete, the build platform raises slightly and the process is repeated. The material jetting process is different, in this process an ink-jet print head moves in the xy-plane above the build platform. The ink-jet print head accurately deposits uv-curable resin droplets on the build platform, which are instantly cured by a uv-lamp attached to the print head. Once a layer is completed, the build platform lowers and the process is repeated. The material jetting process has the capability to create parts that are constructed out of multiple materials, as the ink-jet print head can have multiple nozzles that deposit the resin. The materials available for the material jetting have a range of different mechanical properties such as for instance: tensile strength, Young's modulus, shore hardness and flexural rigidity. This means that the design freedom is greater when compared to the SLA process due to the fact that certain section of the part can be made to be more flexible than others. As the concept design revolves around two diaphragm sections that need to be flexible when compared to the housing, it is beneficial to use the material jetting process. An additional advantage is that the material jetting process allows for the mixing of two base materials into a "digital material". Different digital materials can be constructed by using different base resins, or different mixing ratio's. These digital materials could in theory change the material properties within each voxel of the part, allowing to fine tune part behaviour to a very high degree. Of course flexibility of the diaphragms can also be achieved in other ways than changing the material, such as for instance by changing the geometry.

It was chosen to use the material jetting AM process due to the fact that a wide range of materials is available, and that it is possible to print multi-material parts. Furthermore, past research has shown that it is possible to print diaphragm actuators using material jetting that have the appropriate scale, and lifetime.

4.7. Calculations

4.7.1. Force output from mechanism

Since it is currently unknown how much force is necessary to cut the vitreous, it was decided that the new driving mechanism should deliver a similar amount of cutting force in the forward, and backward direction compared to current vitreous cutters. Current instruments have a net cutting force of 9 N in the forward direction, and 8 N in the backward direction. When it is assumed that the mechanism is able to generate a spring force of 8 N, then the net force developed by the mechanism in the forward direction should be approximately 17 N. This section details how the dimensions of the diaphragms were determined, and calculates what the force output of the mechanism will be when it is subjected to a range of air pressures. It is also evaluated how large the influence of the aspiration pressure is on the force output of the mechanism.

According to Di Giovanni et al, one of the general assumptions to accurately predict diaphragm behaviour is that the diaphragm should not have a thickness which is higher than 20 % of the outer diameter of the diaphragm [124]. Due to the limitations of the material jetting process, the minimal thickness of the diaphragms is 1 mm.

From this it follows that the minimum diameter of the diaphragms should be $>$ 5mm, it was decided to give the small diaphragm a diameter of 7 mm. The diaphragm diameter should be $<$ 16 mm to fit inside the handle of a vitrectome, the diameter of the large diaphragm was therefore chosen to be 14 mm. The maximum thickness of a diaphragm with a diameter of 14 mm is 2.8 mm, it was chosen to give the large diaphragm a

thickness of 2.3 mm. These dimensions are listed in Table 6.

In an actual instrument a cutting needle should be able to attach to the diaphragms of the mechanism. Therefore, a rigid centre should be constructed to use as an attachment point for the cutting needle. Constructing a rigid centre in a diaphragm has a positive influence on its performance, as it increases the effective area (A_{eff}) of a diaphragm [103], [124]. The effective area is the constant which is multiplied by the pressure difference (dP) across the diaphragm to determine the displacement force (F) of the diaphragm, see Equation 1.

$$F = dP * A_{eff} \tag{1}$$

According to Krivits et al, the diameter of the rigid centre is commonly determined based on Equation 2 [103]. In this equation, D_i is the diameter of the rigid centre, and D_o is the outer diameter of the diaphragm. Using this equation it can be determined that the diameter of the rigid centre for the large diaphragm should be approximately 6.58 mm, and for the small diaphragm 3.29 mm. The final diameter of the rigid centre was chosen to be 6.5 mm for the large diaphragm, and 3.0 mm for the small diaphragm. All of the determined dimensions related to both diaphragms are listed in Table 6. In Figure 24 a schematic drawing is shown of a single diaphragm along with the established dimensions.

$$D_i = (0.4/0.85) * D_o \tag{2}$$

TABLE 6. DIAPHRAGM DIMENSIONS

	Small diaphragm	Large diaphragm
Thickness (T)	1 mm	2.3 mm
Outer diameter (D_o)	7 mm	14 mm
Inner diameter (D_i)	3 mm	6.5 mm

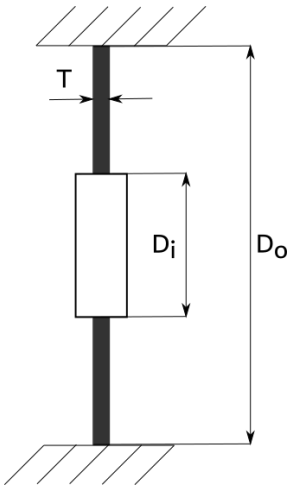

Figure 24. Schematic drawing of a single diaphragm to indicate the relevant dimensions

A schematic free body diagram of the needle is shown in Figure 25. This figure shows that the net force developed by the mechanism in the forward direction (F_{net}) is equal to the difference between the force applied to the needle by the large and small diaphragms (F_{large}, F_{small}), see Equation 3.

$$F_{net} = F_{large} - F_{small} \tag{3}$$

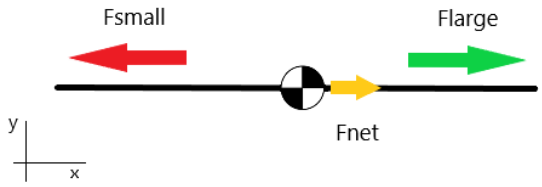

Figure 25. Schematic drawing of the free body diaphragm of just the needle in between both diaphragms. The green arrow represents the force which is applied by the large diaphragm, the red arrow represents the force which is applied by the small diaphragm. The orange arrow extending from the centre of mass of the needle represents the net force which is developed by the mechanism.

The force which is generated by a rigid centre diaphragm under the influence of air pressure is described by Di Giovanni et al using Equations 1, 4 and 5 [124].

$$A_{eff} = \frac{16 * (0.5 * D_o)^2 * (\frac{n^2-1}{4*n^2} - \frac{\ln(n)^2}{n^2-1})}{1 - n^{-4} - 4 * n^2 * \ln(n))} \tag{4}$$

$$n = \frac{D_o}{D_i} \tag{5}$$

Using the aforementioned dimensions of both of the diaphragms, the effective area (A_{eff}) for both diaphragms can be calculated. Before calculating the force that is applied by the diaphragms, the pressure difference over both diaphragms needs to be evaluated. It can be observed that there are three distinct pressure zones in the instrument, this is illustrated in the schematic representation of the mechanism shown in Figure 26. From this schematic it can be seen that the pressure drop over the small diaphragm is equal to the difference in pressure between zone 1 and zone 2. The pressure drop over the large diaphragm is equal to the difference in pressure between zone 2 and zone 3. The absolute pressure in zone 2 is equal to the pressure pulse that is applied to the instrument. The pressure in zone 3 is always equal to the atmospheric pressure. The pressure in zone 1 varies depending on the level of aspiration between atmospheric pressure (no aspiration), and 0.13 bar (maximum aspiration).

Using the aforementioned pressure data and equations, the force output of the mechanism can be calculated. In Figure 27, the force output of the mechanism is plotted against the pressure that is applied in zone 2 of the instrument. Two force profiles are shown, one for minimum aspiration (atmospheric pressure), and the other for maximum aspiration

TABLE 7. MATERIAL PROPERTIES OF MATERIAL JETTING MATERIALS

Material	Ultimate tensile strength σ	Young's Modulus E	Poisson's ratio μ	Calculated spring coefficient k_{total}
TangoBlack	1.8 - 2.4 MPa [125]	0.76 MPa [125]	0.3 [122]	$2.7 * 10^3$ N/m
TangoBlackPlus	0.8 - 1.5 MPa [125]	0.34 MPa [125]	0.49 [126]	$1.4 * 10^3$ N/m
Agilus30	2.1 - 3.1 MPa [127]	0.24 MPa [128]	Unknown	$5.9 * 10^3$ N/m
Vero	50 - 65 MPa [129]	2 - 3 GPa [129]	0.33 [126]	-

Table showing the material properties of flexible materials that can be printed with the polyjet printing technique.

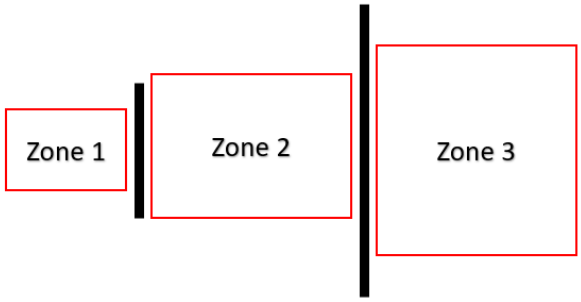

Figure 26. Schematic overview showing the three pressure zones that exist within the mechanism.

(pressure of 0.13 bar). Two horizontal lines are also drawn that indicate a force of 0 N and 17 N.

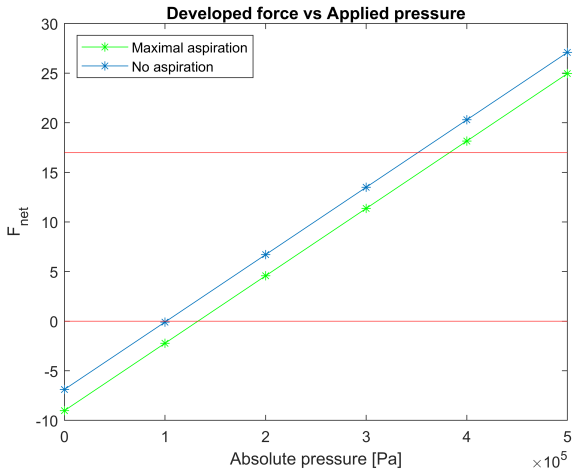

Figure 27. Plot of the force difference between the large and the small diaphragms vs the air pressure that is applied to the air chamber. Two horizontal red lines are drawn that indicate a force difference of 0 N and 17 N.

The figure illustrates that the chosen dimensions for both of the diaphragms are appropriate to generate the desired force of 17 N in the forward direction at a pressure of 3.5 bar, when there is no aspiration. With maximum aspiration, a force of 17 N is reached at a absolute pressure of 3.8 bar. The net force difference (F_{net}) is 2.3 N lower when the aspiration is at its maximum, when compared to the situation when there is no aspiration. This is due to the fact that the force generated by the small diaphragm F_{small} increases when the pressure in zone 1 is lower than atmospheric pressure. At maximum aspiration, the absolute pressure in zone 1 is 0.13 bar, which is lower than atmospheric pressure, leading to a larger pressure drop over the small diaphragm.

4.7.2. Spring rate of mechanism

An important aspect of the mechanism that needs to be considered is the spring force that returns the cutter to its neutral position when the pressure is vented from the chamber. The travel of the mechanism is 0.8 mm, and the cutting force in the extended position should be approximately 8 N. When it is assumed that both diaphragms act as a linear spring in the horizontal direction, it can be deduced by means of Equation 6 that the spring coefficient k_{total} of the mechanism should be 10000 N/m. This section aims to calculate if it is possible to create a mechanism that has a spring coefficient of 10000 N/m, using diaphragms with the dimensions as listed in Table 6 made with common material jetting materials. It is assumed that the materials act as a linear elastic material, as it allows to form an initial estimation of the spring rate of the mechanism.

$$F = k * s \tag{6}$$

The spring coefficient of a single diaphragm with a rigid centre (k) according to Krivits et al, is shown in Equation 7 [103]. T is the thickness of the diaphragm, E the Young's modulus, and μ is the Poisson's ratio of the diaphragm material.

$$k = \frac{16 * \pi * E * T^3 * n^2 * (n^2 - 1)}{3 * D_o^2 * (1 - \mu^2) * [(n^2 - 1) - 4 * n^2 * \ln(n)^2]} \tag{7}$$

The parallel diaphragms of the mechanism have an equal displacement, but generate a different force at this displacement due to their difference in geometry. This means that they should be modelled as parallel springs, and allows to describe the spring stiffness of the entire mechanism using Equation 8.

$$k_{total} = k_{large} + k_{small} \tag{8}$$

It is critical that the mechanism returns to its original state therefore, it is required to construct the diaphragms out of an elastic material. For the material jetting process

there are three elastic materials available, Tango, TangoPlus and Agilus30. A commonly used material to construct rigid components by means of material jetting is Vero. The properties of these materials are listed in Table 7.

Using the dimensions for the outer diameter, internal diameter, and thickness for both of the diaphragms as listed in Table 6, as well as Equations 7 and 8, the total spring coefficient (k_{total}) was calculated for each of the elastic materials. The result of these calculations is shown in the last column of Table 7. It can be seen that none of the flexible materials would be suitable to create a mechanism with a total spring coefficient of 10000 N/m. Since the Poisson's ratio of Agilus30 is unknown, it was assumed that it was equal to that of Tango (0.3).

Since it was not deemed possible to construct a mechanism with the appropriate spring coefficient using the aforementioned base materials, it was decided to construct a series of prototypes with diaphragms that were constructed out of a mixture of the Agilus30 and Vero materials. The reason to choose these materials was that the external company that was selected to print the models, 3D LifePrints ltd., was only able to use a mixture of these two materials. It should be noted that it might be possible to create other material mixtures with varying mechanical properties, as there are other rigid and flexible materials available for the material jetting process.

5. Prototyping

5.1. Prototype Design

Because the Young's modulus and the Poisson's ratio of the digital materials is unknown, it was decided to print a series of prototypes made from a range of different materials which can be tested to examine their performance.

The final design of the prototypes was created in SOLIDWORKS 2017, a render of the final design of the prototypes is shown in Figure 28. An isometric view of the entire driving mechanism is shown, as well as a cross-section view that shows the internal structure of the driving mechanism. The outer surface of the driving mechanism is square because it is easier to fixate a square object when performing measurements. In an actual instrument the outer surface would be round to increase the gripping comfort of the user.

The dimensions related to the diaphragms are listed in Table 6, all other dimensions of the prototype are shown in the construction drawings in Appendix C. It was chosen to manufacture the diaphragms of the driving mechanism from three distinct ratio's of Vero and Agilus30. The chosen ratio's were 20/80, 50/50, and 80/20, these ratio's were chosen because they span a wide range of material ratio's. Since no data was available on the material properties it is useful to examine a large material range, as it is not accurately known how the materials will behave. Tests executed with samples made using these ratio's will be able to roughly estimate what material ratio is beneficial with respect to a particular property of the mechanism.

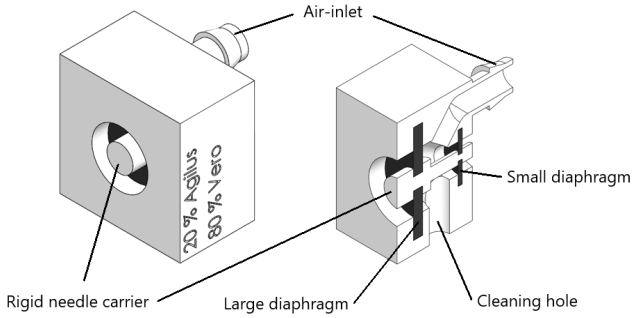

Figure 28. Render of the prototype used to evaluate the performance of a dual diaphragm drive mechanism.

The housing and the rigid needle carrier were both completely constructed out of the Vero material. This is due to the fact that it is desirable that these components are as strong as possible to withstand the air pressure, and to transfer the force to the cutting needle.

The final design of the prototypes does not allow for the attachment of the cutting needles, as it is not necessary when comparing the performance characteristics of the mechanism to current vitreous cutting instruments. Due to the high resolution of the material jetting process it should be possible to print holes of a sufficiently small size to mount currently used cutting needles. A second hole was added to the prototype in order to remove the support material inside, which can be sealed with a bolt in order to perform the tests.

5.2. Prototyping Details

In total 9 samples were printed on an Objet 260 Connex 3 printer, in two batches. The models were printed in two separate batches because it was at first unknown if the models could be successfully cleaned, and printed. Therefore, only three samples were printed at first to test this. This first print batch was successful, and a first set of performance tests was conducted. However, during these tests some of the samples failed before enough data could be collected. A second batch of 6 samples was printed in order to complete the tests. The materials that were used to construct the models were Vero and Agilus30. In Table 8 all the printed samples are listed as well as the material ratio's of the diaphragms. The layer height of the prints was 30 microns. The support material that was used was the 706b support material. This is a soluble support material, and was removed by soaking the parts for a minimum of 2 days in a solution of 97% water, 2% sodium hydroxide, and 1% sodium meta-silicate. The solution was kept at a temperature of 32 degrees. After soaking the parts, a small water pressure jet was used to clean off the remaining support material.

The additional cleaning hole required for removing the support material had a size of 5 mm. This hole was tapped with an M6 tap in order for it to be sealed with an M6

TABLE 8. SAMPLE MATERIAL RATIO'S

Sample name	Vero	Agilus30	Batch
20Agilus80Vero	20 %	80 %	1
50Agilus50Vero	50 %	50 %	1
80Agilus20Vero	80 %	20 %	1
20Agilus80Vero - 2.1	20 %	80 %	2
50Agilus50Vero - 2.1	50 %	50 %	2
80Agilus20Vero - 2.1	80 %	20 %	2
20Agilus80Vero - 2.2	20 %	80 %	2
50Agilus50Vero - 2.2	50 %	50 %	2
80Agilus20Vero - 2.2	80 %	20 %	2

Table showing the material ratio's of the printed samples used during testing, as well as the print batch of each respective sample

bolt. Care needed to be taken when tapping the hole, as the material had the tendency to pulverize into dust under the pressure of the tap. However, when a tapping set was used, and care was taken not to exert a large amount of force, it was possible to create an internal screw thread that had sufficient strength. All of the samples were tapped successfully. The M6 bolts used to seal the cleaning hole were made from A2 stainless steel and had a length of 10 mm. A 2 mm thick Nylon M6 washer was used as a spacer, and to create an air tight seal between the screw and the sample.

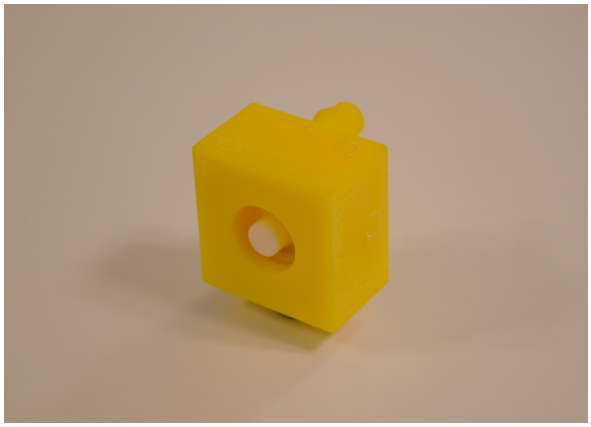

Figure 29. Photograph showing one of the finished prototypes that were printed using the material jetting printing process.

Unfortunately there were some differences between the two batches of samples. In the first batch, the outer surfaces were uniform and had a matte appearance. The surface finish on the samples in the second batch was not uniform and had mixed matte and glossy surface finishes. The difference in surface finish is related to the placement of the support material, after support material is removed it reveals a matte finish on the printed part. It is indicated that glossy surfaces have less defined edges than their matte counterparts. Furthermore, it is mentioned that glossy surfaces yield parts that have superior strength when compared to matte surfaces [130], [131].

In the first batch all surfaces on the air connectors were matte and had sharp defined edges. Attaching an air hose to the samples from the first batch was easy. A piece of Festo 10x1.5 tubing was heated with a Weller WXHAP 200 hot air blower until pliable, and then it could be manually pressed onto the connector.

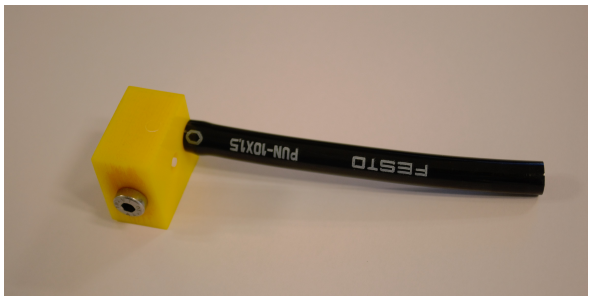

Figure 30. Photograph showing a sample from the first batch with the Festo tubing press fitted on the air connector.

In the second batch of prints it was observed that the angled portion of the air connector was glossy. When trying the aforementioned method to attach the tubing, the air connectors instantly broke off. It is suspected that the glossy surface led to a larger friction force between the tubing and the air connector, making it more difficult to press on correctly. For each of the samples in the second batch, a rigid 8 mm diameter Festo push in sleeve was turned down on a lathe to an outer diameter of 5 mm. Subsequently, it was glued into the hole of the air connector using Loctite 4061 glue. A photo of the finished air connector is shown in Figure 31.

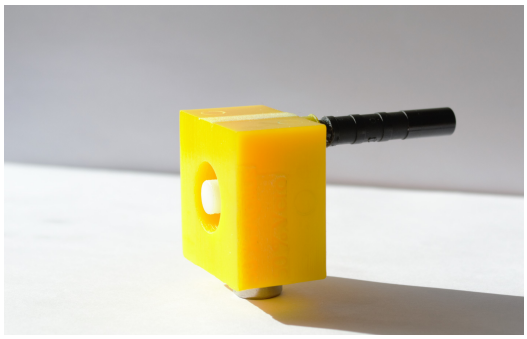

Figure 31. Photograph showing a sample from the second printing batch with its finished new air connector.

6. Testing

6.1. Testing objective

The goal of the tests is to evaluate if the non-assembly driving mechanism is capable of replicating the performance of the currently used driving mechanism. Therefore, three

separate tests were conducted: A spring measurement test, a displacement test and a force test.

The goal of the spring measurement test was to determine the amount of force that each sample exerts in the backward direction when it is displaced by 0.8 mm. This is the force that will be available for cutting vitreous during the backward stroke of the mechanism.

The goal of the displacement tests was to examine the change in position of the rigid needle carrier of each sample in response to an air pressure pulse. From this test the maximum displacement of the sample can be determined, as well as, the time it took the sample to move 0.8 mm forwards, and backwards in response to a particular air pressure pulse.

The force tests aimed to determine the amount of force that is generated by the sample when a particular air pressure is applied to the air chamber.

6.2. Variables

Independent Variables

The following variables were manipulated during the tests:

- *Displacement of rigid needle carrier* [mm]; The displacement of the rigid needle carrier is changed during the spring measurement test between 0 and a maximum value of either 1.3 or 2.1 mm.
- *Orientation of the sample* [Front/Rear]; During the spring measurement tests, the side of the rigid needle carrier which interfaces with the setup is varied. This is done by changing the orientation of the sample between the front and rear orientation in between tests.
- *Pressure* [Pa]; During the displacement and force tests, the pressure of the air which is applied to the sample is varied depending on the sample material. In the experimental procedure section, further details are given on the used pressure values.

Dependent Variables

The following variables were measured during the tests:

- *Spring force* [N]; The force which is exerted by the mechanism when it is displaced.
- *Spring coefficient of mechanism* [N/mm]: Spring coefficient of the mechanism.
- *Maximum displacement* [mm]; The maximum displacement of the rigid needle carrier in response to applied air pressure.
- *Time to reach 0.8 mm* [s]; Time it takes the rigid needle carrier to reach a displacement in the forward direction of 0.8 mm in response to applied air pressure.
- *Time to retract first 0.8 mm* [s]; Time it takes the rigid needle carrier to retract the first 0.8 mm after the pressure is vented from the air chamber.
- *Time to retract last 0.8 mm* [s]; Time it takes the rigid needle carrier to retract the last 0.8 mm before reaching its start position.
- *Force output* [N]; The force that is generated by the mechanism in response to applied air pressure.

6.3. Hypotheses

Spring measurement test

Due to the higher Young's modulus of the Vero material, it is presumed that the spring stiffness of the mechanism will go up along with the percentage of Vero present in the diaphragm material. The increased spring stiffness is expected to lead to an increase in cutting force during the backward stroke of the mechanism.

Displacement test

It is expected that the stiffer samples (20Agilus80Vero) will require a larger pressure to move the rigid needle carrier than the softer materials (80Agilus20Vero). However, it is expected that the stiffer samples will move the needle carrier backwards more quickly, due to the higher Young's modulus of the material. Furthermore, it is expected that higher pressures will lead to a faster forward movement in all of the samples. The 20A80V samples are presumed to be stronger and are therefore likely to withstand higher pressures.

Force test

It is expected that all the samples will have an approximately equal force profile as the displacement of the rigid needle carrier is zero, and therefore the influence of the diaphragm material is expected be non existent. The force measurements are expected to be comparable to the theoretically calculated force profile when the aspiration is zero, shown in Figure 27.

6.4. Spring measurement test

6.4.1. Experimental setup

The spring measurement tests were carried out using a Lloyd LS1EH tensile tester, with an integrated Lloyd 50 N load-cell. The tensile tester was connected to a PC, running Nexygen plus data collection software. Attached to the load cell was a tapered metal needle that could apply the load to the sample. The samples were clamped in a custom aluminium fixture which was attached to the base of the tensile tester. Two stainless steel M6 x 10 mm bolts were used to clamp the sample to the fixture. A rendering of this aluminium fixture with a clamped sample is shown in Figure 32. A photograph of the setup that was used is shown in Figure 33.

6.4.2. Experimental procedure

The spring measurements tests were performed by clamping the sample in the aluminium fixture and calibrating the tensile tester in such a way that the base position of the force needle was slightly above the rigid needle insert. The maximum displacement of the tensile tester was set to 1.3 mm for all samples, however a maximum displacement of 2.1 mm was also applied to three samples of the second batch. This was done to be able to observe the behaviour of the mechanism at larger displacement values. The head of

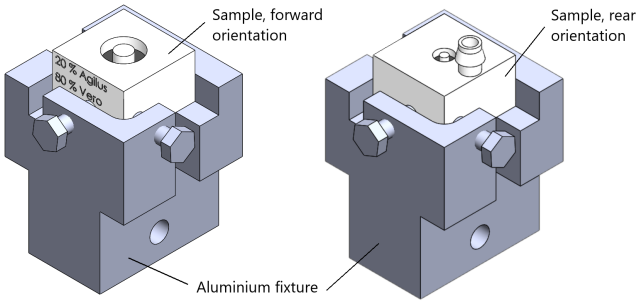

Figure 32. Rendering showing the aluminium fixture and the driving mechanism used for the spring measurement testing. Both the front and rear orientation of the sample are shown.

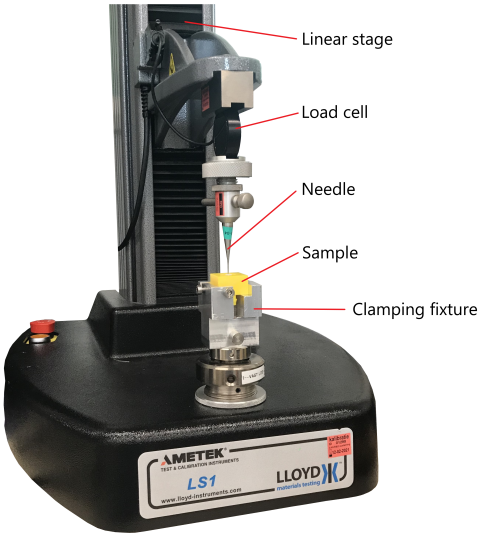

Figure 33. Photograph of the setup used to perform the spring measurement tests.

the tensile tester was lowered at a speed of 0.6 mm/min until the maximum displacement was reached. Once the maximum displacement was reached, the linear stage moved upwards with a speed of 0.6 mm/min until it reached its zero position, slightly above the sample. The load cell registered the force which was developed by the mechanism during the tests.

A schematic image showing the cross section of the sample during the execution of the test is shown in Figure 34. It shows how the tensile tester with the load cell moves down to displace the mechanism, and simultaneously measures the force with which the mechanism resists the displacement.

All of the samples were tested in two orientations, with the front surface of the needle carrier interfacing with the needle, and with the rear surface interfacing with the needle. A rendering showing both of the orientations can be seen in Figure 32. The 1.3 mm tests were repeated three times for each orientation of the sample. The 2.1 mm tests were only executed with a rear orientation of the sample. The reason for this was that the air connectors were installed in the second batch of samples after performing the 1.3 mm tests. The modified air connectors made it impossible to clamp the samples in the forward orientation. After the 2.1 mm displacement tests were completed, a leak test was performed by submerging the sample in water, while a pressure of 2 bar was being applied to it. If bubbles would appear out of the housing, or either of the diaphragms, it would indicate that a leak was present in the sample.

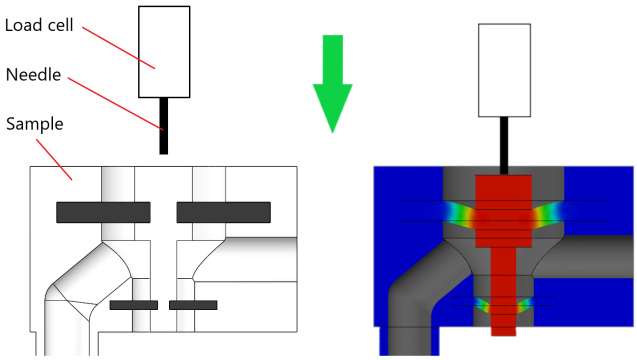

Figure 34. Schematic image showing the cross section of the sample during the spring measurement test. The force sensor with attached needle, mounted to the tensile tester moves down, thereby displacing the rigid needle holder of the mechanism.

6.4.3. Data analysis

Each of the measurements yielded two vectors, one containing the force data that was recorded during the measurement, and one that contained the displacement data of the tensile tester. Each vector was comprised of 1000 data points. The data analysis of all of the tests was performed in MATLAB R2018b. The moment when the load cell registered a force in excess of 0.03 N, was deemed to be the point at which the needle made contact with the sample. The displacement data was shifted to align the point of contact with the origin. This ensured that the displacement axis of the graph was equal to the displacement of the mechanism, and allowed to easily compare the data collected during different measurements. After shifting the data, the data was trimmed to remove excess data points.

In Figure 35 an example is shown of the data that is collected during a single measurement. The amount of cutting force generated by the mechanism at a displacement of 0.8 mm, was determined by finding the index of the last data point of the extension data that was bigger than 0.8 mm. The force value could easily be found, by looking up the force at the found index in the force vector. This point is shown in Figure 35 as a large grey cross.

Due to the linearity of the loading curve, it can be easily approximated how much force is required to displace the rigid needle carrier. The slope of the loading curve of each measurement was determined by dividing the maximum force value, by the maximum displacement of the rigid needle carrier.

The hysteresis area of each measurement was computed by calculating both the area under the loading, and the

unloading curve. The difference between both areas is equal to the hysteresis area.

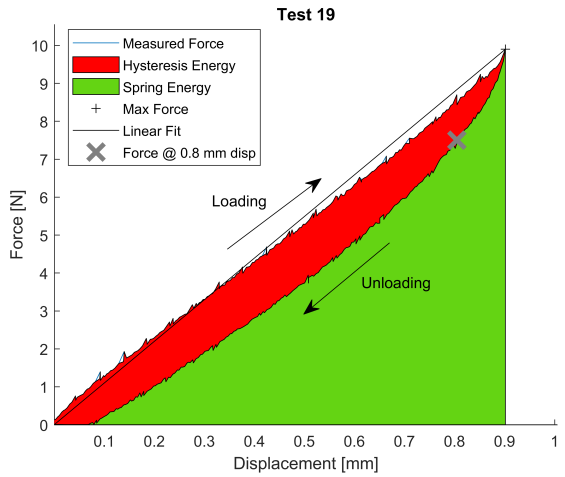

Figure 35. Plot showing an example of the measurement data from the spring measurement test. Several areas and points of interest are indicated in the graph that are used to compare the different measurements.

6.4.4. Results

The spring force which is developed by each of the samples at a displacement of 0.8 mm is shown in Table 9. It can be seen that only the stiffest samples (20Agilus80Vero) were able to reach a cutting force of more than 8 N, at a displacement of 0.8 mm. The other samples were shown to have similar spring force values around 3 - 4 N.

TABLE 9. SPRING FORCE AT 0.8 MM DISPLACEMENT

Sample name	Avg Force (n = 3), Front Orientation	Avg Force (n = 3), Rear Orientation
50Agilus50Vero	3.89 N	3.42 N
80Agilus20Vero	3.14 N	3.24 N
20Agilus80Vero - 2.1	9.82 N	9.80 N
50Agilus50Vero - 2.1	4.04 N	3.76 N
80Agilus20Vero - 2.1	3.53 N	3.51 N
20Agilus80Vero - 2.2	8.29 N	7.72 N
50Agilus50Vero - 2.2	3.41 N	3.31 N
80Agilus20Vero - 2.2	3.18 N	3.16 N

Table comparing the spring force at 0.8 mm displacement, during the 1.3 mm extension tests, of both sample orientations.

In Figure 36 the force vs displacement curve of the 1.3 mm extension tests are shown for all the tested samples. From Figures 36, and 35, it can be clearly seen that there is a difference in force between the loading, and unloading portion of the cycle. The loading part of the cycle corresponds to the amount of force which is required to displace the rigid needle carrier. The unloading part of the cycle is the spring force which is generated by the drive mechanism, and which could be used to cut the vitreous during the return stroke. It can also be observed that the loading part of the cycle is approximately linear between the starting point and the maximum registered force value. A plot of the average slope of the loading curve of the cycle was included for all samples, these are the black lines shown in Figure 36. In Table 10, the average slopes of the loading curves are shown for each of the samples. The results from this test show that the behaviour of the 50Agilus50Vero and 80Agilus20Vero materials are comparable, the samples made from the 20Agilus80Vero material are shown to be more stiff.

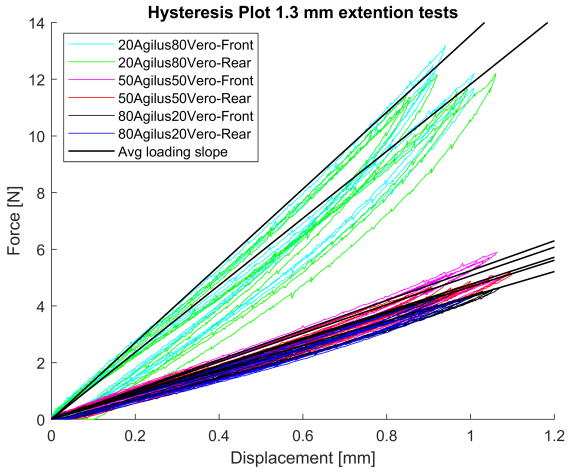

Figure 36. Plot showing the hysteresis curve for all samples with a maximum displacement of 1.3mm, as well as a plot of the average slope of the loading curve of each sample.

TABLE 10. SLOPE OF FORCE - DISPLACEMENT CURVE, 1.3 MM EXTENSION TESTS

Sample name	Average slope (n = 6)
50Agilus50Vero	5.06 N/mm
80Agilus20Vero	4.35 N/mm
20Agilus80Vero - 2.1	13.55 N/mm
50Agilus50Vero - 2.1	5.25 N/mm
80Agilus20Vero - 2.1	4.68 N/mm
20Agilus80Vero - 2.2	11.83 N/mm
50Agilus50Vero - 2.2	4.77 N/mm
80Agilus20Vero - 2.2	4.37 N/mm

Table listing the average slope of each sample during the loading part of the cycle of the 1.3 mm extension tests

Figure 36 also shows that the orientation of the sample does not have a large influence, this can be seen as the front and rear orientation curves for each of the samples are approximately equal. This observation is confirmed further when the spring forces at a displacement of 0.8 mm are compared for both orientations for each of the samples.

This data is shown in Table 9, and shows that the largest average force difference between the front and rear sample orientation is 0.57 N.

From the data it can be observed that the loading and unloading parts of the testing cycle do not coincide. This is an indication that there is a loss of energy in the form of hysteresis when actuating the mechanism. It can also be observed that the amount of hysteresis present in the mechanism was larger for the 20Agilus80Vero-2.1 & 20Agilus80Vero-2.2 samples, the other samples showed less hysteresis. The average hysteresis area for each tested sample is shown in Table 11.

TABLE 11. HYSTERESIS AREA

Sample name	Avg hysteresis area, 1.3 mm tests (n=6)	Avg hysteresis area, 2.1mm tests (n=3)
50Agilus50Vero	4.91	-
80Agilus20Vero	3.90	-
20Agilus80Vero - 2.1	9.60	-
50Agilus50Vero - 2.1	4.17	-
80Agilus20Vero - 2.1	3.64	-
20Agilus80Vero - 2.2	10.18	23.39
50Agilus50Vero - 2.2	4.87	15.01
80Agilus20Vero - 2.2	4.05	12.93

Table comparing the average hysteresis area's for all samples and 1.3/2.1 extension tests.

Three of the samples were also subjected to a larger downward displacement of 2.1 mm. Again, the force was evaluated on both the downward and upward movement of the linear stage. The results of these tests are shown in Figure 37 and Table 12. It can be seen that the maximum measured force is higher for all of the samples in the 2.1 mm tests, the slopes of the loading curve are comparable to the 1.3 mm extension tests for the 80Agilus20Vero, and 50Agilus50Vero samples. The average slope of the 20Agilus80Vero-2.2 sample is 2 N/mm lower in the 2.1 mm extension tests than in the 1.3 mm tests. In Figure 37, it can be seen that the spring measurements of the 20Agilus80Vero sample are lower for each subsequent measurement. This was an indication to check if the diaphragms of this sample were still intact. A leak test showed that there was a leak in the small diaphragm after performing the 2.1 mm extension tests.

TABLE 12. SLOPE OF FORCE - DISPLACEMENT CURVE, 2.1 MM EXTENSION TESTS

Sample name	Average slope (n=3)
20Agilus80Vero - 2.2	9.80 N/mm
50Agilus50Vero - 2.2	5.54 N/mm
80Agilus20Vero - 2.2	4.75 N/mm

Table listing the average slope of each sample during the loading part of the cycle of the 2.1 mm extension tests

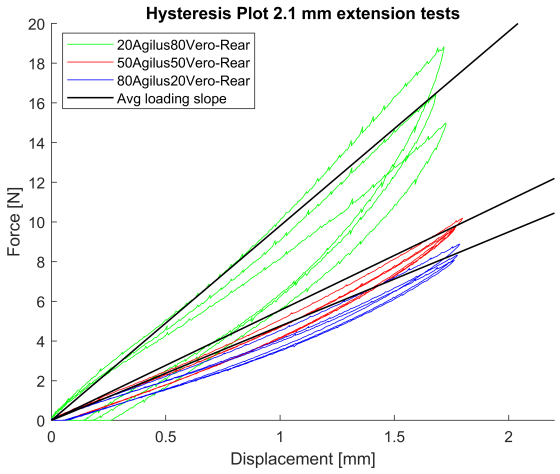

Figure 37. Plot showing the hysteresis loops of all samples with a maximum displacement of 2.1mm, as well as a plot of the average slope of each sample during the loading part of the cycle

6.5. Displacement test

6.5.1. Experimental setup

During the displacement tests the samples were clamped in a custom aluminium platform to which a Micro Epsilon ILD1420-10 laser sensor was mounted using two M2x25mm bolts. The aluminium platform intended to remove any relative movement between the sensor and the sample. The samples were fixed to the platform using four M3x30mm stainless steel bolts. The head of the bolts interfaced with a 1.5 mm thick steel plate which was placed on top of the sample. The sample was clamped in between the platform and the steel plate by tightening the bolts. The aluminium platform was custom made in the student workshop of the TU Delft using an Emco FB 4 mill. A rendering showing the mounting platform, the sample, and the laser sensor that were used in the displacement test, is shown in Figure 38.

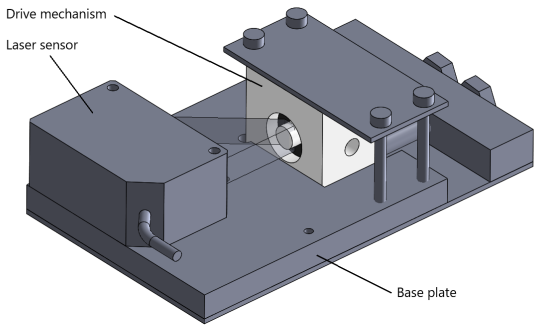

Figure 38. Rendering showing the components of the test setup to measure the displacement of the rigid needle holder.

A National Instruments NI USB-6008 was used as a data acquisition device, which was in turn connected to a PC running Labview to save the data. A GE PACE 5000 was used to apply the air pressure to the sample, it was

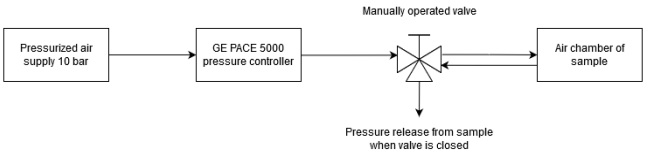

Figure 39. Schematic representation of the pressure setup that was used during the displacement and the force testing.

connected to a pressurized air supply of 10 bar. A valve was placed in between the PACE 5000 and the sample that was able to release the pressure from the sample when it was closed. A schematic drawing of the pressure circuit used in the displacement and force tests can be seen in Figure 39. A photograph of the test setup used in the displacement tests is shown in Figure 40.

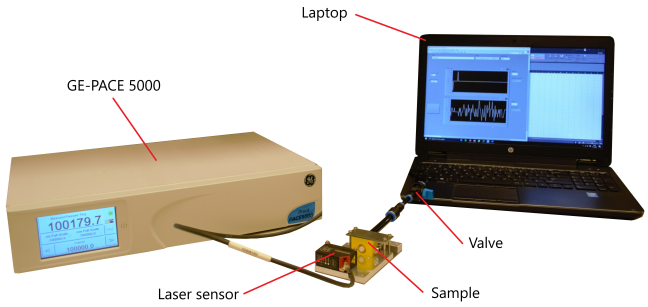

Figure 40. Photograph of the setup that was used to perform the displacement tests

6.5.2. Experimental procedure

The samples were mounted in such a way that no play existed between the sample and the rest of the setup. Next, the data collection would be started in the LabView program running on the PC. Subsequently, the intended pressure was set on the PACE 5000. When the PACE indicated that the pressure was constant, the valve between the PACE and the sample was opened, to allow the pressurized air to flow into the air chamber of the sample. The air pressure was applied until the displacement was deemed to be stationary, with a minimum duration of 60 seconds. When the displacement was observed to be stationary, the valve was closed, venting the pressure from the sample. The measurement would continue to run until the rigid needle carrier returned to its position at the start of the measurement, or until 2 minutes had passed, in which no movement of the rigid needle carrier was observed. Pressure was applied in increments of 10000 Pa for the 20Agilus80Vero samples, 5000 Pa for the 50Agilus50Vero samples, and 2500 Pa for the 80Agilus20Vero samples. Early tests revealed that these pressure changes led to a small measurable change in each of the samples. 5 out of the 6 tested samples were tested until failure.

6.5.3. Data analysis

First, the measurement data of the laser sensor was converted into the displacement of the rigid needle carrier, by compensating for the distance between the sensor and the sample, and the fact that the distance between the sensor and the rigid needle carrier becomes smaller as the mechanism extends. A plot of the converted data with the points of interest of a single measurement is shown in Figure 41.

It can be seen in Figure 41 that the raw measurement data contained some noise. This noise was filtered out using a 1 dimensional median filter, it was chosen to use this type of filter because it preserves sharp change points in the data. The maximum displacement value was found by searching for the largest value in the displacement data.

The time it took the sample to move 0.8 mm forward was determined as follows:

1) The first value in the filtered data set which is larger than 0.02 mm was taken as the start of the displacement.
2) Subsequently, it was checked at which time the displacement data was first equal to 0.8 mm.
3) Subtracting the time at the start of the displacement from the time at which the rigid needle carrier reached 0.8 mm, gave the time it took the needle carrier to move 0.8 mm forward.

The time it took the sample to move 0.8 mm backwards from the maximum extension was determined as follows:

1) The time at which the air pressure was vented was determined to coincide with a sharp change in the position of the mechanism after the maximum displacement had been reached (drop point).
2) Subsequently, it was determined at which time the displacement of the mechanism was 0.8 mm below the maximum displacement value.
3) Subtracting both times gave the time it took the mechanism to retract 0.8 mm from the maximum displacement.

The time it took the sample to move the last 0.8 mm of the backwards stroke, was determined by subtracting the time at which the sample reached a displacement of 0.8 mm for the second time, from the time when the position of the rigid needle carrier was within 0.03 mm from the starting position.

6.5.4. Results

During the displacement tests, pressure pulses of varying magnitude were applied to each of the samples, and the displacement of the rigid needle carrier was measured. The maximum displacement that was measured in response to a range of pressures is plotted in Figure 42.

A few things are immediately apparent, the first being that the material has a large influence on the maximum displacement that can be achieved at a certain pressure. It is also visible in the data that the relationship between the maximum displacement and the applied pressure is linear.

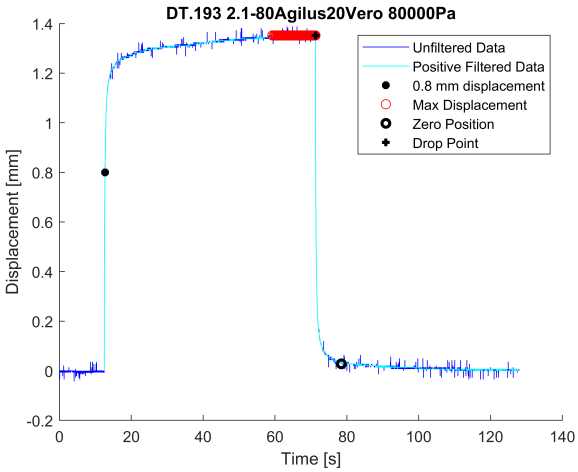

Figure 41. Plot showing an example of a single measurement of a displacement test with the points of interest highlighted in the graph.

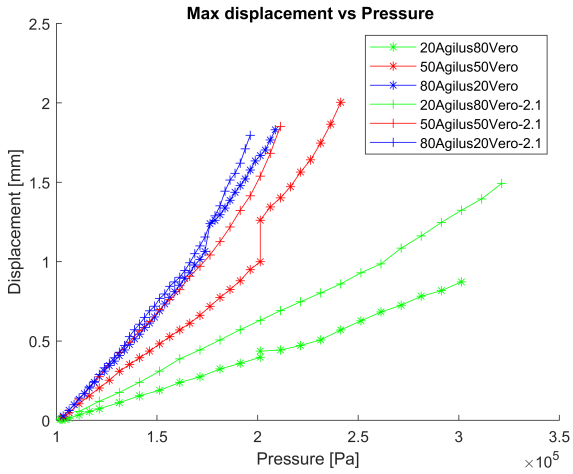

Figure 42. Plot showing the maximum displacement vs the pressure that was applied to each sample.

A jump in the data can be observed for the 50Agilus50Vero and the 80Agilus20Vero samples, at a pressure of 0.6 bar, and 1 bar respectively. Furthermore, it can be seen in the graph that the most flexible tested samples (80Agilus20Vero & 80Agilus20Vero-2.1) have a very similar behaviour. The other samples show more variation within their material group. In Table 13 the failure points of the samples are listed.

A plot showing the time it took each sample to move 0.8 mm forwards, vs the pressure that was applied to the sample, is shown in Figure 43. From the graphs it can be seen that the time decreases exponentially with increasing pressure. In Figure 44 the same plot is shown, only now the axis are arranged in such a way that the points with the fastest response are more clearly visible. It can be seen that the time it takes to reach a displacement of 0.8 mm can differ by a factor of more than 200, while the applied pressures differ by a factor smaller than 2.

It was also evaluated how long it took each sample to move 0.8 mm backwards from the maximum displacement. In Figure 45 this time is plotted against the maximum displacement of the rigid needle carrier. It can be observed that the time to move the first 0.8 mm backwards decreased sharply between a maximum displacement of 0.8 and 1.0 mm for all samples. After a maximum displacement of 1.4 mm, the movement time decreases more slowly, and appears to become constant for the 80Agilus20Vero & 80Agilus20Vero-2.1 samples. It can be seen that the 20Agilus80Vero-2.1 sample takes the longest time, the other samples have a similar behaviour. In Table 13 the time it took each sample to move 0.8 mm backwards from the overall largest displacement is listed.

Figure 46 shows the time that the samples took to move the last 0.8 mm backwards. The samples made from the 20Agilus80Vero material took significantly longer than the other samples, which showed comparable behaviour. The graph shows that the time is fairly consistent and does not seem dependent on the maximum displacement of the mechanism. The data shows that the time it takes each sample to span the last 0.8 mm of the movement lies between 5.59 and 73.3 seconds.

6.6. Force test

6.6.1. Experimental setup

The samples were clamped in a similar matter as in the displacement tests, the same aluminium platform was used

TABLE 13. DISPLACEMENT TEST FAILURE POINTS

Sample name	Max Displacement	Failure Pressure	Time to move 0.8 mm forward	Time to move 0.8 mm backward
20Agilus80Vero	-	-	-	-
50Agilus50Vero	2.00 mm	2.41 bar	0.175 s	0.258 s
80Agilus20Vero	1.83 mm	2.11 bar	0.183 s	0.326 s
20Agilus80Vero - 2.1	1.49 mm	3.31 bar	0.567 s	1.483 s
50Agilus50Vero - 2.1	1.85 mm	2.16 bar	0.156 s	0.180 s
80Agilus20Vero - 2.1	1.76 mm	1.98 bar	0.110 s	0.134 s

Table listing the failure points of all the samples which were tested in the displacement test, along with the times it took to move the needle carrier 0.8 mm forwards from rest, and 0.8 mm backwards from the maximum displacement

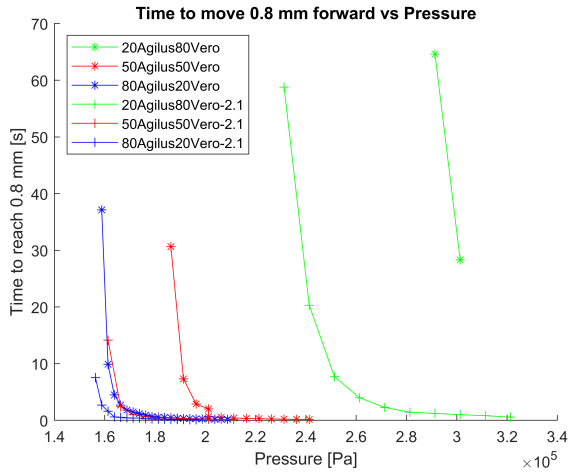

Figure 43. Plot showing the time it took to reach a displacement of 0.8 mm vs the applied pressure to the sample

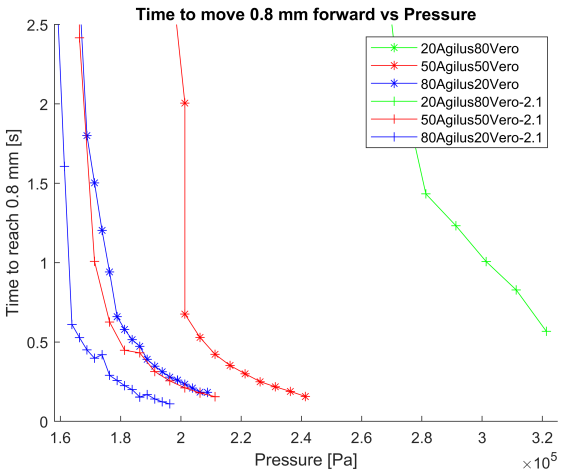

Figure 44. Zoomed plot showing the time it took to reach a displacement of 0.8 mm vs the applied pressure to the sample

to hold them. The difference was that during the force tests, a load cell was mounted to the aluminium platform instead of the laser sensor. A rendering of the force setup that was used can be seen in Figure 47. For the force measurements, a Futek mini load cell was used with a measurement range of up to 44.5 N. The load cell was connected to a Scaime CPJ2S analog signal conditioner, which was in turn connected to the aforementioned data-acquisition system that was used during the displacement tests. The load cell was fastened with an M3x5mm bolt to an L-bracket, which was in turn mounted to the aluminium platform. Another M3x5mm bolt with 6 stainless steel 0.5 mm spacer rings was mounted to the front of the load cell, to bridge the gap between the sensor and the sample. The pressure system that was used to apply the air pressure to the samples was identical to the one used during the displacement tests. The construction drawings of all the custom built components for the test setups can be found in Appendix C.

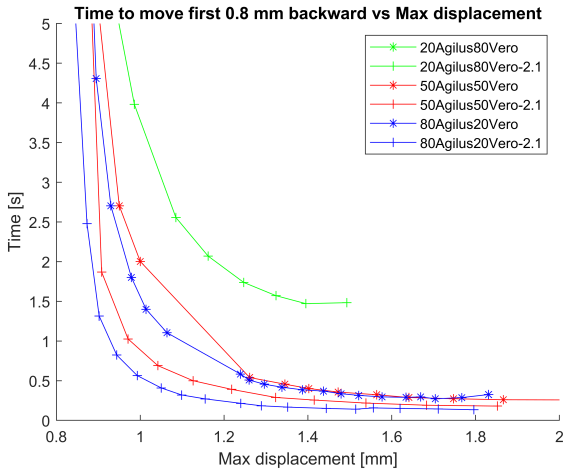

Figure 45. Plot showing the time it takes for the mechanism to move 0.8 mm backwards from the maximum displacement.

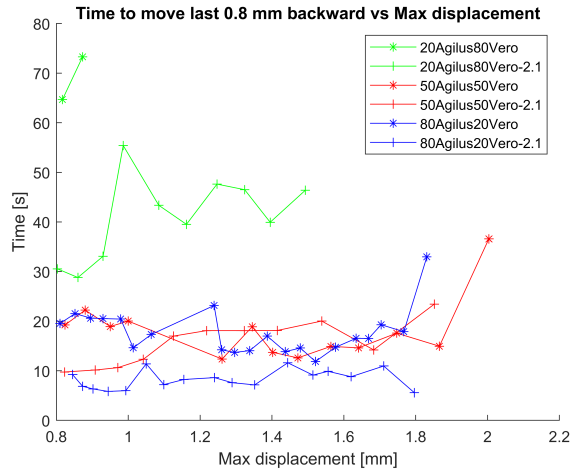

Figure 46. Plot showing the time it takes for the mechanism to move the last 0.8 mm before returning to its starting position.

6.6.2. Experimental procedure

The force tests were performed in the following manner: First, the sample was clamped in such a way that no relative movement was present. Subsequently, it was checked if the force sensor registered a positive reading. This was done to ensure that there was contact between the rigid needle carrier and the load cell. If there was no positive reading, the screw attached to the front of the load cell would be loosened slightly, or another 0.5 mm spacer ring was added to the setup. Care was taken not to develop a pre-tension force of more than 1 N, as this could have a negative impact on the accuracy of the test results. Once the force sensor was deemed to be in contact with the sample, the measurement would be started. Next, the desired pressure value was set on the PACE 5000. After the system indicated that the pressure was constant, the valve was opened, allowing the pressurized air to reach the sample. The pressurized air was applied for a duration of

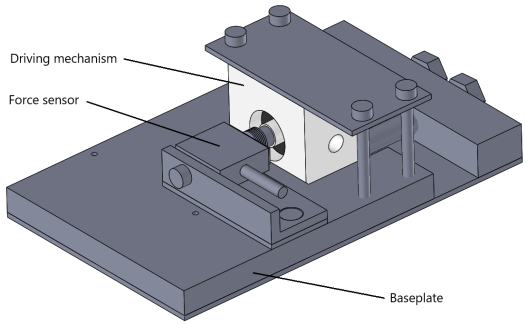

Figure 47. Rendering showing the components of the force measurement test setup.

20 seconds, as it was observed that the force would become stationary within that time for all measurements. After the 20 seconds had passed, the valve was closed, allowing the air pressure to vent from the sample. The measurement continued until the force returned to the value at the start of the measurement, or until it was deemed to be constant.

6.6.3. Data analysis

A plot showing the measurement data of a single force test is shown in Figure 48, along with the points of interest. To obtain the force which is generated by the mechanism, the pre-tension force is subtracted from all the datapoints. The third datapoint within each dataset was considered to be representative of the pre-tension force. From Figure 48, it can be observed that the raw force data also contained noise, this was filtered out using a 1 dimensional median filter. It can also be seen that there is a force spike in the data after the air pressure is applied to the mechanism. This spike is caused by the PACE 5000 system that is adjusting the air pressure to compensate for the increase in volume in the system once the air valve between the sample and the PACE is opened. This is therefore not indicative of the behaviour of the mechanism and should be filtered out. This is achieved by determining the maximum value within the latter half of the dataset. The maximum force can subsequently be plotted against the air pressure that was applied to the mechanism during that particular measurement.

6.6.4. Results

In Figure 49 the maximum force that is generated by the mechanism is plotted against the absolute air pressure in the air chamber. The calculated force output of the mechanism is also shown in the figure. It can be seen that the force output of all the tested samples is nearly identical. The measured values correspond to the calculated force output of the mechanism as calculated in section 4.7.1, for the case of no aspiration. Two of the five samples were tested until failure. The failure points of these samples are listed in Table 14. It can be observed that the pressure that could be applied before the samples failed was roughly a factor 2 higher than during the displacement tests.

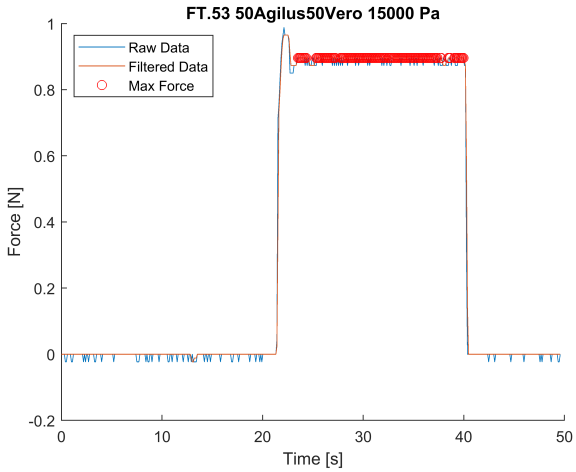

Figure 48. Plot showing an example of a single measurement of a force test, as well as the points of interest.

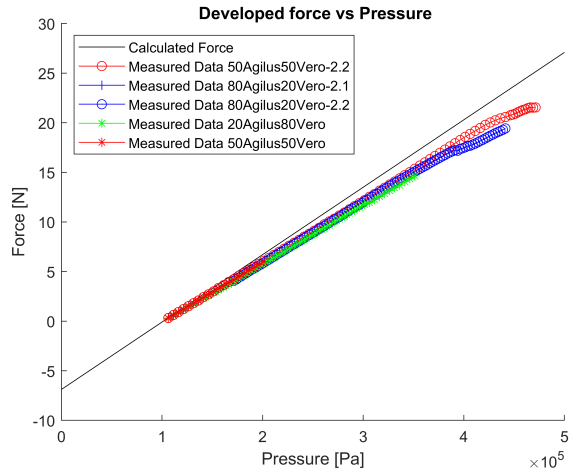

Figure 49. Plot showing the maximum force that was developed in response to the pressure that was applied to the sample. The calculated force output of the mechanism is also shown.

7. Discussion

7.1. Introduction

The goal of this study was: ”To create a non-assembly driving mechanism for a vitreous cutter that is designed for AM”. This study has shown that it is possible to successfully produce a non-assembly driving mechanism using the material jetting printing process. Additional development of the driving mechanism is needed as it currently does not have a comparable performance to currently used instruments. The tests revealed that none of the tested prototypes was able to achieve the desired actuation speed of 8000 PPM. The prototypes that came closest to being actuated at the desired speed were the 80Agilus20Vero samples, this was true for both the forward and the backward movements. In this chapter the test results will be discussed further along with several steps that can be taken to improve the design. It should be noted that although the current design does not

TABLE 14. FORCE TEST FAILURE POINTS

Sample name	Max Force	Failure Pressure
20Agilus80Vero	-	-
50Agilus50Vero	-	-
50Agilus50Vero - 2.2	21.7 N	4.68 bar
80Agilus20Vero - 2.1	-	-
80Agilus20Vero - 2.2	19.8 N	4.41 bar

Table listing the failure points of all the samples which were tested in the force test.

full-fill all of the requirements, it is encouraging that it is possible to manufacture a true scale, non-assembly driving mechanism using AM.

7.2. Interpretation of the test results

7.2.1. Spring measurement test

In currently used instruments there is no or very little hysteresis due to the use of metal return springs. The tests show that there is considerable hysteresis in the tested samples, this is not desirable as it indicates that energy is lost in actuating the mechanism. The results show that there is a difference in the amount of hysteresis depending on the material type of the sample. The samples made with the 20Agilus80Vero material have a larger hysteresis area than samples made from the other two materials. These tests show that the Agilus30 material is more capable of storing and releasing energy, as the samples with the highest percentage of Agilus30 have the smallest average hysteresis area. The amount of hysteresis is also dependent on the displacement of the mechanism as the amount of hysteresis in the 2.1 mm tests was seen to be larger than in the 1.3 mm tests.

The hypotheses was that the stiffness of the mechanism would go up along with the percentage of Vero that is present in the material. This is confirmed by the test results ,as the average slope of the loading curve is the steepest for the 20Agilus80Vero samples, and the lowest for the 80Agilus20Vero samples. However, the stiffness of the mechanism does not increase linearly with the percentage of Vero. This can be observed by the fact that the behaviour of the 50Agilus50Vero samples is very similar to the 80Agilus20Vero samples. It was expected that the 50Agilus50Vero samples would have a very distinct behaviour somewhere in the middle between the stiffest and most flexible samples. This shows that the Agilus to Vero ratio does not influence the spring behaviour to a large degree, when the material ratio is somewhere between 80/20 and 50/50. The tests also show that the behaviour of the mechanism is similar in both the front and rear orientation. This was expected, as the construction of each of the diaphragms was symmetric around their centre plane.

The results show that the spring force is not linear in the tested samples, while it is linear in currently used instruments. Furthermore, in current vitreous cutters the spring inside the mechanism is pre-loaded, allowing the instrument to apply a more constant cutting force in the backward direction. The newly developed driving mechanism does not have the ability to deliver a constant cutting force in the backward direction due to the fact that it is constructed in its neutral position, and does not have the ability to be pre-loaded. When the mechanism is displaced, the spring force is generated that drives the mechanism backward. In currently used instruments the cutting force in the backward direction is approximately 8 N over the entire stroke. The results show that a spring force of 8 N can be generated in the samples constructed out of the 20Agilus80Vero material, when the displacement of the mechanism is approximately 0.8 mm. The other samples were not capable of reaching a spring force of 8 N within a displacement of 0.8 mm. The results of the 2.1 mm extension tests show that the average displacement required to reach a spring force of 8N, is 1.59 mm for the 50Agilus50Vero-2.2 sample, and 1.73 mm for the 80Agilus20Vero-2.2 sample.

From the tests it can be concluded that a spring force of 8 N can be generated by the 20Agilus80Vero samples at a displacement of approximately 0.8 mm. This should be sufficient to cut the vitreous at the start of the return stroke. However, the spring force is not constant over the stroke, and drops as the mechanism returns to its neutral position. When it is assumed that a minimal cutting force of 7 N is required to cut vitreous, and the mechanism is constructed out of the 20Agilus80Vero material, the mechanism will be able to start a cut on the backward stroke, but will likely jam once the spring force falls below 7 N, which happens after the mechanism moves 0.1 - 0.2 mm backwards. It should be noted that it currently is unknown how much force is required to successfully cut vitreous, and that the cutting range of the instrument is smaller than the range of motion. If for instance a force of 2 N would be sufficient to cut the vitreous, the mechanism would deliver the appropriate amount of force over the first 0.4 mm of the backward stroke. As the cutting ports have a length of 0.4 mm, this could be sufficient to cut the vitreous. Since the required cutting force of vitreous is unknown, no definitive conclusion can be drawn if the appropriate amount of cutting force is generated by the new driving mechanism on the backward stroke.

7.2.2. Displacement test

The displacement tests show that all of the tested samples were able to reach a displacement of 0.8 mm. Furthermore, it can be seen that the relationship between the applied pressure and the displacement of the rigid needle carrier is fairly linear. A jump can be seen in the data shown in Figure 42 for the 80Agilus20Vero & 50Agilus50Vero samples. The cause of this jump is unknown, however, it marked the point in the data where the measurements were taken on different days for the respective samples. Perhaps the samples degraded somewhat overtime resulting in a larger displacement of the rigid needle carrier.

The samples with the lowest percentage of Vero reached a displacement of 0.8 mm at lower pressures than the

other materials. This behaviour was expected as these samples are the most flexible. It should be noted that the 50Agilus50Vero-2.1 sample showed a similar behaviour to the 80Agilus20Vero samples, this result is in agreement with the results from the spring force measurement test, but was unexpected prior to testing. This again leads to the assumption that the Agilus/Vero material ratio does not have a significant influence on the mechanism behaviour, if it is between 80/20 and 50/50. The 20Agilus80Vero samples required the highest pressures to reach a displacement of 0.8 mm, this was expected as the Vero material has a higher Young's modulus than that of Agilus30.

As is mentioned in the requirements section 4.1, it is the goal to move the needle with a speed of 8000 PPM or 133 Hz. This means that the available time to complete a cutting cycle is approximately 0.0075 seconds. In this time the mechanism needs to extend 0.8 mm in the forward direction, come to a full stop, and return backwards to its starting position. This means that the time for the individual movements of the mechanism is 0.00376 seconds. The time it took for each of the samples to reach a displacement of 0.8 mm was highly influenced by the air pressure that was applied to each sample. It can be seen that the samples with a low percentage of Vero were more responsive and reached the required displacement in a shorter time span. It should be noted that none of the tested samples were able to perform the forward movement of the mechanism within 0.00376 seconds before they failed. The fastest time that was recorded for a sample to move 0.8 mm, was 0.11 seconds at a pressure of 1.98 bar.

The return movement of the mechanism was also analysed by examining the time it took the mechanism to move backward by 0.8 mm from the maximum displacement that was measured. The results again show that the 80Agilus20Vero samples had a similar behaviour to the 50Agilus50Vero samples. The 20Agilus80Vero sample that was tested was distinctively slower than the other samples for all maximum displacement values. This result was unexpected prior to testing, as it was assumed that the increased stiffness of the material would lead to a more responsive mechanism. The results from this test show that this is not correct and that the more flexible samples were in fact more responsive. Therefore, it can be concluded that the Vero material has a negative influence on the movement speed of the mechanism in both the forward and backward directions. The sample with the best performance was 80Agilus20Vero-2.1 with a time of 0.134 seconds to retract the first 0.8 mm. This means that all the samples that were tested took too much time to retract to be able to operate the mechanism at the desired speed of 8000 PPM.

An interesting result was discovered when it was examined how much time was required for each sample to retract the final 0.8 mm when the air pressure was vented. This did not seem to be influenced by the maximum displacement of the mechanism, but was fairly constant across all measurements. It can be seen that the fastest time was 5.56 seconds and that the slowest time was approximately 75 seconds. This shows that the tested samples took a relatively long time to return to their neutral position when compared to the intended actuation time of 0.00376 seconds. Since the return times of the last 0.8 mm of the backward stroke are much longer for all samples than the times of the first 0.8 mm, it can be concluded that the speed of the mechanism varies greatly over the stroke. This result also indicates that ideally there should be a pause of at least 2 minutes in between successive measurements to ensure that the samples have enough time to return to their neutral position. During the tests this was not yet known, as it was revealed when performing the data analysis, and as a result several tests were executed before the samples were completely in their neutral position.

7.2.3. Force test

The force tests revealed that the relationship between the applied air pressure and the developed force by the mechanism when it is constrained in its neutral position is linear. This was expected, as it is in agreement with the performed calculations described in section 4.7.1. Furthermore, it is shown that all the tested samples develop equal forces at equal pressures, confirming the hypothesis. According to the requirements a forward force of 9 N should be generated to have a comparable performance to current instruments. From Figure 49 it can be seen that this force can be reached in all samples at the start of the stroke when an air pressure of 2.5 bar is applied to the sample.

The force at the end of the forward stroke could not be determined with the test setup used in this study, as it was not possible to create a gap of 0.8 mm between the rigid needle carrier and the force sensor. However, from the spring measurement tests it is shown that the slope of the loading curve is between 13.5 N/mm and 4.37 N/mm depending on the sample. These values can be used to approximate the required force to displace the sample by 0.8 mm, which is between 10.8 N and 3.50 N for all samples. The maximum measured force during the force test was approximately 20 N. When the required displacement force is subtracted from the maximum force, it can be seen that the approximately available cutting force is 9.2 N for the stiffest, and 16.5 N for the softest samples. As both of these values are above 9 N, it can be assumed that the mechanism is able to create an appropriate cutting force in the forward direction over the entire length of the stroke for all tested materials.

An unexpected result occurred with regards to the pressure at which two of the tested samples failed during the test. From the displacement tests it can be seen that the pressure at which the 80Agilus20Vero & 80Agilus20Vero-2.1 samples failed was approximately 2 bar. During the force tests the 80Agilus20Vero-2.2 sample was able to withstand an applied pressure in excess of 4 bar, without showing any signs of leakage. The most significant difference between both tests is: that the mechanism could move freely during the displacement tests, but was constrained in the forward direction during the force tests. This leads to the conclusion that the amount of displacement plays a huge role in the ability of the mechanism to withstand a certain pressure. This can have a significant influence on the lifetime of the

mechanism as well as, the performance characteristics as it is demonstrated that the actuation speed of the forward movement is highly correlated to the pressure which is applied to the mechanism.

7.3. Limitations of this study

A limitation of the prototyping process was that the location of support material was determined by 3D life prints, this was also true for the printing direction. Unfortunately, these parameters were not kept constant for all the printed samples and led to a noticeable difference in strength of the air connector. Since it is known that the printing direction can influence the strength of a printed part, its desirable to keep the printing direction identical for all samples. A solution would be to communicate clearly to production partners that the need for consistency is paramount, and discuss specifically the placement of support material as well as the printing direction in relation to the part.

The results from the force measurement show that the PACE 5000 takes some time to re-establish the correct pressure once the valve between the PACE and the sample is opened. This is due to the fact that the PACE 5000 needs to compensate for the extra volume inside the tubing which connects the sample to the setup, and the volume of the air chamber inside the sample. A solution to this would be to place a pressure tank in between the PACE 5000 and the valve. The tank should have a large volume when compared to the volume inside the tubing and the volume of the air chamber. This will ensure that the pressure remains more constant when the valve is opened as the additional volume is negligible when compared to the pressurized volume of the tank. This could increase the accuracy of the measurements with regards to the time it takes for each sample to reach a forward displacement of 0.8 mm.

To ensure that the sample was always in contact with the force sensor, the screw attached to the load cell was adjusted in such a way that the load cell registered a positive value. Unfortunately, it was not possible to make this value consistent for all the samples, this might be due to manufacturing tolerances and the different stiffnesses of the diaphragm materials. Another downside to this method is that the force measurements are in theory less accurate due to the pre-tension that is applied to the mechanism. To mitigate this effect, it was ensured that the positive load was as small as possible when performing the tests. In future experiments the accuracy might be increased by being able to make small adjustments to the position of the force sensor or the sample. If these adjustments can be made repeatably and are sufficiently small, the positive load can be made equal for all samples and can be potentially lower, leading to more accurate results.

The test setup that was used only allowed to measure the force at the start of the forward stroke, this made it impossible to verify that the mechanism has the appropriate force profile across the entire stroke. This could be solved by creating another test setup, where there exists a gap of 0.8 mm between the force sensor and the rigid needle carrier of the sample. When air pressure is applied to the sample, it can be examined if the amount of force measured by the load cell is adequate to cut vitreous.

Another limitation of the tests was that no aspiration pressure was applied to the mechanism when the force, and displacement tests were conducted. In actual procedures at some point aspiration pressure will be applied to the instrument. Therefore, it should be examined how the mechanism behaves in response to the aspiration pressure. It is expected that the force which is generated by the mechanism will be 2.3 N lower, as is shown in section 4.7.1. The displacement of the mechanism can also be negatively influenced by the aspiration pressure, as well as the response time of the mechanism. When developing the mechanism further, it is therefore relevant to conduct additional tests that are able to show the influence of the aspiration pressure on the mechanism behaviour.

7.4. Recommendations

7.4.1. Design Recommendations

Several improvements could be made to the design of the mechanism that might result in an increase of performance or a reduction in manufacturing complexity. The first improvement being that the shape of the chamber could be designed in such a way that it is optimized for AM by minimizing the amount of support material that is required. This could potentially lead to the elimination of the secondary hole required for support removal, as less support material is used to support the air chamber. Minimizing the support material could be achieved by integrating a rigid porous structure inside the air chamber that supports the top of the chamber during printing. Another option to reduce the amount of required support material is to print the top half of the air chamber with inclined walls that have an angle of 82 degrees or larger, as this is the smallest self supporting angle for the material jetting process. This will increase the size of the instrument, but perhaps could eliminate the need for most of the required support material. Both of these options would still require some support material as the rigid needle carrier is suspended in the air chamber which requires it to be supported on the bottom surface. This problem might be solved by printing a porous support structure inside the air chamber which is made from a flexible material. Because of the nature of the flexible material it might be permanently connected to the needle carrier, as well as the air chamber while still allowing it to move without requiring a lot of additional force. The durability of this internal structure does not matter as its function is to provide support during printing.

Another improvement that could be made is related to the air connector of the design. It was observed that a small amount of air leaked from the connector. The connector used in this study was not based on a standard design, and the tubing was not taken into consideration when designing the connector. These two factors may have led to the small air leak, therefore, it is recommended to incorporate a standard-

ized connector design which is compatible with commonly available tubing.

During the force tests, the pressure that could be applied to the samples before they failed was approximately 2 times higher than during the displacement tests. The main difference between these tests was that the mechanism was constrained during the force tests, and was completely free to move during the displacement tests. It is therefore interesting to incorporate a stop in the mechanism to constrain the movement of the rigid needle carrier to 0.8 mm. Subsequently, it has to be determined if the stop allows for a larger air pressure to be applied before the mechanism fails. The increase in air pressure might result in a higher forward movement speed of the rigid needle carrier, and therefore, a shorter time to displace it by 0.8 mm in the forward direction. The presence of a stop will not increase the speed of the backward motion, as the backward motion is generated by the spring rate of the diaphragms.

The executed tests also revealed that the spring force was insufficient to ensure that the rigid needle carrier returned to its initial position with sufficient speed. It can be seen that the time it took the mechanism to move 0.8 mm backwards was fairly constant when the mechanism was displaced in excess of 1.4 mm. The time it took for the rigid needle carrier to move back the last 0.8 mm varied in between samples but was otherwise consistent. However, the times that were observed where too long, as they were in between 5.59 and 73.3 seconds depending on the sample. A way to improve the behaviour of the mechanism in this regard might be to incorporate a rigid spring structure into the diaphragm. Previous research has been done to construct planar springs by means of AM. If these springs can be integrated into the mechanism or the diaphragms, perhaps it is possible to generate a sufficiently high force to achieve the desired speed of the mechanism in the backward direction. Future research could be done to check if this is a viable solution.

It was observed during testing that 8 out of the 9 samples failed at the small diaphragm, it can therefore be assumed that the strength of the small diaphragm plays a large role in the performance of the mechanism. Therefore, it is recommended to focus future design efforts on decreasing the internal stresses of the small diaphragm. This could for instance be done by increasing the ratio between the outside diameter and the diameter of the rigid centre, by decreasing the thickness, or by decreasing the Young's modulus of the material that is used to construct the diaphragm.

7.4.2. Future research

It is relevant to do additional research into the material properties of all known digital materials. Currently there is not enough known about the material properties of digital materials to design a diaphragm using diaphragm design theory. Especially the Young's modulus, Poisson's ratio and the ultimate tensile strength are relevant parameters to determine. With this information it will be possible to determine more accurately if a diaphragm will have the appropriate characteristics to be used in a driving mechanism for a vitreous cutter. Another benefit of having accurate material properties is that finite element models can be constructed of a particular design that predict the behaviour of the mechanism. These models could also be used to perform a topology optimization which can fine-tune the placement of materials with different properties to achieve a desired behaviour. Additional research could also be performed by conducting additional experiments using prototypes that are constructed using different digital materials, to examine whether they have better performance characteristics.

Another suggestion for further research is to determine the amount of force that needs to be generated by the mechanism to cut vitreous. This information is relevant as the spring force of the mechanism is not linear, and not constant over the stroke. Additional information on the required spring force is necessary to determine if the mechanism generates the appropriate amount of spring force to cut vitreous.

In the requirements it is stated that the lifetime of the driving mechanism should exceed 300,000 cycles, it is therefore recommended to study the lifetime of the driving mechanism in future studies. During this study the lifetime of the mechanism was not evaluated as it was unknown what pressure should be applied to achieve the desired behaviour of the mechanism.

The tests show that the speed of the return motion is too low when a combination of Agilus and Vero material with a material ratio between 20/80 and 80/20. Adding a pre-tension to the mechanism will not solve this issue, as the return speed is still too slow when the mechanism is displaced by 1.8 mm for all of the samples.

The current thickness of the large diaphragm was chosen to be near the upper limit, in order for it to generate a spring force to move the needle backwards. In concept variation B, the needle is moved backwards using a second pressure pulse. The thickness of the large diaphragm can therefore be reduced, the advantage of this is that it will require less energy to move the mechanism forwards. It is likely that this will reduce the response time of the mechanism. For these reasons it is therefore recommended to develop prototypes of concept variation B, and conduct similar displacement and force tests as have been described in this study. It should be noted that concept variation B requires a more intricate air supply system, as two pressure pulses need to be applied to the mechanism at specific points during the cutting cycle. However, instruments are currently on the market that use dual actuated diaphragm mechanisms which also require such air supply systems. Therefore, it is proven that it is possible to create a system which is capable of delivering two pressure pulses with sufficient properties to actuate a vitreous cutter.

7.5. Future outlook

This study shows that it is possible to additive manufacture a mechanism on true scale which creates the desired movement without any further assembly. Testing shows that additional steps have to be made to ensure that the mechanism is able to operate at the desired speed. There are multiple

ways in which this could be achieved. The first being that new materials could be developed which are both strong, and able to release internally stored spring energy. More research into other digital materials and their properties could also reveal materials which are already available, but were not considered in this study.

Another option is to develop concept variation B further. This variation does not rely on the spring force which is generated when the mechanism is displaced. Therefore, a different set of material properties are important in the embodiment of this concept variation, which could lead to an improved function.

Besides these points related to the function of the mechanism, improvements in the manufacturing process are also needed in order for future instruments to be instantly usable after printing. The most important being that the secondary cleaning hole needs to be made redundant, as it would otherwise need to be sealed. It is expected that this could be achieved by integrating porous structures inside the air chamber, eliminating the need for removable support material.

7.5.1. Non-assembly vitreous cutter design

This section aims to describe the design of two future instruments that are based on concept variations A, and B. Figure 50 shows a rendering of the cross section of the future instrument based on concept variation A. It can be seen that there are several hollow spaces inside the model however, all of them have a connection to the outside world. This means that in theory these connections could be used to remove the support material. The non-assembly driving mechanism can also be seen with its distinctive small and large diaphragms that seal the air chamber. In between the diaphragms there is a rigid needle carrier that is connected to the inner cutting needle. The outer needle is connected to the housing and is stationary. The needle carrier interfaces with a stopping surface constructed inside the handle. This stopping surface limits the forward movement of the mechanism. Tests of the prototyped driving mechanism have shown that such a stopping surface could lead to increased performance. Current AM technologies are not yet able to print the cutting needles with sufficiently high tolerances and quality. However, the future instrument that is proposed here could be manufactured in a non-assembly manner without printing the needles. Examples have been found in the scientific literature where parts were inserted in the assembly during printing [132]. If the instrument would be printed in the orientation as shown in Figure 50, slightly above the middle plane, the needles could be placed in the mechanism, and the printer could continue printing on top of the needles. In Figure 51 a schematic representation of the embedding steps is shown. The tolerances on the used printing method are 0.1 mm which is large for the degree of precision that is required in the currently used instruments. However, it is expected that future printers will be able to print parts with tighter tolerances in the future due to the continued development.

The size of the handle of the proposed instrument is comparable to that of current instruments, with the diameter of the latter being 15.7 mm, and the proposed one being 22 mm. The length of the current instrument handle is 40 mm and the length of the proposed instrument handle is 35 mm. It should be noted that design optimizations could decrease the diameter size by investigating the minimal wall thicknesses that are required for a successful print. The length of the handle can also probably be reduced further by optimizing the amount of contact that is required between the outer needle and the handle. The length can be further reduced by making the air chamber as small as possible, as an example a chamber of arbitrary size is shown. However in theory the size of the air chamber only needs to be slightly larger than the diameter of the air inlet line entering it.

A rendering of the future instrument based on concept variation B is shown in Figure 52. The instrument is different from the one based on concept variation A in the fact that it utilizes an additional diaphragm. The thickness of

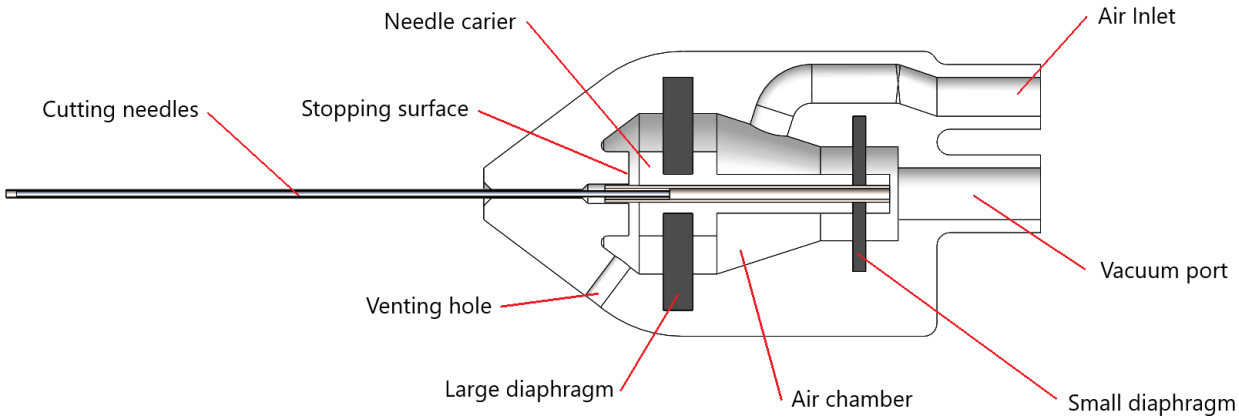

Figure 50. Rendering showing the cross section of a future dual diaphragm instrument

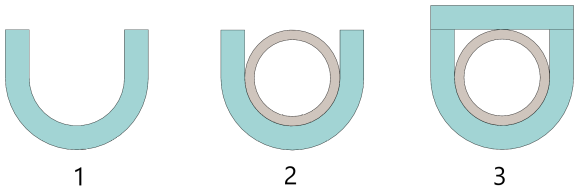

Figure 51. Showing the three steps of the embedding process of traditionally manufactured components during AM. 1: Printing the base plus supporting walls to align the component, 2: Inserting the component, 3: Printing the remaining layers to fix the component in position.

the large diaphragm can be reduced, due to the fact that it does not have to generate a spring force to move the cutting needle backward. The instrument does have an additional air chamber, and air inlet to apply air pressure pulses on both sides of the diaphragm. To accommodate the air inlet that feeds into the most forward air chamber, the diameter of the handle was increased from 22 mm to 24.4 mm. It should be noted that future design efforts can reduce this diameter when the instrument is designed asymmetrically. It can also be noticed that the instrument has two stopping surfaces, one at the front of the handle, and one at the rear at the vacuum port. This is done to limit the movement of the instrument in both directions. Besides these differences, both of the future instruments are identical.

8. Conclusion

In this study a new innovative driving mechanism was developed consisting of two asymmetrical diaphragms that seal an air chamber on opposite sides. The driving mechanism was manufactured using the material jetting process, in true scale, and did not require any additional assembly steps before use. The mechanism which is developed in this study has not been observed in any other vitreous cutter, and to the knowledge of the author not in any other device.

This study shows that the mechanism exhibits an appropriate displacement of the rigid needle carrier when loaded with pressure. Additional research is needed to optimize the design as the actuation speed is currently too slow to reach the desired cutting speed of 8000 PPM. However, several areas are highlighted that reveal design space which was not explored in this study. Future research could explore these areas further to see whether they lead to new mechanisms with improved performance. The author believes there is a high likelihood that this could be the case, as one of the proposed concept variations relies on a different set of material properties to create optimal performance. Continued development of the proposed design space may lead to instruments which are manufactured by means of AM in a single production step. This could lower their cost, and contribute to a future where surgical instruments are manufactured on site, and on demand.

9. Acknowledgements

First and foremost I want to thank my daily supervisors Kirsten Lussenburg and Marta Scali, they helped giving direction to my project and always made time for me when I requested it, which I greatly appreciated. I also want to thank DORC international as a whole for the opportunity to perform this thesis as part of a graduate internship in the R&D Instruments team. This gave me unique access to a lot of material which enhanced the quality and applicability of the work described in this thesis. In particular I want to thank Mart Gahler for bringing me in contact with the appropriate people to assist me with the experimental setup and measurements. Jos van Driel was very helpful in providing the appropriate sensors and data collection systems as well as, the labview program to log the data. Lastly I want to thank Paul Breedveld for inspiring me to graduate at the BITE department of the TU Delft and for the discussions over the course of the project.

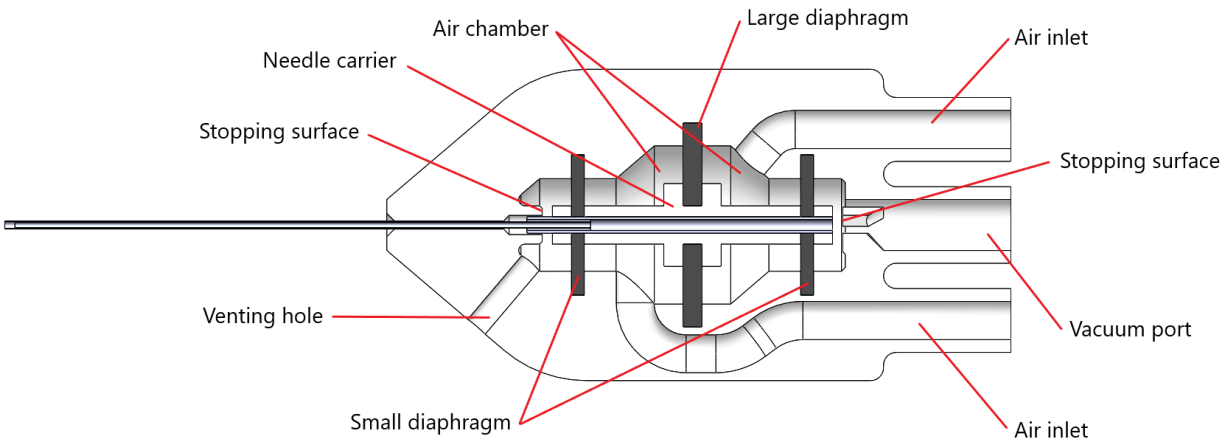

Figure 52. Rendering showing the cross section of a future instrument based on concept variation B

References

[1] Centraal Bureau voor de Statistiek. (2019) Medisch specialistische zorg; personen, diagnose en inkomen. Accessed: 4 May 2020. [Online]. Available: https://opendata.cbs.nl//CBS/nl/dataset/84480NED/table?searchKeywords=netvlies

[2] J. Sebag, *Vitreous: In health and disease*. Springer New York, 01 2014.

[3] A. Kumar, *Retina: Medical & Surgical Management*. Jaypee Brothers,Medical Publishers Pvt. Limited, 2018.

[4] T. Mimura, T. Nakashizuka, and M. Mori, "Recent advances and history of vitreous surgery," *Journal of Healthcare Engineering*, vol. 2, pp. 447–458, 12 2011.

[5] I. J. Constable and M. Nagpal, "Proliferative vitreoretinopathy," in *Retina*. Elsevier, 2013, pp. 1806–1825.

[6] J. F. Arevalo, M. H. Berrocal, J. D. Arias, and T. Banaee, "Minimally invasive vitreoretinal surgery: is sutureless vitrectomy the future of vitreoretinal surgery?" *Journal of ophthalmic & vision research*, vol. 6, no. 2, pp. 136–144, 2011.

[7] R. S. Snell and M. A. Lemp, *Clinical Anatomy of the Eye*. Wiley-Blackwell, 12 1997.

[8] E. Marieb and K. Hoehn, *Human Anatomy & Physiology*. Pearson Education, 2010.

[9] V. Narendran and A. Kothari, *Principles and Practice of Vitreoretinal Surgery*. JP Medical Ltd, 2014.

[10] S. Charles, J. Calzada, and B. Wood, *Vitreous Microsurgery*. Lippincott Williams & Wilkins, 2010.

[11] Awh, C. C., "Why (and When) I Prefer 25-g Vitrectomy," *Retinal Physician*, 2008.

[12] B. Diniz, R. M. Ribeiro, R. B. Fernandes, J.-C. Lue, A. G. Teixeira, M. Maia, and M. S. Humayun, "Fluidics in a dual pneumatic ultra high-speed vitreous cutter system," *Ophthalmologica*, vol. 229, no. 1, pp. 15–20, 2013.

[13] S. Y. Fang, C. M. DeBoer, and M. S. Humayun, "Performance analysis of new-generation vitreous cutters," *Graefe's Archive for Clinical and Experimental Ophthalmology*, vol. 246, no. 1, pp. 61–67, 2008.

[14] T. Juan, J.-P. Hubschman, and J. D. Eldredge, "A computational study of the flow through a vitreous cutter," *Journal of biomechanical engineering*, vol. 132, no. 12, 2010.

[15] X. Su, Y. Yang, D. Xiao, and Y. Chen, "Processability investigatation of non-assembly mechanisms for powder bed fusion process," *The International Journal of Advanced Manufacturing Technology*, vol. 64, no. 5-8, pp. 1193–1200, 2013.

[16] C. L. Treviño, J. D. Galloway, and P. A. Bhounsule, "A three-dimensional printed, nonassembly, passive dynamic walking toy: design and analysis," *Journal of Mechanisms and Robotics*, vol. 10, no. 6, 2018.

[17] J. S. Cuellar, G. Smit, A. A. Zadpoor, and P. Breedveld, "Ten guidelines for the design of non-assembly mechanisms: The case of 3d-printed prosthetic hands," *Proceedings of the Institution of Mechanical Engineers, Part H: Journal of Engineering in Medicine*, vol. 232, no. 9, pp. 962–971, 2018.

[18] J. S. Cuellar, G. Smit, D. Plettenburg, and A. Zadpoor, "Additive manufacturing of non-assembly mechanisms," *Additive Manufacturing*, vol. 21, pp. 150–158, 2018.

[19] Varotis, A. B. (2020) Selecting the right 3d printing process. Accessed: 20 March 2020. [Online]. Available: https://www.3dhubs.com/knowledge-base/selecting-right-3d-printing-process/by-capabilities

[20] T. S. Hassan, "Advances in vitreous cutters," *Retina Today*, pp. 108–10, 2014.

[21] Dutch Opthalmic Research Center (D.O.R.C). Disposable pneumatic vitrectome. (27 gauge / 0.4 mm) (working with 42 p.s.i., max. 6000 cuts/min. Accessed on: 30 October 2019. [Online]. Available: https://www.dorc.eu/product/disposable-pneumatic-vitrectome-%27-gauge-%04-mm-working-%42-psi-max-%6000-cutsmin

[22] "Pushing the envelope in small-gauge surgery: The impact of 2-dimensional cutter technology," *Retinal Physician*, vol. 14, no. 12, pp. 6–8, 2017.

[23] D. E. Higgins and J. C. Easley, "Vitrectomy cutting mechanism," U.S. Patent US4 696 298 (A), September 29, 1987.

[24] C. Sawicz, "Vitreous cutter pneumatic driver," U.S. Patent US2 019 183 679 (A1), June 20, 2019.

[25] T. Akkas and T. Carlson, "Surgical cutting instrument," U.S. Patent US4 909 249 (A), March 20, 1990.

[26] ——, "Surgical cutting instrument with reciprocating inner cutter," U.S. Patent US4 986 827 (A), January 22, 1991.

[27] E. De Juan, G. S. Gahn, J. J. Weidenbenner, and D. Hickingbotham, "Vitrectomy probe," U.S. Patent US5 047 008 (A), September 10, 1991.

[28] ——, "Pneumatic vitreotome," U.S. Patent US2 009 281 479 (A1); US8 784 432 (B2), November 12, 2009.

[29] S. T. Charles, "Surgical apparatus for a vitreous," U.S. Patent US2 009 082 715 (A1); US8 080 029 (B2), March 26, 2009.

[30] B. W. Mcdonell, "Reduced friction vitrectomy probe," U.S. Patent US2 012 158 006 (A1); US9 101 442 (B2), June 21, 2012.

[31] J. R. Underwood, J. R. Aulid, and J. C. Huculak, "Vitrectomy probe with adjustable cutter port size," U.S. Patent US2 012 158 029 (A1); US9 101 441 (B2), June 21, 2012.

[32] J. R. Auld and J. C. Huculack, "Hydraulic vitrectomy probe," U.S. Patent US2 012 165 724 (A1); US8 540 743 (B2), June 28, 2012.

[33] J. R. Underwood, J. R. Aulid, and J. C. Huculak, "Vitrectomy probe with adjustable cutter port size," U.S. Patent US2 013 158 583 (A1), June 20, 2013.

[34] B. W. Mcdonell, "Dual mode vitrectomy system," U.S. Patent US2 016 128 870 (A1); US9 974 689 (B2), May 12, 2016.

[35] N. M. Gunn, "Traction-limiting vitrectomy probe," U.S. Patent US10 111 777 (B2); US2 016 143 780 (A1), May 26, 2016.

[36] J. L. Lopez, M. D. Mccawley, B. W. Mcdonell, T. C. Ryan, J. R. Underwood, S. Valencia, and J. R. Auld, "Vitrectomy probe," U.S. Patent US2 018 360 660 (A1), December 20, 2018.

[37] B. W. Mcdonell, "Systems and methods for actuating a vitrectomy probe using a fluidic amplifier," U.S. Patent US2 019 000 672 (A1), January 3, 2019.

[38] K. Makihara, "Surgical apparatus for a vitreous," U.S. Patent US6 383 203 (B1), May 7, 2002.

[39] B. W. Mcdonell, "Minimal pulsation ophthalmic probe," Australian Patent AU2 017 203 358 (A1); AU2 017 203 358 (B2), June 8, 2017.

[40] G. L. Kirchhevel, "Microsurgical instrument," U.S. Patent US2 007 185 512 (A1); US8 187 293 (B2), August 9, 2007.

[41] ——, "Microsurgical instrument," U.S. Patent US2 007 185 514 (A1), August 9, 2007.

[42] J. Dean, N. M. Gunn, and A. D. Johnson, "Reciprocating surgical tool with inertial damper," U.S. Patent US2 018 243 134 (A1), August 30, 2018.

[43] J. R. Auld and J. C. Huculak, "Method of operating a vitrectomy probe," U.S. Patent US2 010 312 169 (A1), December 9, 2010.

[44] B. Missilian, T. Akkas, and W. Cook, "Cutting assembly for surgical cutting instrument," U.S. Patent US5 019 035 (A), May 28, 1991.

[45] L. Egi, "Ophthalmic surgical device handle and associated devices, systems, and methods," U.S. Patent US10 045 883 (B2); US2 016 324 688 (A1), November 10, 2016.

[46] M. A. Helfgott and G. N. Helfgott, "Ophthalmic surgical instrument with beveled tip," U.S. Patent US4 530 356(A), July 23, 1985.

[47] M. Martinez, "Surgical instrument for ophthalmic surgery," U.S. Patent US4 577 629 (A), March 25, 1986.

[48] ——, "Surgical instrument having a offset probe for ophthalmic surgery," U.S. Patent US4 753 234 (A), June 28, 1988.

[49] K. W. Wright, "Precision intra ocular apparatus," U.S. Patent US4 662 869 (A), May 5, 1987.

[50] S. T. Charles, "Systems and methods for pressure driven tool actuation," U.S. Patent US2 018 193 192 (A1), July 12, 2018.

[51] D. J. Kopf, "Ophthalmic instrument," U.S. Patent US3 994 297 (A), November 30, 1976.

[52] M. A. Helfgott and G. N. Helfgott, "Powered handpiece for endophthalmic surgery," U.S. Patent US4 314 560 (A), February 9, 1982.

[53] P. J. Petillo, "Apparatus for microsurgery," U.S. Patent US4 940 468 (A), July 10, 1990.

[54] L. J. Cull, "Turbine driven vitrectomy cutter," U.S. Patent US2 003 114 870 (A1) US6 875 221 (B2), June 19, 2003.

[55] G. Sussman and T. G. Capetan, "Surgical handpiece," U.S. Patent US6 004 284 (A), December 21, 1999.

[56] S. T. Charles, "Vitrectomy probe with rotary cutter and associated devices, systems and methods," U.S. Patent US2 018 008 463 (A1), January 11, 2018.

[57] S. T. Charles, H. J. Tyler, and D. M. Domash, "Vitreous cutter," U.S. Patent US5 176 628 (A), January 5, 1993.

[58] M. J. Papac, M. J. Yadlowsky, and J. C. Huculak, "Pneumatically driven ophthalmic scanning endoprobe," U.S. Patent US2 012 245 569 (A1); US9 192 515 (B2), September 27, 2012.

[59] P. Bennett and S. Goh Toh, "End cutting vitrectomy probe," U.S. Patent WO2 009 079 229 (A2); WO2 009 079 229 (A3), June 25, 2009.

[60] R. S. Dotson, "Ophthalmic handpiece with pneumatically operated cutter," U.S. Patent US4 316 465 (A), February 23, 1982.

[61] M. Farley, "Vitrectomy probe with a counterbalanced electromagnetic drive," U.S. Patent US10 251 782 (B2); US2 016 120 697 (A1), May 5, 2016.

[62] T. Hunter, "Method for using microelectromechanical systems to generate movement," Spain Patent EP3 146 946 (A1), March 29, 2017.

[63] J. Y. Chon, "Dual electromagnetic coil vitrectomy probe," U.S. Patent US2 015 157 503 (A1); US9 486 360 (B2), June 11, 2015.

[64] G. N. Peyman, "Ophthalmic instrument," U.S. Patent US3 776 238 (A), December 4, 1973.

[65] S. G. Strayer and L. Hickey, "Electrical guillotine vitrectomy cutter," U.S. Patent US2 019 099 292 (A1), April 4, 2019.

[66] L. T. Ying-Ching, F. Tao, and T. Escorcio, "Microsurgical cutting device," Patent WO9 305 719 (A1), April 1, 1993.

[67] J. R. Underwood, "Electronically actuated reciprocating surgical instrument," U.S. Patent US2 018 369 016 (A1), December 27, 2018.

[68] T. Y. Lo, F. Tao, T. Escorcio, and K. H. Packo, "Intraocular surgical scissors," U.S. Patent US5 275 607 (A), January 4, 1994.

[69] S. T. Charles, "Variable drive vitrectomy cutter," U.S. Patent US2 011 295 296 (A1); US8 298 253 (B2), December 1, 2011.

[70] R. Ross, G. Hughes, J. C. Boore, and T. E. Reimer, "Apparatus and method for performing ophthalmic procedures," U.S. Patent US2 004 049 217 (A1), March 11, 2004.

[71] R. Ross, G. Hughes, and J. C. Boore, "An apparatus and method for performing ophthalmic procedures," Patent WO9 746 164 (A1), December 11, 1997.

[72] ——, "Apparatus for performing ophthalmic procedures," U.S. Patent US5 833 643 (A), November 10, 1998.

[73] R. Ross, G. Hughes, J. C. Boore, and T. E. Reimer, "An apparatus and method for performing ophthalmic procedures," U.S. Patent WO0 078 371 (A1), December 28, 2000.

[74] A. Barnes, C. De Boer, and M. Mccormick, "Disposable vitrectomy handpiece," U.S. Patent US2 017 319 387 (A1), November 9, 2017.

[75] unknown, "Eye vitreous infusion cutter," Australian Patent AU3 250 178 (A), July 26, 1979.

[76] R. M. Hartman and A. F. Trott, "Reciprocation vitreous suction cutter head," U.S. Patent US4 108 182 (A), August 22, 1978.

[77] M. Martinez, "Surgical cutting instrument," U.S. Patent US4 246 902 (A), January 27, 1981.

[78] W. C. Lawson, J. V. Paganelli, and P. Sepielli, "Ocular cutter with enhanced cutting action," U.S. Patent US5 059 204 (A), Oktober 22, 1991.

[79] J. Zacharias, "Spring mass surgical system," Patent WO2 007 062 412 (A2); WO2 007 062 412 (A3), May 31, 2007.

[80] ——, "Precision surgical system," Patent WO2 007 056 763 (A2); WO2 007 056 763 (A3), May 18, 2007.

[81] J. Attinger, W. Maag, and L. Egi, "Device for use in ophthalmic procedures," U.S. Patent US6 527 736 (B1), March 4, 2003.

[82] A. Banko, "Surgical instrument with flexible blade," U.S. Patent US4 210 146 (A), July 1, 1980.

[83] D. L. Oberkamp and B. J. Barwick, "Hard drive vitrectomy probe," U.S. Patent US6 485 499 (B1), November 26, 2002.

[84] H. T. Dinkelkamp and N. G. Douvas, "Fixed arc cyclic ophthalmic surgical instrument," U.S. Patent US4 200 106 (A), April 29, 1980.

[85] R. Machemer, D. Hickingbotham, and B. Dodge, "Oscillatory coupling for surgical instruments and methods of imparting oscillatory motion thereto," U.S. Patent US5 609 602 (A), March 11, 1997.

[86] D. E. Staub, C. L. Foltz, and R. W. Simmons, "Vitreous cutter," U.S. Patent US4 014 342 (A), March 29, 1977.

[87] A. Banko, "Rotatable surgical instrument," U.S. Patent US3 945 375 (A), March 23, 1976.

[88] ——, "Surgical cutting instrument with release mechanism," U.S. Patent US4 436 091 (A), March 13, 1984.

[89] C. A. Toth, R. F. Overaker, B. C. Dodge, and R. Machemer, "Magnetic couplings for imparting simultaneous rotary and longitudinal oscillations," U.S. Patent US6 478 681 (B1), November 12, 2002.

[90] ——, "Hand-held surgical instruments employing magnetic couplings for simultaneous rotary and longitudinal oscillations of distal workpieces," U.S. Patent US6 517 560 (B1), February 11, 2003.

[91] B. C. Dodge and R. F. Overaker, "Power supplies for drive assemblies which minimize net torque and/or vibration thereof," Patent WO0 243 225 (A1), 2002.

[92] D. G. Wuchinich, "Endoscopic ultrasonic rotary electro-cauterizing aspirator," U.S. Patent US5 176 677 (A), January 5, 1993.

[93] V. A. Dumenek, G. E. Stolyarenko, and L. V. Kossovsky, "Ophthalmological device," U.S. Patent US5 024 652 (A), June 18, 1991.

[94] ——, "Ophthalmological device," Great Brittain Patent GB2 222 952 (A), March 28, 1990.

[95] A. Banko, "Surgical-type method for removing material," U.S. Patent US3 996 935 (A), December 14, 1976.

[96] J. O'Donnell, M. Kim, and H.-S. Yoon, "A Review on Electromechanical Devices Fabricated by Additive Manufacturing," *Journal of Manufacturing Science and Engineering*, vol. 139, no. 1, 08 2016, 010801. [Online]. Available: https://doi.org/10.1115/1.4033758

[97] L. Li, A. Tirado, I. Nlebedim, O. Rios, B. Post, V. Kunc, R. Lowden, E. Lara-Curzio, R. Fredette, J. Ormerod *et al.*, "Big area additive manufacturing of high performance bonded ndfeb magnets," *Scientific reports*, vol. 6, p. 36212, 2016.

[98] Z. Chen, X. Song, L. Lei, X. Chen, C. Fei, C. T. Chiu, X. Qian, T. Ma, Y. Yang, K. Shung *et al.*, "3d printing of piezoelectric element for energy focusing and ultrasonic sensing," *Nano Energy*, vol. 27, pp. 78–86, 2016.

[99] ASTM Committee F42 on Additive Manufacturing Technologies, *Standard terminology for additive manufacturing technologies*. Astm International, 2012.

[100] K. Salonitis, "Design for additive manufacturing based on the axiomatic design method," *The International Journal of Advanced Manufacturing Technology*, vol. 87, no. 1-4, pp. 989–996, 2016.

[101] J. Vanek, J. A. G. Galicia, and B. Benes, "Clever support: Efficient support structure generation for digital fabrication," in *Computer graphics forum*, vol. 33, no. 5. Wiley Online Library, 2014, pp. 117–125.

[102] R. Hague, S. Mansour, N. Saleh, and R. Harris, "Materials analysis of stereolithography resins for use in rapid manufacturing," *Journal of materials science*, vol. 39, no. 7, pp. 2457–2464, 2004.

[103] I. L. Krivts and G. V. Krejnin, *Pneumatic actuating systems for automatic equipment: structure and design*. Crc Press, 2006.

[104] M. De Volder and D. Reynaerts, "Pneumatic and hydraulic microactuators: a review," *Journal of Micromechanics and microengineering*, vol. 20, no. 4, p. 043001, 2010.

[105] J. Krause and P. Bhounsule, "A 3d printed linear pneumatic actuator for position, force and impedance control," in *Actuators*, vol. 7, no. 2. Multidisciplinary Digital Publishing Institute, 2018, p. 24.

[106] W. Zhao, A. Song, and Y. Cao, "An extended proxy-based sliding mode control of pneumatic muscle actuators," *Applied Sciences*, vol. 9, no. 8, p. 1571, Apr 2019. [Online]. Available: http://dx.doi.org/10.3390/app9081571

[107] M. Schaffner, J. A. Faber, L. Pianegonda, P. A. Rühs, F. Coulter, and A. R. Studart, "3d printing of robotic soft actuators with programmable bioinspired architectures," *Nature communications*, vol. 9, no. 1, pp. 1–9, 2018.

[108] R. Mutlu, C. Tawk, G. Alici, and E. Sariyildiz, "A 3d printed monolithic soft gripper with adjustable stiffness," in *IECON 2017-43rd Annual Conference of the IEEE Industrial Electronics Society*. IEEE, 2017, pp. 6235–6240.

[109] C. Tawk, G. M. Spinks, M. in het Panhuis, and G. Alici, "3d printable vacuum-powered soft linear actuators," in *2019 IEEE/ASME International Conference on Advanced Intelligent Mechatronics (AIM)*. IEEE, 2019, pp. 50–55.

[110] M. E. Salem, Q. Wang, R. Wen, and M. Xiang, "Design and characterization of soft pneumatic actuator for universal robot gripper," in *2018 International Conference on Control and Robots (ICCR)*. IEEE, 2018, pp. 6–10.

[111] H. K. Yap, H. Y. Ng, and C.-H. Yeow, "High-force soft printable pneumatics for soft robotic applications," *Soft Robotics*, vol. 3, no. 3, pp. 144–158, 2016.

[112] W. Hu, W. Li, and G. Alici, "3d printed helical soft pneumatic actuators," in *2018 IEEE/ASME International Conference on Advanced Intelligent Mechatronics (AIM)*. IEEE, 2018, pp. 950–955.

[113] B. Sparrman, S. Kernizan, J. Laucks, S. Tibbits, and C. Guberan, "Liquid printed pneumatics," in *ACM SIGGRAPH 2019 Emerging Technologies*, 2019, pp. 1–2.

[114] B. N. Peele, T. J. Wallin, H. Zhao, and R. F. Shepherd, "3d printing antagonistic systems of artificial muscle using projection stereolithography," *Bioinspiration & biomimetics*, vol. 10, no. 5, p. 055003, 2015.

[115] D. B. Comber, J. E. Slightam, V. R. Gervasi, J. S. Neimat, and E. J. Barth, "Design, additive manufacture, and control of a pneumatic mr-compatible needle driver," *IEEE Transactions on Robotics*, vol. 32, no. 1, pp. 138–149, 2016.

[116] F. Schmitt, O. Piccin, L. Barbé, and B. Bayle, "An origami-inspired flexible pneumatic actuator," in *2018 IEEE/RSJ International Conference on Intelligent Robots and Systems (IROS)*. IEEE, 2018, pp. 436–441.

[117] R. MacCurdy, R. Katzschmann, Y. Kim, and D. Rus, "Printable hydraulics: A method for fabricating robots by 3d co-printing solids and liquids," in *2016 IEEE International Conference on Robotics and Automation (ICRA)*. IEEE, 2016, pp. 3878–3885.

[118] H. F. Lau, "3d-printed inflatable actuators. design and development of soft actuators for a pneumatically-actuated soft robotic arm," Zurich, 2019-08.

[119] B. Sparrman, S. Darbari, R. Rustom, M. Hughes, S. Kernizan, J. Laucks, and S. Tibbits. (2020) Liquid printed pneumatics. Accessed: 31 March 2020. [Online]. Available: https://selfassemblylab.mit.edu/liquid-printed-pneumatics/lfrglxnmf98luraefa009vmf9tmi3x

[120] M. Vázquez, E. Brockmeyer, R. Desai, C. Harrison, and S. E. Hudson, "3d printing pneumatic device controls with variable activation force capabilities," in *Proceedings of the 33rd Annual ACM Conference on Human Factors in Computing Systems*, 2015, pp. 1295–1304.

[121] P. King and J. Covington, "A novel monolithic microactuator fabricated by 3d rapid direct manufacture," *Procedia Chemistry*, vol. 1, no. 1, pp. 1163–1166, 2009.

[122] A. P. Taylor and L. F. Velásquez-García, "Miniaturized diaphragm vacuum pump by multi-material additive manufacturing," *Journal of Microelectromechanical Systems*, vol. 26, no. 6, pp. 1316–1326, 2017.

[123] A. Teixeira, L. P. Chong, N. Matsuoka, L. Arana, R. Kerns, P. Bhadri, and M. Humayun, "Vitreoretinal traction created by conventional cutters during vitrectomy," *Ophthalmology*, vol. 117, no. 7, pp. 1387–1392, 2010.

[124] M. Di Giovanni, *Flat and corrugated diaphragm design handbook*. Marcel Dekker, INC, 1982.

[125] Stratasys, "Tango polyjet simulated rubber material data sheet," 2018.

[126] D. Li, L. Dong, and R. S. Lakes, "A unit cell structure with tunable poisson's ratio from positive to negative," *Materials Letters*, vol. 164, pp. 456–459, 2016.

[127] Stratasys, "Agilus30 polyjet rubber-like material data sheet," 2017.

[128] D. A. Howells and H. Arora, "Technical note - preliminary mechanical testing of agilus support samples," N.D., unpublished.

[129] Stratasys, "Vero material data sheet," 2018.

[130] Williams, C. (2020) Polyjet accuracy: Matte vs. glossy. Accessed: 29 July 2020. [Online]. Available: https://www.cati.com/blog/2020/01/polyjet-accuracy-matte-vs-glossy/

[131] Nahum, A. (2019) Matte or glossy? which finish to use for your 3d prints and when. Accessed: 29 July 2020. [Online]. Available: https://grabcad.com/tutorials/matte-or-glossy-which-finish-to-use-for-your-3d-prints-and-when

[132] L. J. Stiltner, A. M. Elliott, and C. B. Williams, "A method for creating actuated joints via fiber embedding in a polyjet 3d printing process," in *22nd annual international solid freeform fabrication symposium*, 2011, pp. 583–592.

[133] S. T. Charles, "Hydraulic acuation for microsurgical instruments," U.S. Patent US2 009 030 436 (A1), January 29, 2009.

10. Appendix A

This appendix contains the descriptions corresponding to the driving mechanisms of vitreous cutters that were found in the patent literature.

10.1. Translating cutters

The following section describes the largest group of instruments, those that utilize a translating cutter motion. The means to drive the translating cutters are extensive, however, most translating cutters are driven by a diaphragm that moves in response to air pressure pulses from a control system.

10.1.1. Fluidic

The following section contains the patents that describe mechanisms to drive a translating cutter, and use a fluidic engine to power the mechanism.

Diaphragm

Patents [23]–[44] all describe a mechanism that uses a diaphragm to drive a translating reciprocating cutter. The construction of these instruments is relatively simple, since the mechanism requires few moving parts. A diaphragm is placed inside the handle of the instrument, and depending on the presence of a biasing spring, is connected to one or two air chambers. A schematic drawing of a double actuated mechanism is shown in figure 52 and a schematic drawing of a biased mechanism is shown in figure 53. The air chamber(s) is/are connected to an external pressure source that supplies short pulses of pressurized air. In response, the diaphragm (red) will move due to these pressure pulses. In a biased system, only one air-chamber is present and a spring (pink) will push the diaphragm (red) back in its original position. Dual actuated mechanisms have two air-chambers (orange & brown) and use a second pressure pulse supplied to the opposite side of the diaphragm to achieve this. The inner cutter (blue) is inserted through the centre of the diaphragm and secured to it. Therefore, the inner cutter moves forward and backward along with the movement of the diaphragm. Because the cutter extends past the diaphragm, it is easy to connect the instrument to an external vacuum source. The mentioned cut rates for diaphragm mechanisms vary between 1 and 50,000 cuts per minute [32], [34].

Piston actuator

Another type of fluidic actuator that is used to generate a translating movement to drive the cutter is the piston actuator. Patents [45]–[53] all describe such a mechanism. A schematic drawing of a vitreous cutter using a piston mechanism is shown in figure 54. The working principle is similar to that of a diaphragm, although, the range of motion can be larger than that of a diaphragm mechanism. There is an internal chamber in the handle of the instrument in which a piston (red) is able to slide back and forth. The piston is sealed to the walls of the chamber using o-ring seals to prevent air leakage. Because the mechanism is

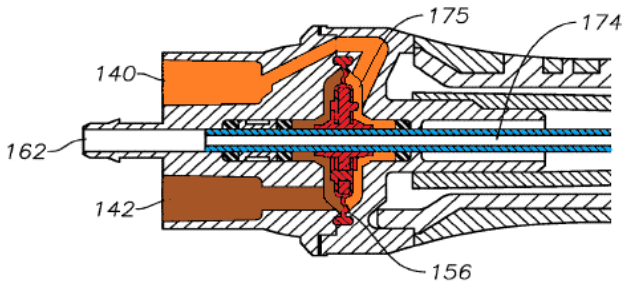

Figure 52. Schematic representation of a dual-actuated diaphragm mechanism. Components: 140 = Pressurized air inlet 1, 142 = Pressurized air inlet 2, 156 = diaphragm, 162 = vacuum connector, 174 = inner cutting tube, 175 = rear air-chamber. Adapted from: [24]

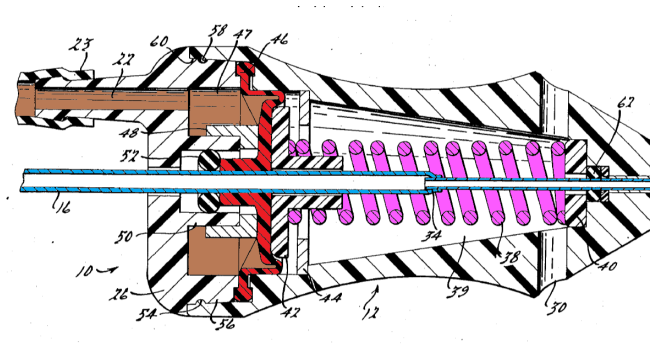

Figure 53. Schematic representation of a biased diaphragm mechanism. Important components: 16 = connection tube between diaphragm and cutter, 22 = inlet for pressurized air, 38 = Compression spring, 42 = Force distributor for spring, 46 = Diaphragm, 47 = air-chamber, 52 = rear O-ring seal, 62 = front O-ring seal. Adapted from: [23]

biased by a spring (pink), pressurized air is only supplied to one end of the piston. If the mechanism is not biased, pressurized air is supplied to both ends of the piston to create reciprocating movement. This is similar to mechanisms that utilize a diaphragm to generate motion. Like with diaphragm mechanisms, the inner cutting tube (blue), in most cases, is inserted through the centre of the piston and rigidly attached to it. This enables an easy connection to an external vacuum source to aspire the cut vitreous.

Turbine driven cam, with spring biased follower

Another interesting example is given in patent [54], the patent describes a mechanism which uses a turbine powered by continuous air pressure to drive a reciprocating translating cutter. A schematic drawing of the proposed mechanism is shown in figure 55. The turbine (red) is positioned inside an air-chamber to which an air-inlet and exhaust are connected. Pressurized air flows into the air chamber and hits the turbine blades, in response they rotate. The air subsequently exits the air-chamber through the exhaust. The turbine rotates a drive shaft , to which a cam (green) is attached. This cam interacts with a follower (purple), situated below the turbine at the bottom of the air-chamber.

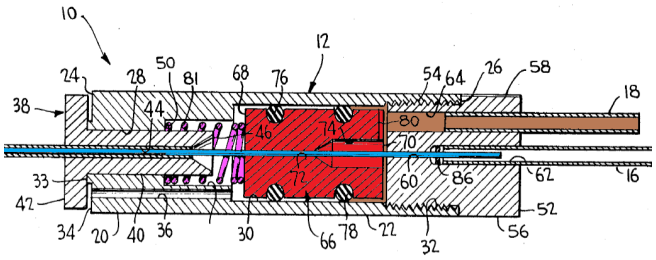

Figure 54. Schematic drawing of a piston based mechanism. Relevant components: 16 = vacuum supply tube, 18 = pressurized air supply tube, 44 = inner cutting tube, 76 = distal O-ring, 78 = proximal O-ring, 81 = compression spring, Adapted from: [47]

A compression spring (pink) is positioned between the follower and housing of the instrument, to bias the follower. This ensures that the follower remains in contact with the cam for the entire duration of the cutting cycle. The inner cutting tube (blue) is rigidly attached to the follower and therefore, moves with it. The geometry of the cam is such that the cutting port in the outer shaft is opened and closed as the cam is rotated. The main benefit of the mechanism is, that the air supply is continuous during the entire cutting cycle. The cutting speed is therefore, not dependent on a valve system that supplies air pressure pulses to the system to actuate the cutter, as is the case with many diaphragm based mechanisms. Also a higher force can be generated due to the fact that the surface area that is in contact with the pressurized air is much larger, than in a diaphragm based system. This has the consequence that a more reliable spring with higher stiffness can be used to bias the follower. The maximum cut rate depends on the stiffness of the spring, and the maximum air pressure that is available to actuate the system. No exact cutting speed is mentioned by the authors however, they argue that it can be much higher than that of conventional instruments because of the continuous air supply.

Fluidic amplifier

Patent [37] describes a special form of a diaphragm mechanism. A standard diaphragm is equipped with a fluidic amplifier to direct the airflow to the front or rear of the diaphragm with the help of control jets. A schematic close up of such a fluidic amplifier can be seen in figure 56, in figure 57 a schematic drawing of a fluidic amplifier in relation to the entire instrument is shown. A high powered airflow is continuously supplied to the fluidic amplifier, and additional smaller controlled pulses of air are directed at the airflow to redirect it. The pressurized air can be directed to either the front, or rear air chamber of the diaphragm (red). This will subsequently cause the diaphragm to move, and to therefore, also move the attached cutter (blue). A large number of different fluidic amplifiers are described in the patent, the aforementioned description is meant to illustrate the general working principle.

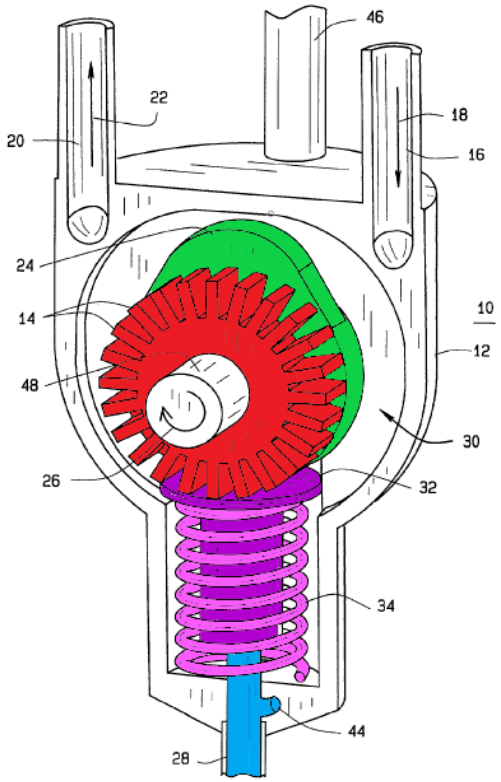

Figure 55. Schematic representation of the turbine driven cam mechanism. Important components: 14 = turbine blades, 16 = inlet of pressurized air, 18 = direction of air inflow, 20 = exhaust of air, 22 = direction of air outflow 24 = cam, 26 = direction of rotation of drive shaft, 28 = inner cutting tube, 32 = follower, 34 = compression spring, 48 = drive shaft. Adapted from: [54]

Dual diaphragm configuration to minimize vibration

Patent [42] also details an interesting variation on the standard diaphragm driving mechanism. It uses two diaphragms that move in opposite directions using the same air pulses supplied by a control system. A schematic representation of the mechanism is shown in figure 58. The right diaphragm (red) operates as is previously described in the diaphragm paragraph, and has the function of moving the inner cutting tube (blue) to cut the vitreous. The left diaphragm (red) moves in the opposite direction and has the function of counteracting the movement of the right diaphragm. This reduces the vibration generated by the instrument and could improve the stability as well as the accuracy. An internal pathway (brown & orange) couples the chambers of both diaphragms in such a way that the diaphragms move in opposite directions using the same pressure pulse. In this manner a standard control system can be used to operate the instrument, instead of a specialized system that can appropriately control both diaphragms simultaneously. It is described that both diaphragms should have approximately equal masses, but that they can vary in size. The maximum cutting rate of the instrument is mentioned to be 1,000 cycles per second, or 60,000 cuts per minute.

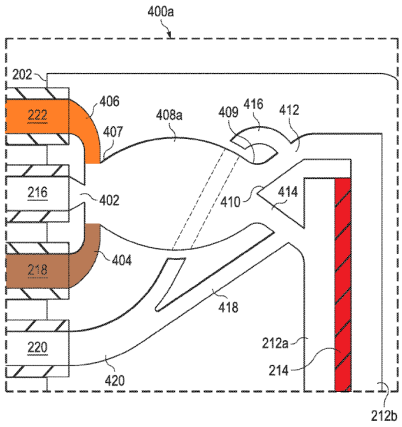

Figure 56. Schematic representation of a fluidic amplifier mechanism. Relevant components: 212(a) = Front air chamber, 212(b) = rear air chamber, 214 = diaphragm, 216 = Continuous air pressure inlet, 218 = control jet 1 inlet, 222 = control jet 2 inlet, 220 = air exhaust, 410 = air divider Adapted from: [37]

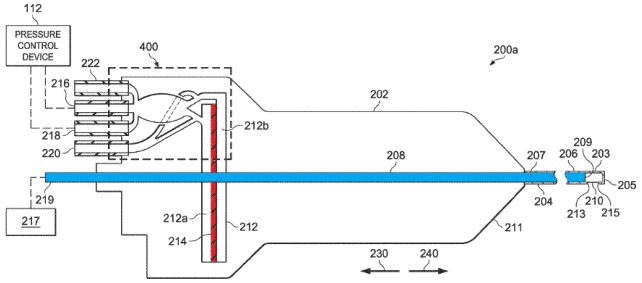

Figure 57. Schematic representation of a fluidic amplifier mechanism in relation to the complete instrument. Relevant components: 204 = outer tube, 208 = inner cutting tube, 210 = cutting port, 212(a) = Front air chamber, 212(b) = rear air chamber, 214 = diaphragm, 216 = Continuous air pressure inlet, 218 = control jet 1 inlet, 222 = control jet 2 inlet, 220 = air exhaust, 410 = air divider. Adapted from: [37]

Boiling of conductive liquid

Patent [55] describes a mechanism that uses the boiling of a conductive liquid to drive the inner cutter of a vitreous removal instrument. A schematic drawing of the described mechanism is shown in figure 59. The mechanism consists of a piston (red) with at the proximal end a boiling chamber (brown). The liquid is supplied to the chamber through an electrode with an integrated valve system to prevent back-flow. O-ring seals in the piston, and at the proximal side of the boiling chamber seal the chamber. The proximal face of the piston contains an electrode, the distal face is connected to the cutter (blue), and also interfaces with a return spring (pink) to bias the mechanism. The mechanism operates as follows: Liquid is supplied to the boiling chamber through the valve system. When enough liquid has accumulated, a current is applied to both the electrode at the proximal end of the boiling chamber and to the one attached to the piston. The current will heat the liquid, causing it to boil, and to transform it into gas. This process is accompanied with

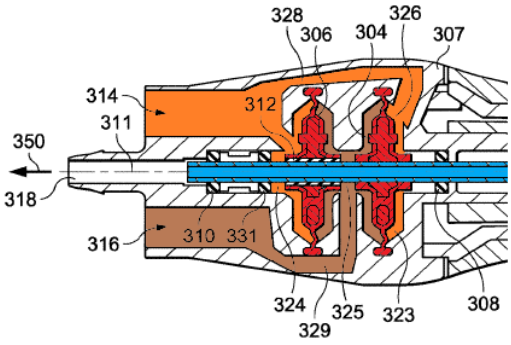

Figure 58. Schematic representation of the dual diaphragm mechanism. Relevant components: 304 = movement generating diaphragm, 306 = counterbalancing diaphragm, (308 & 310 & 331) = O-ring seal, 311 = vacuum connector, 312 = Low friction sealing bearing, 314 = Pressure pulse receiver inducing backward motion of cutter, 316 = Pressure pulse receiver inducing forward motion of cutter, Cutter is highlighted in orange. Adapted from: [42]

a large expansion in volume, which overcomes the spring force and pushes the piston forward. The excess gas escapes through the exhaust, lowering the pressure, and returning the piston to its initial position. The cycle is repeated to generate a reciprocating motion of the cutter.

An alternative embodiment described in the patent uses two boiling chambers to actuate the piston instead of one chamber and a return spring. One boiling chamber is placed in front of the piston in a similar manner as previously described, the second boiling chamber is placed behind the piston. Additional electrodes are placed at the rear end of the second chamber and on the rear face of the piston. The piston is moved by intermittently supplying power to either one of the boiling chambers, causing the piston to reciprocate back and forth.

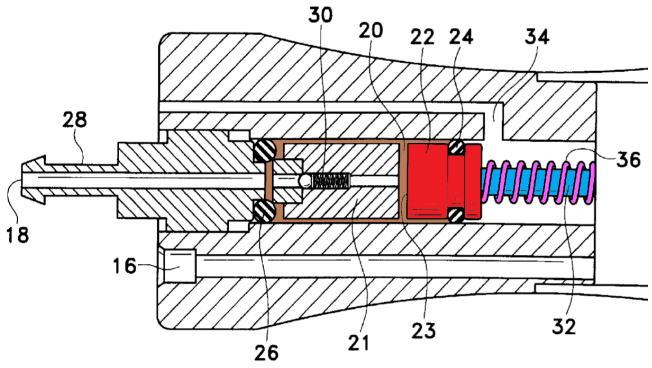

Figure 59. Schematic drawing of a mechanism that uses the boiling of liquid to drive a translating cutter. Relevant components: 16 = vacuum line, 18 = conductive liquid supply, 28 connector to conductive liquid source, 20 = boiling chamber, 22 = piston, 23 = electrode mounted on proximal face of piston, 24 & 26 = O-ring seal, 32 = cutter, 34 = air vent, 36 = compression spring. Adapted from: [55]

10.1.2. Electromagnetic

Besides the aforementioned pressure based driving mechanisms, electromagnetic driving mechanisms are also used to generate a translating movement of the cutter. The following section contains the patents that describe mechanisms to drive a translating cutter, and use an electromagnetic power source to drive the mechanism.

Solenoid actuator

Patents [53], [61]–[68] all describe mechanisms that utilize a permanent magnet in combination with a spool that is energized to generate motion. A schematic drawing of an exemplary mechanism utilizing a two magnet counterbalancing system is shown in figure 60. Patent [61] describes this particularly interesting mechanism where a set of two magnets of equal mass are used as well as two spools. The spools are mounted at the front and at the back of the instrument handle, one of the magnets (red) is rigidly connected to the inner cutting tube (blue) and will generate the motion of the cutter. The other magnet is mounted in such a way that the polarity is opposite of the magnet that is mounted to the cutter. This will cause both magnets to move in the opposite direction when a voltage is applied to the spools. The function of the second magnet is to reduce vibrations of the instrument by counterbalancing the movement of the magnet (red) attached to the cutter (blue). In this particular example, the counterbalancing magnet has a large central hole that allows it to move over the movement generating magnet and attached cutter. Other similar mechanisms have only one magnet that is attracted to a single spool, when a voltage is applied to said spool. A spring could be present to provide movement in the opposite direction when the power to the spool is cut off. The polarity of the spool could also be switched to generate motion in the opposite direction. Stops may be included to limit the movement of the magnet and/or inner cutting tube. The mentioned cut rate for solenoid mechanisms lies between 1,200 and 60,000 cuts per minute according to [66].

Wobble drive

The mechanisms in patents [69]–[75] all describe the use of a driven wobble or cam plate. A schematic drawing of a double profiled wobble drive mechanism is shown in figure 61. A rotary (electric) motor drives a shaft (green) to which a wobble plate (green) is connected. A follower assembly (purple) is situated around the plate (green), that moves back and forth in response to the rotation of the plate (green). The inner cutting tube (blue) is rigidly mounted to the follower (purple), which results in the linked movement of both components. The construction of the plate is such that it generates a back and forth movement of the follower of the appropriate size to open and close the cutting port located in the outer tube of the instrument. Furthermore, the plate could have a shape such that the port would be opened and closed multiple times if the plate is rotated only once. This could be used to increase the cut-rate of the instrument relative to the engine speed. Plates are described that are

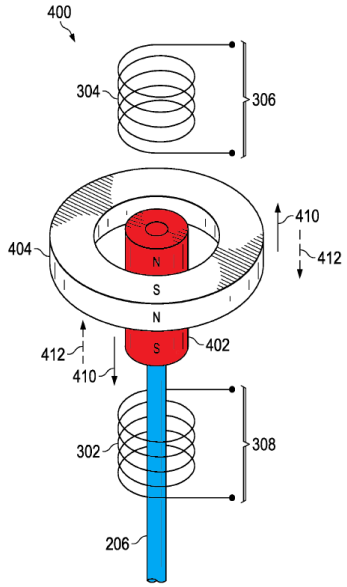

Figure 60. Schematic drawing of a counterbalancing solenoid mechanism. Relevant components: 206 = inner cutting tube, 302 = proximal coil, 304 = distal coil, 402 = movement generating magnet, 404 = counterbalancing magnet. Adapted from: [61]

profiled on both sides to remove the need for a spring to keep the follower in contact with the plate. However, single profiled plates in combination with spring biased follower assemblies are also mentioned. Patent [69] has an interesting addition to the mechanism; it describes how the plate could be constructed in a non-planar fashion (varying profile along the radius of the disk), in combination with a mechanism to move the contact point of the follower assembly relative to the radius of the disk. This allows the operator to change the duty cycle of the instrument without changing the output of the motor. It is mentioned that the cut rate could be between 600 and 6,000 cuts per minute [74]. A schematic drawing of the mechanism using a non-planar construction of the disk is shown in figure 62.

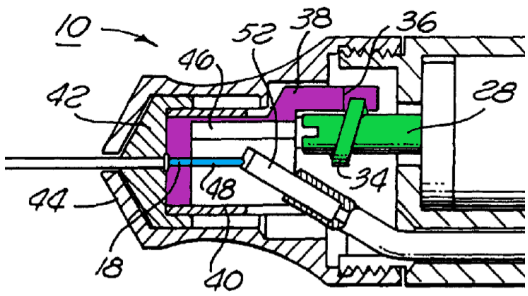

Figure 61. Schematic representation of a wobble plate mechanism that uses a follower with a fixed contact point on the wobble disk. Components: 28 = drive shaft, 34 = wobble disk, 36 = follower assembly, 48 = inner cutting tube. Adapted from: [72]

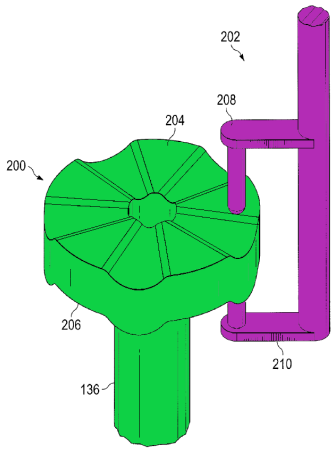

Figure 62. Schematic representation of the wobble drive mechanism that uses a movable follower. Components: 136 = drive shaft, 200 = wobble disk, 202 = follower assembly, 204 = distal cam face, 206 = proximal cam face, 208 = distal follower, 210 = proximal follower. Adapted from: [69]

Cam and spring biased follower

Patent [76] describes a mechanism to drive a reciprocating translating cutter that uses a cam. A schematic drawing of the mechanism is shown in figure 63. The mechanism consists of a hollow cam tube (green) that is continuously driven by an electric motor. The proximal end is connected to the motor and the distal end is the cam face of the tube. This cam face interfaces with a spring-loaded follower assembly (purple), to which the inner cutting tube (blue) is connected. The follower assembly is spring-loaded by means of a compression spring (pink), which is placed between the follower (purple) and a retaining ring. The spring ensures that the follower assembly remains in contact with the cam tube during the entire cutting cycle. When the cam tube is rotated by the engine, it causes the follower assembly to be reciprocated and therefore, causes the cutter to be translated. The cam surface is shaped in such a manner that the cutter has the appropriate travel to open and close the cutting port in the outer shaft. The intended cutting speed of the instrument was not mentioned in the patent; it was only stated that the cutter should reciprocate fast. Patents [77] and [78] describe similar mechanisms that also use a rotating cam shaft combined with a spring-loaded follower.

Piezoelectric actuators

Patents [79], [80] both describe mechanisms that utilize piezoelectric actuators to generate movement of the inner cutting tube. Piezoelectric actuators use piezoelectric materials to generate movement by applying a current to the material. Although the port size of a vitreous cutter is small, a single piezoelectric actuator does not have a large enough range of motion to fully open and close the cutting port. Patent [80] solves this problem by connecting multiple piezoelectric actuators in series and thereby increases the range of motion of the instrument. A different approach is described in patent [79], in which a mass spring damper system is actuated by a piezoelectric actuator. When the

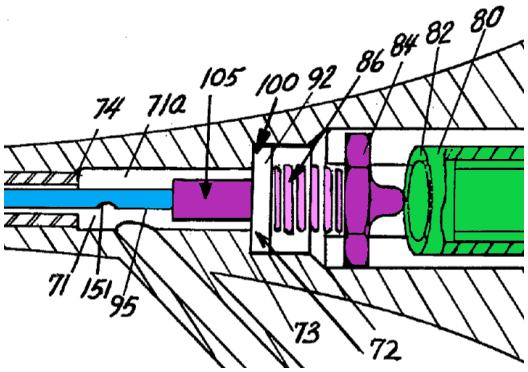

Figure 63. Schematic representation of the cam and spring biased follower mechanism. Essential components: 80 = cam-tube, 82 = cam face, 84 = follower, 86 = compression spring, 92 = retaining ring, 95 = inner cutting tube, 105 = connection of follower and cutter. Adapted from: [76]

piezoelectric actuator oscillates the mass-spring damper system at its harmonic frequency, the amplitude of the system is increased and the movement of the cutter is amplified when compared to the range of motion of the piezoelectric actuator. It is mentioned that the cut rate of piezoelectric based instruments should exceed 2,000 cuts per minute [80].

Pin + cam groove

The mechanism described in patent [81] uses the combination of a driven pin and a cam groove to actuate a reciprocating cutter. A schematic drawing of the described mechanism is shown in figure 64. Attached to the drive shaft (green) of a rotary motor, is a U-shaped bracket (green) with on one end of it a pin. This pin is perpendicularly mounted to the axis of rotation of the drive shaft. The pin interfaces with a cam groove formed in a connection piece (purple), to which the inner cutter (blue) is rigidly mounted. The groove is located on the outer surface of the connection piece, near the proximal end. The groove is formed in such a way that as the pin rotates, the cutter is displaced back and forth by the appropriate amount to open and close the cutting port in the outer tube. An interesting property of the mechanism is that it does not require a spring to complete the cutting cycle. The formed groove has two surfaces that are in contact with the pin at all times. Because of the lack of a biasing spring, there is no limitation of the cutting speed due to the finite spring stiffness. This could result in a higher cut rate of the instrument than would be possible with a spring-biased mechanism. The instrument is intended to be powered by an electric motor that continuously rotates in a single direction. No cutting speed was mentioned in the patent, however the authors do speak of ”high cutting rates” when referring to the instrument. Patent [82] describes an almost identical mechanism. The difference being that the pin is rigidly mounted on the internal surface of the housing, and the shaft containing the cam groove is driven by the motor. The shaft is mounted to the motor in such a way that rotational movement is transferred from the motor to the shaft, but translation between the two components is

not restricted. A spring is placed between the distal end of the housing and the drive shaft to bias it. The inner cutting tube is rigidly mounted to the driven shaft containing the cam groove. As the engine rotates, it causes a reciprocating movement of the cutter.

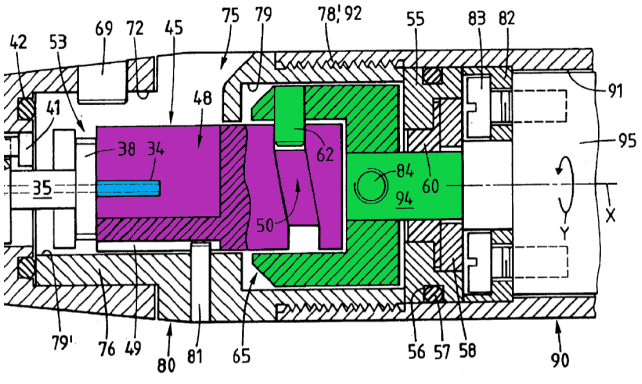

Figure 64. Schematic representation of the pin and cam groove mechanism. Relevant components: 34 = inner cutting tube, 48 = connection piece, 50 = groove formed in connection piece, 62 = pin, 65 = U-shaped bracket, 94 = driveshaft, 95 = electric motor. Adapted from: [81]

Cable pulling mechanism

Patent [83] describes a cable pulling mechanism in combination with a spring to reciprocate the cutter. The cable is attached on one end to a stepper motor, and on the other end to a ring which is mounted on the cutter. When the stepper motor is actuated, the cable will be put under tension and will retract the cutter. Attached to the other face of the ring is a tension spring to bias the instrument, and to provide the force necessary to advance the cutter. As the cutter is retracted by the pulling force of the cable, the spring will be put under tension. When the direction of the stepper motor is reversed, the tension in the cable will decrease and the spring will provide the necessary force to move the cutter forward in a controlled manner. The spring is located inside the handle of the instrument, along with the ring attached to the inner cutting tube. The stepper motor is intended to be located outside of the instrument. To prevent unintentional actuation and to prevent the cable from coming into contact with patient material, the cable has an outer sleeve around it. It is mentioned that the stepper motor should change direction slowly to prevent uncontrollable rebounding. The described actuation mechanism is designed to have a cut rate between 1 and 1,000 cuts per minute [83].

10.1.3. Manual

The patents described in this section use manual actuation to power the mechanism that drives a translating cutter.

Closed hydraulic system

Patents [93], [94] describe the use of a closed hydraulic drive system that uses manual actuation to drive a translating cutter. The system is comprised of a foot actuated pedal with an internal bellow, connected via tubing to the vitreous cutting instrument. The instrument contains a second bellow system which actuates the inner cutting tube. The bellows and the tubing that connects them are filled with an incompressible liquid. When the operator presses down on the pedal the internal bellow is compressed, and the pressure inside the tubing and bellow inside the instrument rises. As a consequence, the bellow inside the instrument expands and advances the cutter. An internal spring inside the handle of the vitreous cutter provides a biasing force to retract the cutter, as the user decreases the applied pressure on the foot pedal. Stops are placed inside the handle of the instrument to constrict the movement to the appropriate range to open and close the cutting port, which is located in the distal end of the outer tube. The intended cutting speed of the instrument is not mentioned in either of the reviewed patents. A variation on the aforementioned patents is described in [133]. The mechanism used to actuate the inner cutting tube also uses a closed hydraulic system, but does not require the user to manually deliver the pressure pulses to actuate the instrument. A control system is placed between the user and the instrument to provide hydraulic pressure pulses based on the position of a foot pedal, operated by the user.

10.2. Rotating cutters

The following section contains all the mechanisms that power a rotating cutter. Because the movement of rotating cutters can either be continuous or reciprocating, there are two groups in which the patents are subdivided.

10.2.1. Continuous

This section contains the patents that describe a continuously rotating cutter.

Fluidic

This section contains the continuously rotating cutters that are driven using a fluidic engine.

Inner and outer tube driving mechanism

Patent [58] describes various methods to continuously drive both the inner and outer tubes of the vitreous cutting instrument using a variety of different engine types and gear systems. A schematic drawing of one of the described mechanisms is shown in figure 65. A turbine (red) drives a drive shaft (green) to which a set of gears (green & purple) is attached. These gears drive both the cutter (blue) and the outer tube in opposite directions. A set of bearings is placed in between the tubes as well as the housing, to minimize friction. Pressurized air is supplied to the turbine from a control system. The patent describes the use of either one or two engines to drive the instrument. Two engines give the possibility of controlling the movement of the cutter and outer tube independently of each other. The described engine types are also varied, besides the described embodiment it is suggested that the instrument could also be driven by a piston connected to a worm gear, or by one or two electrical motors.

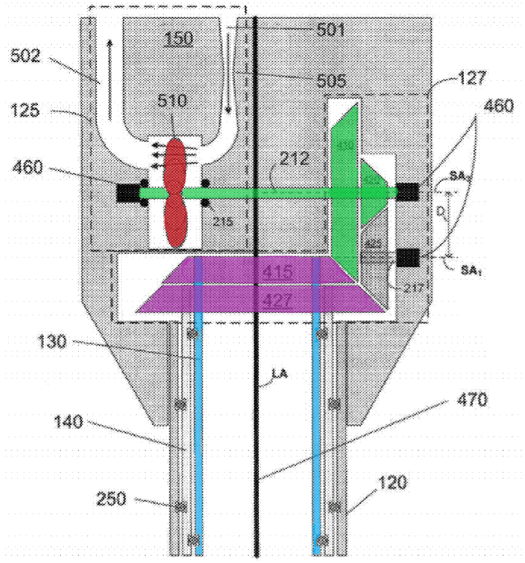

Figure 65. Schematic drawing of a mechanism to continuously drive both the cutter and the outer tube. Relevant components: 120 = housing, 130 = inner cutting tube, 140 = outer tube, 212 = drive shaft, 250 = ball bearing, 415 = angular gear driving inner cutter, 427 = angular gear driving the outer tube, 501 = pressurized air inlet, 510 = Turbine. Adapted from: [58]

Electromagnetic

This section contains the patents that describe a continuously rotating cutter which is driven by an electromagnetic engine.

Cutting blade directly driven by motor

The vitreous cutters as detailed in [86]–[88] all use an internal spring loaded, and continuously rotated cutting blade driven by a rotational motor. A schematic drawing of the vitreous cutter proposed in patent [86], is shown in figure 66. An internal spring-loaded blade (blue) cuts the partially aspired vitreous away, by means of shearing action between the blade and outer tube. The proposed motor is a rotational micro electrical motor that is powered by an internal battery. A hexagonally shaped drive shaft (green) is used to transfer the movement of the engine to the cutter. Patent [88] details the presence of a system that turns the motor briefly in the opposite direction when the device is stopped. The intention of this system is to clear the port and to prevent material being stuck in between both tubes when the instrument is moved to a different location.

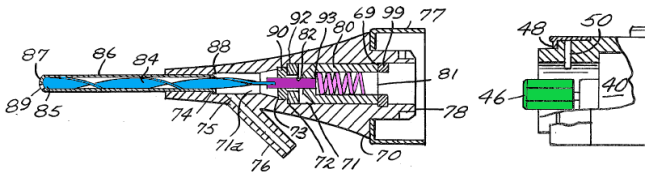

Figure 66. Schematic drawing of a mechanism to continuously drive a rotating cutter. Relevant components: 40 = motor, 46 = hexagonal drive shaft, 80 = connector between blade and drive shaft, 84 = twisted inner cutter, 86 = outer tube, 93 = compression spring. Adapted from: [86]

10.2.2. Reciprocating

The following section contains all the patents that describe reciprocating rotating cutters. The section is divided further according to the engine type that is used to drive the mechanism.

Fluidic

This section contains the patents that describe reciprocating rotating cutters that are driven by a fluidic engine.

Air-vane

Patent [56], describes a fluidic motor to actuate the inner cutting tube. A schematic drawing of this mechanism is shown in figure 67. Attached to the proximal end of the inner cutting tube (blue) are one or multiple vanes (red) that rotate inside an air chamber, located inside the instrument handle.

This air chamber can be pressurized at either side of the vane, causing a pressure difference between both sides of the vane. This results in the movement of the air-vane in the direction of the established pressure gradient. By intermittently applying pressure pulses to alternating sides of the vane, a reciprocating rotating movement of the air-vane can be achieved. The inner cutter is rigidly attached to the air-vane, and will therefore also reciprocate. The patent describes that the cut-rate of the mechanism could be increased by simultaneously applying a vacuum pulse to the non-pressurized chamber. The vacuum and pressure pulses therefore, cooperate to move the air-vane in a specific direction. The maximum cut rate of the described mechanism ranges from 10,000 - 30,000 cuts per minute, depending on the construction of the instrument.

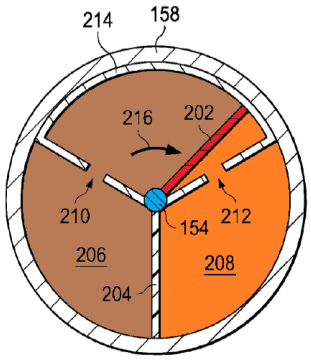

Figure 67. Schematic drawing the reciprocating air vane mechanism. Components: 154 = drive shaft connected to cutter, 158 = housing of instrument, 202 = air vane, 204 = separation wall, 206 = high pressure zone, 208 = low pressure zone, 214 = rotation chamber of air vane, 210 = air inlet 1, 212 = air inlet 2, 216 = direction of motion of air vane. Adapted from: [56]

Diaphragm and swashplate mechanism

Patent [56] describes another mechanism that achieves a reciprocal rotational movement of the cutter. This mechanism consists of a translating diaphragm that uses pressure

pulses on either side of it to create movement. A drive shaft is mounted in the centre of the diaphragm to transfer the translation movement to a mechanism, that converts it into a rotating movement of the cutter. This mechanism consists of a swashplate that is coupled to the drive shaft and a follower. The geometry and mounting of the swashplate in combination with the follower on the drive shaft causes the translating movement to transform into a rotating one. The swashplate mechanism is similar to the wobble drive mechanism, when the output and input are reversed.

Piston with integrated gear rack

In patent [57] a mechanism is described that uses a piston with an integrated gear rack, to drive a pinion gear which is attached to the inner cutting tube. A schematic close up drawing of the piston and pinion gear assembly, as well as an overview of the instrument is shown in figure 68. The piston (red) moves back and forth in response to applied air pressure pulses. Air hoses connected to an external air supply provide pressure pulses to the instrument, internal pathways provide guidance for the air to either side of the piston. The piston contains two seals, one on either end, to seal the gap between the piston and the housing. As mentioned the piston contains an integrated gear rack to transform the translating movement of the piston into a reciprocating rotating movement of the cutter (blue). When air pressure is applied to the top of the piston, it will cause a downward movement of the piston. As the piston moves down, the gear rack also moves and engages the pinion gear (purple). It will rotate the pinion gear until the piston reaches the end of the chamber, and therefore, stops moving. At this point the air pressure supply to the top side of the piston is stopped and is instead applied to the bottom side of the piston. This causes the piston to move upwards, and generates a motion opposite to the previously described one. When the piston again reaches the top of the chamber, the cutting cycle is completed.

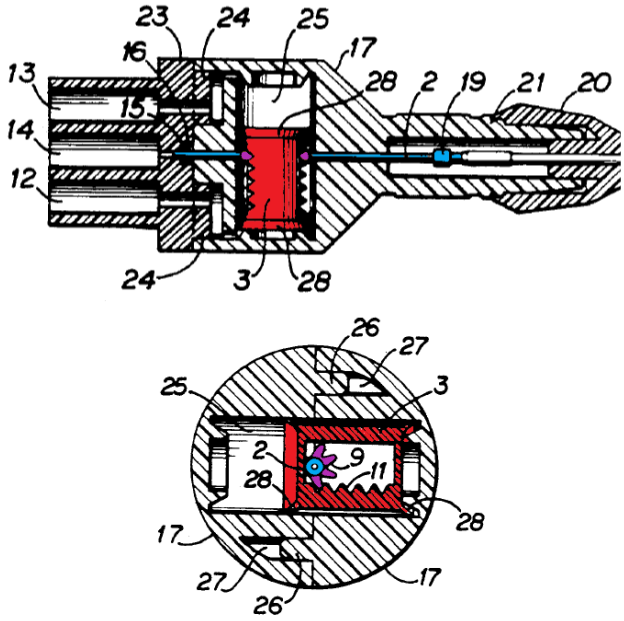

Figure 68. Schematic representation of the piston and pinion gear mechanism. Components: 2 = inner cutting tube, 3 = piston with internal gear rack, 9 = pinion gear, 11 = internal gear rack, 12,13 = connection to air pressure source, 14 = connection to vacuum source, 25 = air chamber. Adapted from: [57]

Electromagnetic

This section contains the patents that describe reciprocating rotating cutters which are driven by an electromagnetic engine.

Alternately energized electrical motor

Patent [84] describes a vitreous cutter that is driven by a rotational electric motor, which is alternately energized to reverse the direction at specific points during the cutting cycle of the instrument. A schematic drawing of the actuation mechanism of the proposed instrument is shown in figure 69. Power is intended to be applied for the duration of 100 ms and the time it takes the instrument to complete one cutting cycle is 400 ms, the cut rate of the instrument is thus, 150 cuts per minute. The rotational electric motor drives a hollow internal cutting tube (blue), which rotates inside a slightly bigger outer tube. An internal stop inside the handle in combination with an extremity extending from the collet (purple) holding the inner cutting tube, limits the relative rotation between the two concentric tubes to approximately 180 degrees.

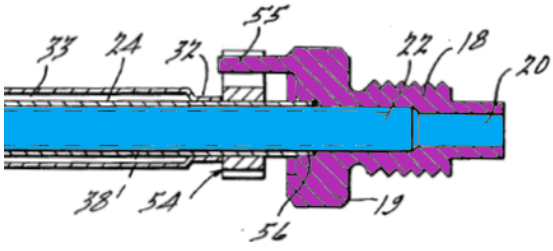

Figure 69. Schematic drawing of a mechanism that drives a reciprocating cutter. Components: 18 = collet holding the inner cutter, 20 = inner cutting tube, 32 = outer tube, 54 = stop, 55 = extremity extending from collet. Adapted from: [84]

Magnetic transmission

Patent [85] describes a magnetic transmission that drives a reciprocating rotating cutter. A schematic cross-sectional drawing of the mechanism is shown in figure 70. The mechanism consists of two shafts, which both contain a magnet holder (purple & green) at one end. These ends face each other and hold magnets (grey & yellow) that have such a polarity that they attract both magnets of the opposite holder. The right shaft (green) is continuously driven in the same direction by a motor, the left shaft (purple) is connected to the cutter. A housing is placed around both of the magnet holders, and a stabilizing rod is placed in the

centre of them. The rod has the function of keeping both magnet holders aligned, it is not driven, and does not transfer rotational movement between the two magnet holders. A pin (purple) is located on the left magnet holder, which is attached to the cutter. This pin is intended to interface with a stop located on the inside surface of the housing, and intends to limit the movement of the left magnet holder. A set of schematic drawings of the 4 steps that describe the operation of the mechanism are shown in figure 71. The mechanism operates as follows: Step 1: The motor rotates the drive shaft, both magnet holders are connected through the magnetic connection and rotate together. Step 2: Both magnet holders continue to rotate until, the pin of the left magnet holder (connected to the cutter) engages the stop in the housing. Step 3: The right shaft, driven by the motor, continues to rotate the attached magnet holder, while the stop prevents the left magnet holder (attached to the cutter) to rotate further. This results in the decoupling of the magnetic connection. Step 4: As the right magnet holder continues to be rotated, the magnets begin to attract each other again, and in response the left shaft moves in the opposite direction until the magnetic connection is re-established. A return spring could potentially be attached to the left magnet holder to assist this return movement. After the fourth step is completed, the magnetic connection between the left and right magnet holders will be reestablished and the cycle will repeat itself.

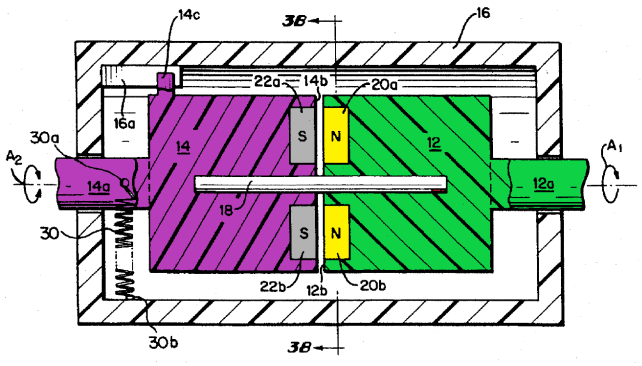

Figure 70. Schematic cross section of the magnetic transmission mechanism. Relevant Components: 12a = drive shaft extending from the motor, 12 = driving magnet holder, 14 = driven magnet holder, 14a = driven shaft connected to the cutter. 14c = pin extending from driven magnet holder, 16a = stop inside the housing, 16 = housing, 18 = stabilizing shaft, (20a & 20b)= driving magnets, (22a & 22b) = driven magnets, 30 = return spring, A1 = rotation direction of the engine, A2 = the reciprocating movement direction of the cutter. Adapted from: [85]

Manual

This section contains the patents that describe a reciprocating rotating cutter which is manually driven.

Manually rotated cutter

Patent [95] describes the construction of a vitreous removal instrument that uses manual rotation of the inner cutting tube to cut the vitreous. A schematic drawing of the instrument

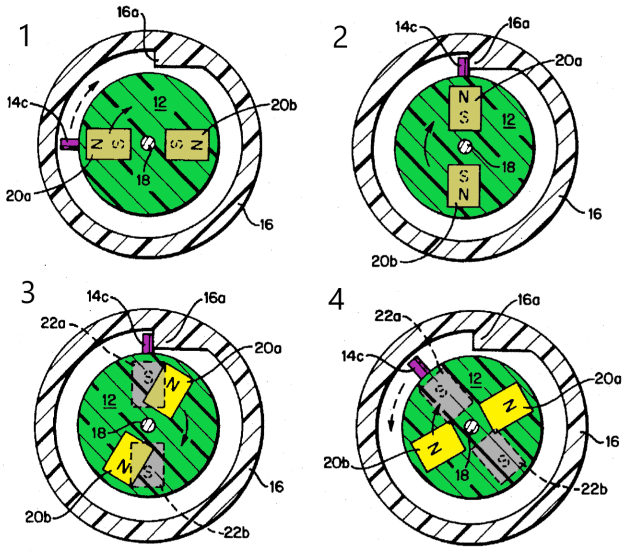

Figure 71. Schematic representation of the different stages during the operation of the magnetic transmission. Step 1: both parts of the coupling are connected through the magnetic connection and both parts rotate together. Step 2: the pin engages the stop in the housing. Step 3: the shaft driven by the motor continues to rotate, the stop holds the second shaft and the magnetic connection is decoupled. Step 4: the magnets attract each other and in response the non driven shaft moves in the opposite direction until the magnetic connection is re-established. Adapted from: [85]

is shown in figure 72. The inner cutting tube (blue) extends out of the back of the instrument and has a dialling knob (red) attached to it. The rear end of the cutting tube is connected to a control system that applies a vacuum to the instrument. The housing of the instrument is connected to the outer tube of the instrument, and at the distal end it also contains a gripping knob. A knurling pattern is placed on the exterior surface of both knobs to enhance the grip of the user. The user is supposed to grip both the knob of the inner cutter and the housing of the instrument. Subsequently both components need to be rotated in opposing directions by the user. This will open and close the cutting port located in the outer tube, and will sever the vitreous. In the housing of the instrument there are constraints that ensure that there is minimal translating movement between the inner and outer tube when the instrument is actuated.

10.3. Combined translating and rotating cutters.

The following section describes mechanisms that drive simultaneously translating and rotating cutters.

10.3.1. Fluidic

This section contains the patents that describe simultaneously translating and rotating cutters which are driven by a fluidic engine.

Pin in guiding slot

The mechanism described in [59] details how a pin and slot mechanism could be used to achieve a simultaneously

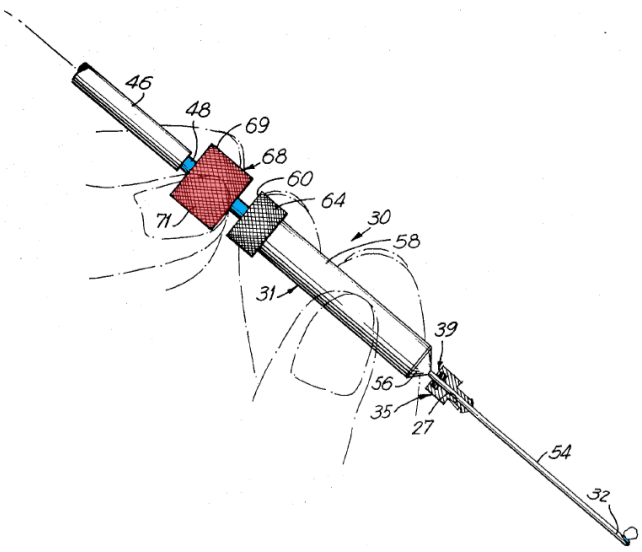

Figure 72. Schematic representation of the manually rotated mechanism. Relevant Components: 31 = housing, 35 = trocar port to provide access into the eye, 46 = vacuum line, 54 = outer tube, 60 = knob attached to the housing, 68 = knob attached to the inner cutting tube. Adapted from: [95].

translating and rotating movement of the inner cutting tube. A schematic drawing of this system is shown in figure 73. A piston type mechanism that is operated by pressurized air pulses from a control system is used to move a drive shaft up and down. This drive shaft contains a pin that engages a slot formed in the handle of the instrument. The cutter is rigidly attached to the drive shaft. The slot is formed in such a manner that the inner cutting tube is rotated when the inner tube is (almost) in contact with the closed distal end of the stationary outer tube. The drive shaft is connected to the actuator in such a manner that it allows for rotation of the drive shaft.

Screw mechanism

In [60] a mechanism is described that can also generate a simultaneous rotating and translating movement of the inner cutting tube. A schematic drawing of the mechanism is shown in figure 74. This mechanism also uses a pneumatic mechanism that is actuated using pressure pulses provided by a control system. An example of a suitable pneumatic mechanism is a piston actuator (red). The described mechanism is biased, and uses a spring (pink) for the retracting movement of the cutter (opening of port). The piston actuator drives a drive shaft (purple), to which in turn, the inner cutting tube (blue) is connected. This drive shaft is connected to the piston actuator in such a way that it allows for rotation of the drive shaft. The inner cutter is rigidly fixated to the drive shaft. Formed in the drive shaft are helical grooves, these grooves interact with inward facing protrusions formed in the housing. When the piston presses down on the drive shaft, the downward movement is converted into a combined translating and rotating movement of the cutter. When the air pressure reduces to a certain level,

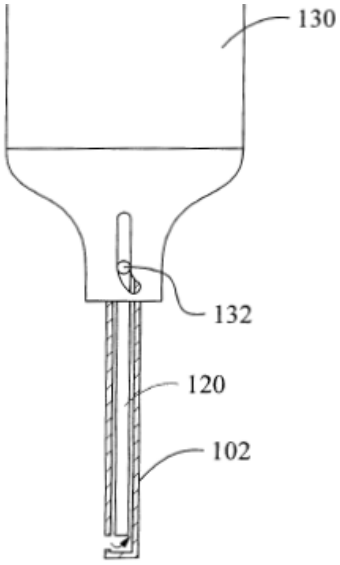

Figure 73. Schematic representation of the pin and slot mechanism. Components: 130 = Engine, 132 = Pin + slot, 120 = Lumen of inner cutting tube, 102 = Outer tube Adapted from: [59]

the spring (green) will drive the inner cutter upward and the cutter will retract and rotate in the opposite direction.

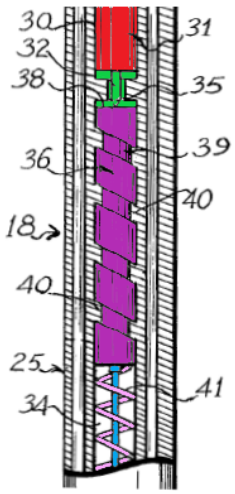

Figure 74. Schematic representation of the screw mechanism, Relevant components: 25 = Housing, 31 = Piston actuator, 36 = Drive shaft, 39 = Helical groove, 40 = Inward protrusion formed in housing, 41 = Compression spring. Adapted from: [60].

10.3.2. Electromagnetic

This section contains the patents that describe simultaneously translating and rotating cutters which are driven by an electromagnetic engine.

Magnetic coupling for combined movement

Patents [89]–[91] all describe a mechanism to drive a simultaneously rotating and translating cutter using a magnetic coupling. Two schematic drawings are shown of the

mechanism, one is a isometric view, shown in figure 75, the second is a cross-section drawing, shown in figure 76. The mechanism consists of a motor that continuously rotates a connector, attached to this connector is a magnetic ring (green). In this magnetic ring are two pairs of evenly spaced opposing magnets (yellow), the magnet pairs have an offset to each other along the longitudinal axis of the instrument. The hollow cutter (blue) is positioned distally from the magnetic ring, rigidly attached to the cutter is a tubular magnet (grey & purple) with a central hole. A shaft extends from the engine through the centre of the magnetic ring, and through the hole in the tubular magnet into the hollow cutting tube, to stabilize the cutter. Distally to the tubular magnet is a ”resilient coupling” (pink), this coupling is made from a pliable material with elastic properties, and acts as a spring. It connects the cutter to the housing of the instrument and has the function of limiting the movement, and subsequently providing a return force in the opposite direction to achieve reciprocal motion. When the motor rotates the magnetic ring, the tubular magnet will also be rotated because of the magnetic coupling between the magnetic ring and the tubular magnet. Only one of the magnet pairs in the ring is magnetically coupled to the tubular magnet at any given moment. When the rotation reaches the limit imposed by the resilient coupling, the currently coupled magnet pair will be decoupled from the tubular magnet. This is due to the fact that the cutter can't rotate further while the motor keeps rotating the magnetic ring, causing the magnet pair and tubular magnet to decouple. In response, the cutter assembly will rotate in the opposite direction because of the force provided by the resilient coupling and attraction to the second magnet pair. The magnet ring will continue to be rotated by the engine, moving the second magnet pair closer to the tubular magnet. Eventually a connection will be formed between the tubular magnet and the second magnet pair, causing them to move in the same direction again. This process will repeat itself and causes the reciprocal rotational movement of the cutter. The translating reciprocal movement is caused by the fact that the magnet pairs inside the ring have a longitudinal offset. Because each magnet pair will intermittently connect with the tubular magnet, a reciprocating translating movement of the cutter is also established.

Piezoelectric actuator and rotating motor

Patent [92] describes a mechanism to independently translate and rotate the cutter of a vitreous removal instrument by means of a linear piezoelectric actuator and rotating motor. A schematic drawing of the mechanism can be seen in figure 77. The mechanism consists of a motor that is designed to independently rotate a portion of the instrument, and a piezoelectric crystal which generates a translating movement of the cutter. A stem extends from both the piezoelectric crystal, and the rotary motor to a motor coupling, which links them. The function of the motor coupling is to transmit the rotational movement of the motor to the stem, and to insulate the motor from the piezoelectric crystals and corresponding power supply.

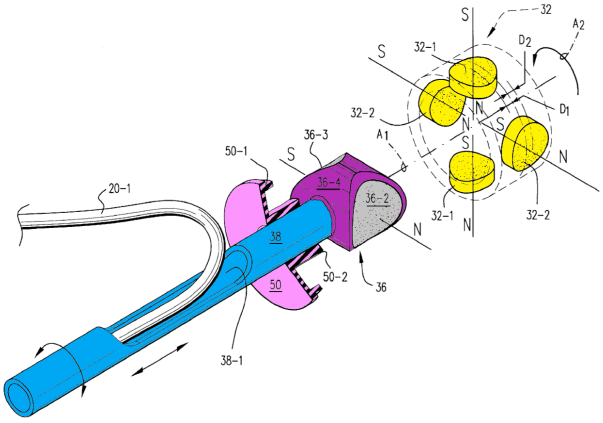

Figure 75. An isometric schematic representation of the magnetic coupling mechanism. Relevant components: 20-1 = vacuum/aspiration line, 32 = driven ring, containing 2 magnet pairs, 32-1 = magnet pair 1, 32-2 = magnet pair 2, D1 = offset of magnet pair one, to centre line of ring, D2 = offset of magnet pair two, to centre line of ring, 36-2 = north pole of tubular magnet, 36-3 = south pole of tubular magnet, 36-4 = housing of tubular magnet, 38 = cutter, 50 = resilient coupling. Adapted from: [89].

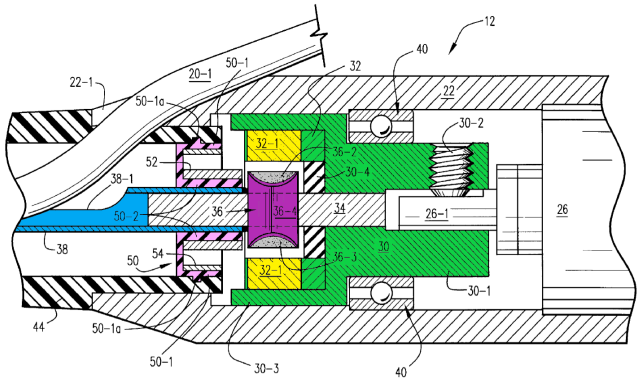

Figure 76. A schematic cross-section of the magnetic coupling mechanism. Relevant components: 20-1 = vacuum/aspiration line, 26 = motor, 26-1 = drive shaft, 30 = connector between magnet ring and drive shaft, 30-4 = vibration damper, 32 = magnet ring, containing 2 magnet pairs, 32-1 = magnet pair 1, 34 = stabilizing shaft, 36-2 = north pole of tubular magnet, 36-3 = south pole of tubular magnet, 36-4 = housing of tubular magnet, 38 = cutter, 40 = ball bearing, 50 = resilient coupling. Adapted from: [89].

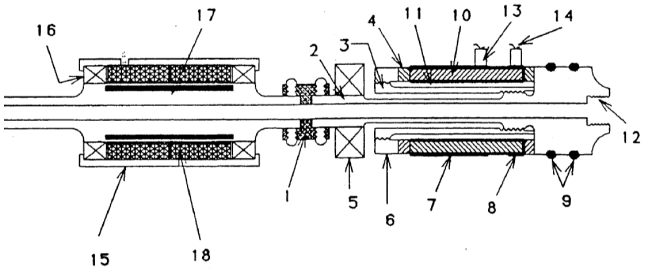

Figure 77. A schematic drawing of the mechanism using a rotating engine and piezoelectric crystal to simultaneously translate and rotate the cutter. Relevant components: 1 = motor coupling, 2 = stem extending from piezoelectric crystal, 5 = bearing, 7 & 8 = electrodes on surface of piezoelectric crystal, 9 = o-ring seal, 10 = piezoelectric crystal, 12 = connection for cutter, 13 = brush , 14 = spring, 15 = housing, 17 = rotating armature of motor, 18 = windings of electrical motor, Adapted from: [92].

11. Appendix B

This appendix contains the sketches that show driving mechanisms that were based on a bellows actuator and a McKibben actuator.

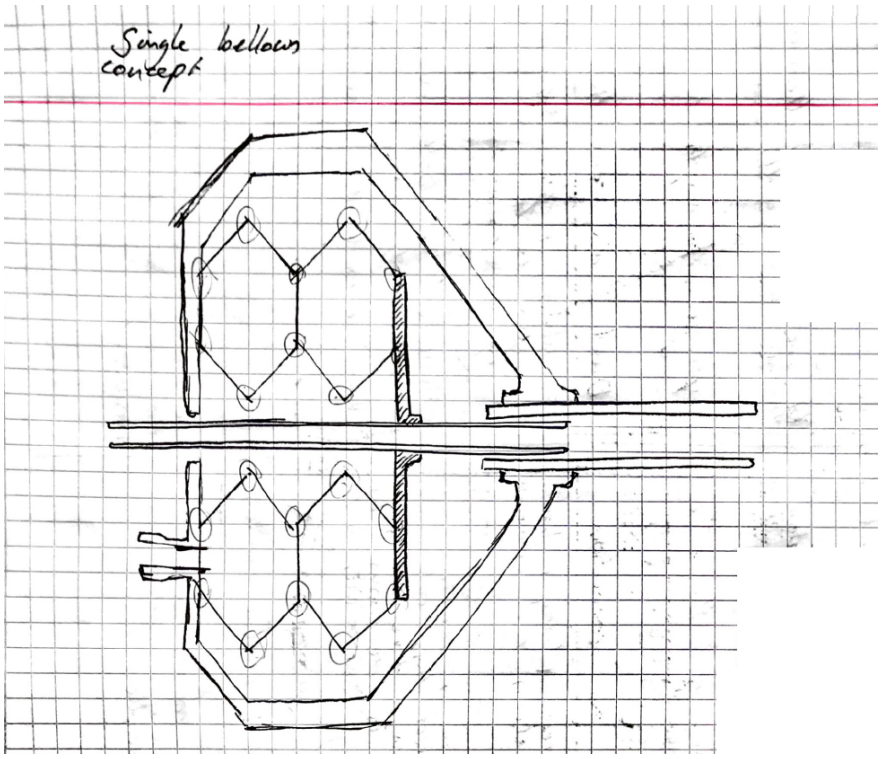

Figure 78. Sketch showing a driving mechanism which is based around a round bellows actuator.

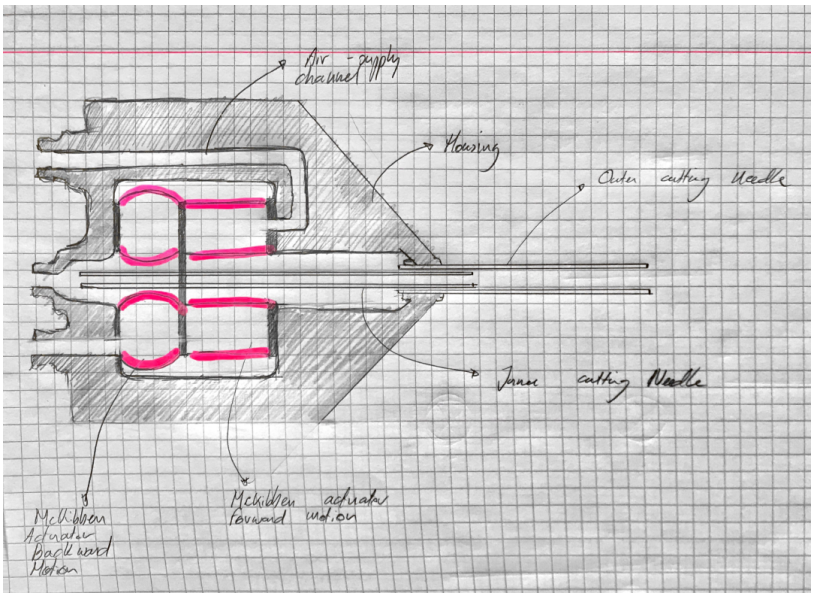

Figure 79. Sketch showing a driving mechanism which is based around a set of two round McKibben actuators to move the inner cutting needle.

12. Appendix C

This appendix shows the construction drawings with all the dimensions of the prototype that was used during testing.

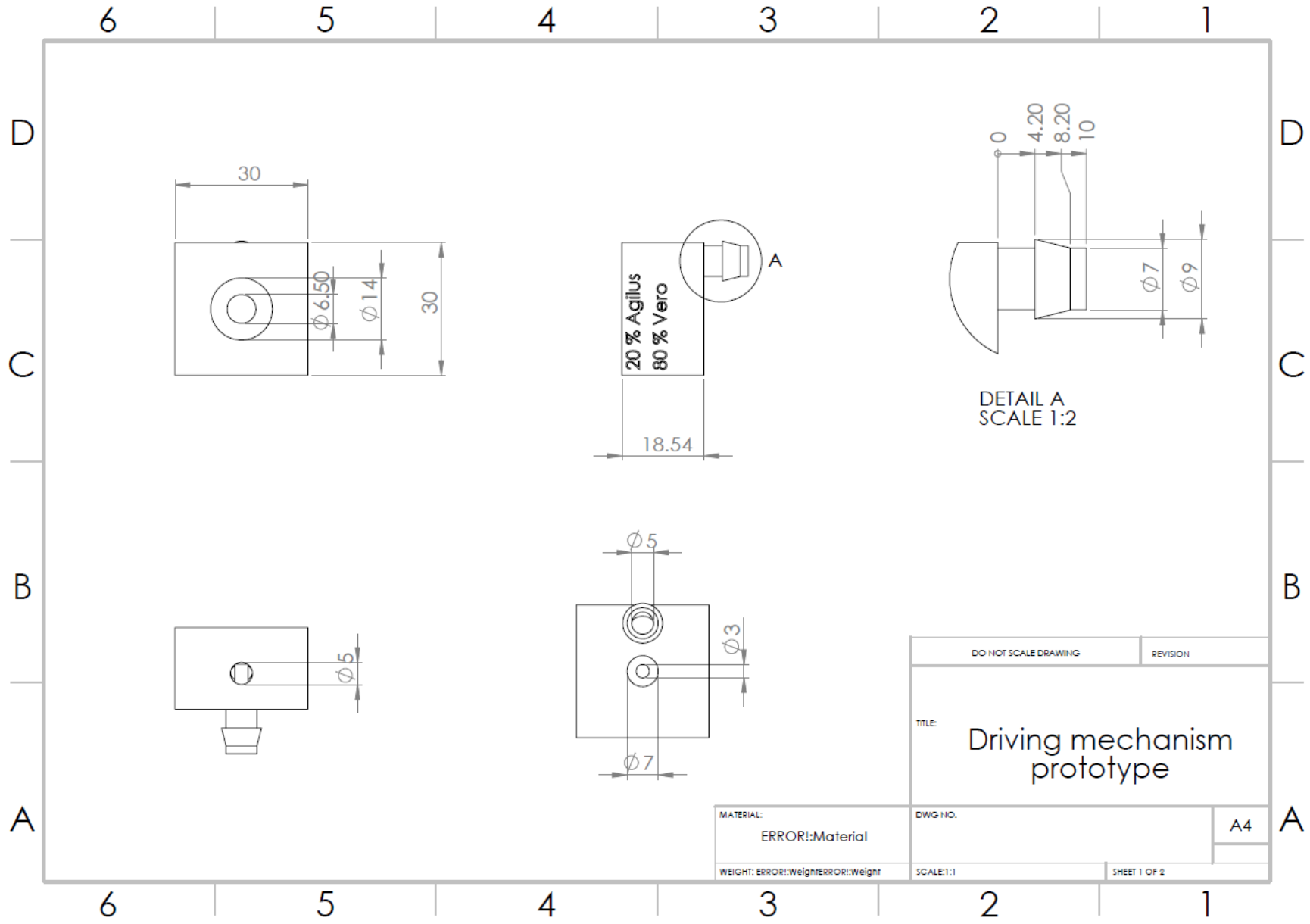
30
Ø6.50
Ø14
30
20 % Agilus
80 % Vero
A
18.54
0
4.20
8.20
10
Ø7
Ø9
DETAIL A
SCALE 1:2
Ø5
5
Ø5
Ø3
Ø7
DO NOT SCALE DRAWING
REVISION
TITLE:
Driving mechanism prototype
MATERIAL:
ERROR!:Material
DWG NO.
A4
WEIGHT: ERROR!:WeightERROR!:Weight
SCALE:1:1
SHEET 1 OF 2

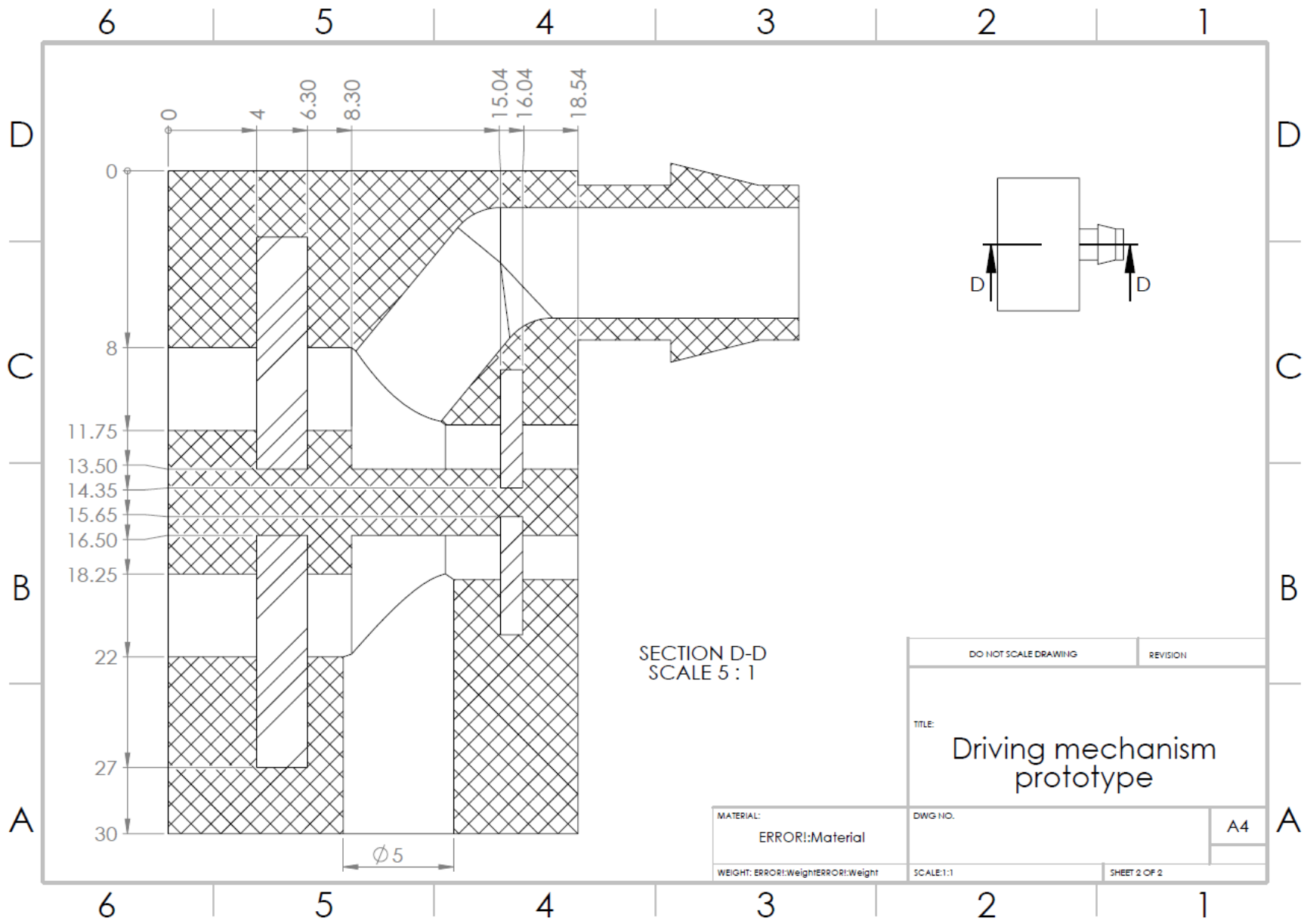
6
5
4
3
2
1
D
C
B
A
0
4
6.30
8.30
15.04
16.04
18.54
0
8
11.75
13.50
14.35
15.65
16.50
18.25
22
27
30
Ø5
D
D
SECTION D-D
SCALE 5 : 1
DO NOT SCALE DRAWING
REVISION
TITLE:
Driving mechanism prototype
MATERIAL:
ERROR!:Material
DWG NO.
A4
WEIGHT: ERROR!:WeightERROR!:Weight
SCALE:1:1
SHEET 2 OF 2

13. Appendix D

This appendix houses the construction drawings that were used to fabricate the fixtures which were used to mount the sensor and the samples.

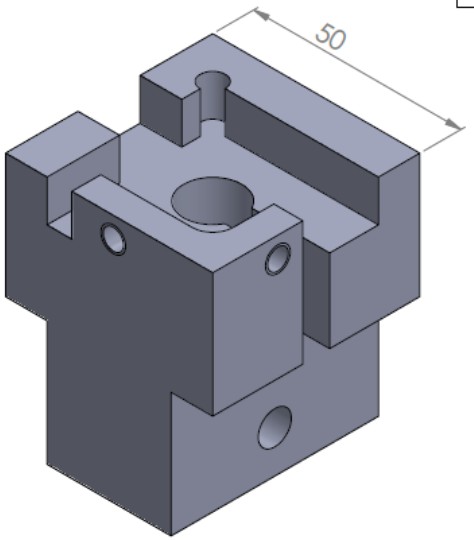

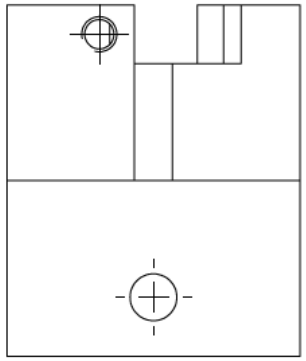

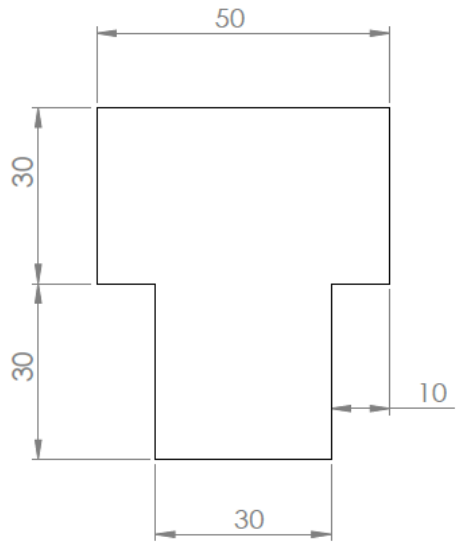

DO NOT SCALE DRAWING	REVISION	
TITLE: ClampingFicture		
MATERIAL:	DWG NO.	A4
WEIGHT:	SCALE:1:1	SHEET 1 OF 2

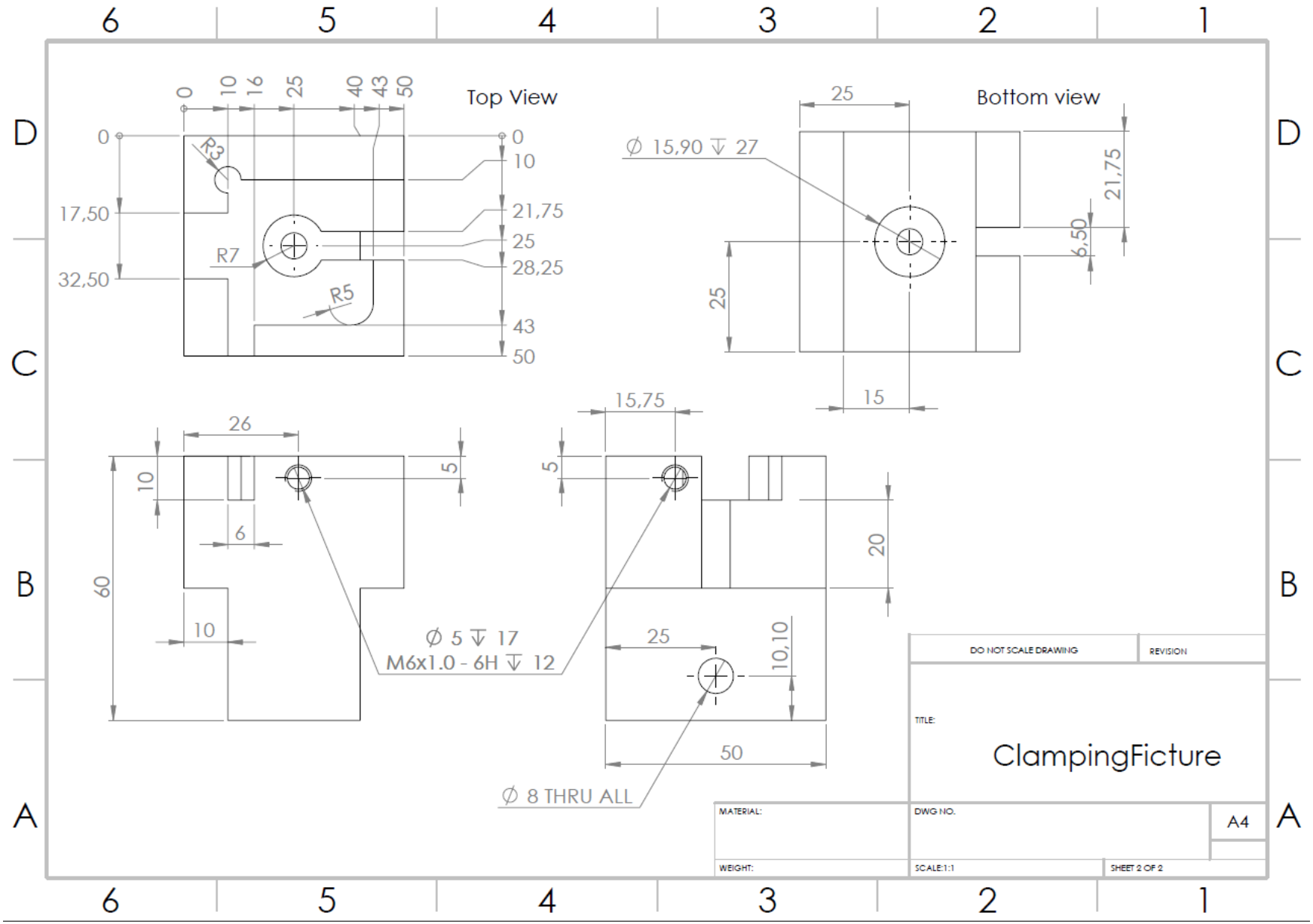
Top View
Bottom view
0
10
16
25
40
43
50
17,50
32,50
R3
R7
R5
21,75
28,25
Ø 15,90 ↧ 27
6,50
15
26
5
6
60
Ø 5 ↧ 17
M6x1.0 - 6H ↧ 12
15,75
20
10,10
Ø 8 THRU ALL
DO NOT SCALE DRAWING
REVISION
TITLE:
ClampingFicture
MATERIAL:
DWG NO.
A4
WEIGHT:
SCALE:1:1
SHEET 2 OF 2

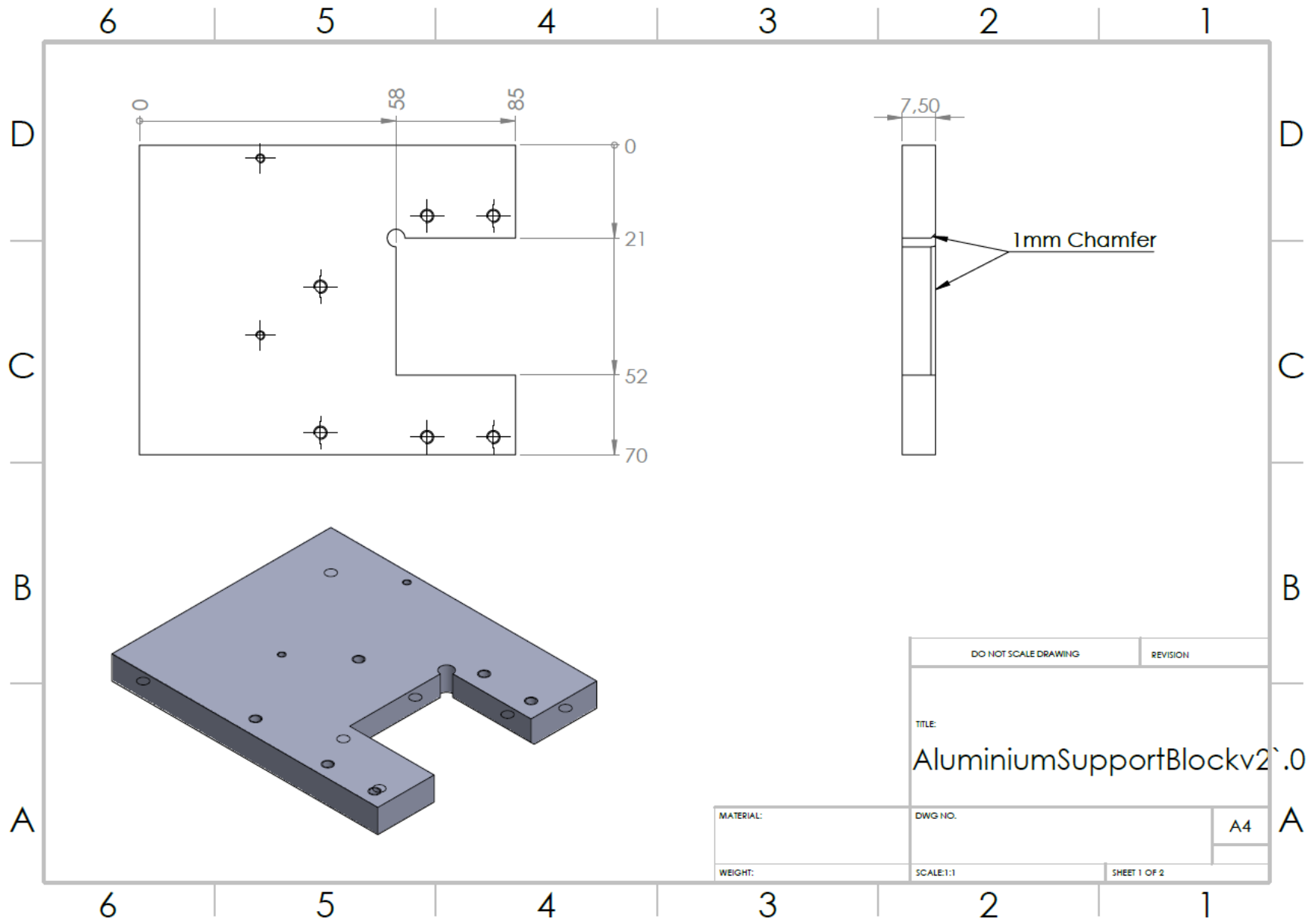
0
58
85
0
21
52
70
7,50
1mm Chamfer
DO NOT SCALE DRAWING
REVISION
TITLE:
AluminiumSupportBlockv2`.0
MATERIAL:
DWG NO.
A4
WEIGHT:
SCALE:1:1
SHEET 1 OF 2

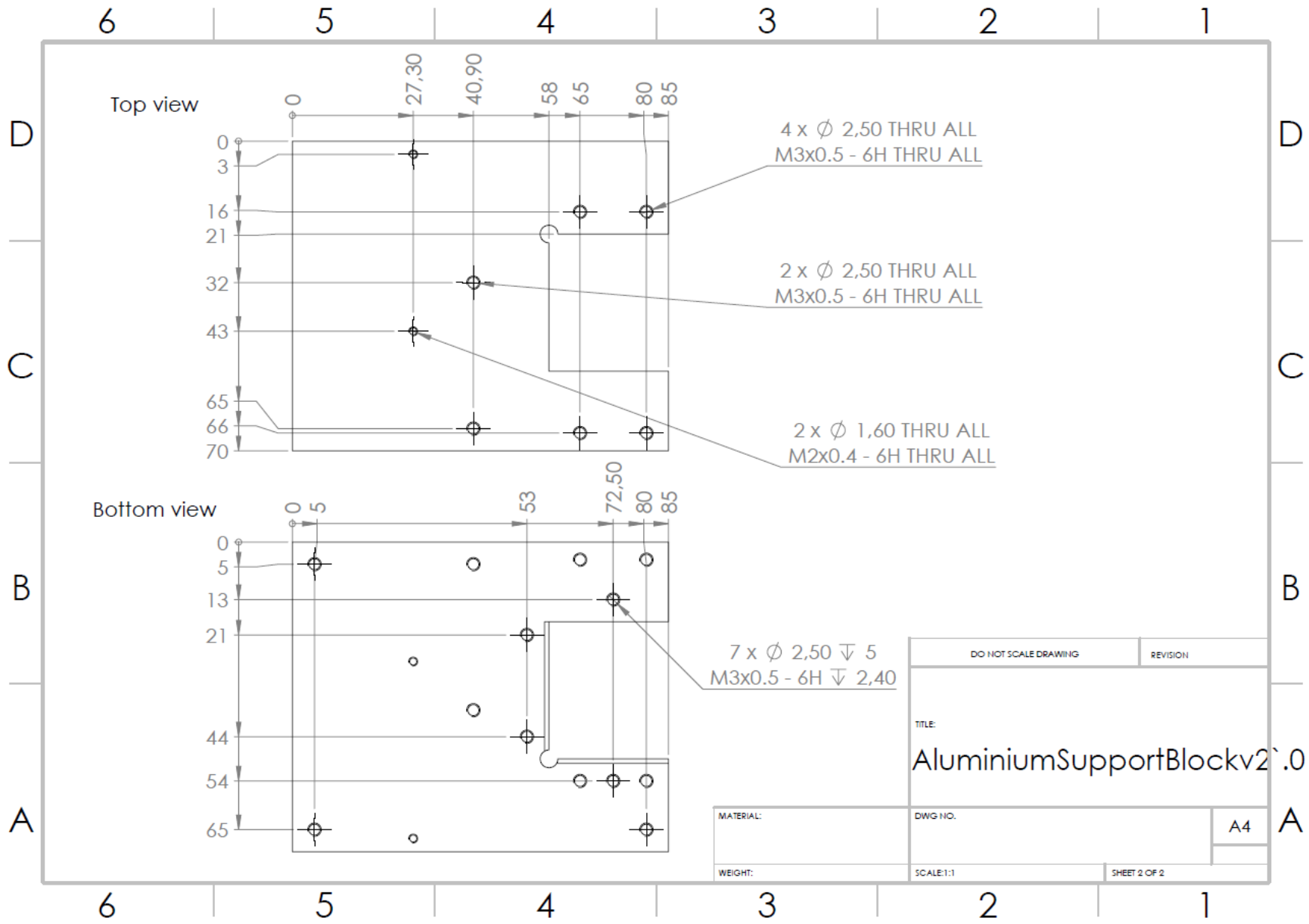
Top view
0
27,30
40,90
58
65
80
85
0
3
16
21
32
43
65
66
70
4 x ∅ 2,50 THRU ALL
M3x0.5 - 6H THRU ALL
2 x ∅ 2,50 THRU ALL
M3x0.5 - 6H THRU ALL
2 x ∅ 1,60 THRU ALL
M2x0.4 - 6H THRU ALL
Bottom view
0
5
53
72,50
80
85
0
5
13
21
44
54
65
7 x ∅ 2,50 ↧ 5
M3x0.5 - 6H ↧ 2,40
DO NOT SCALE DRAWING
REVISION
TITLE:
AluminiumSupportBlockv2`.0
MATERIAL:
DWG NO.
A4
WEIGHT:
SCALE:1:1
SHEET 2 OF 2

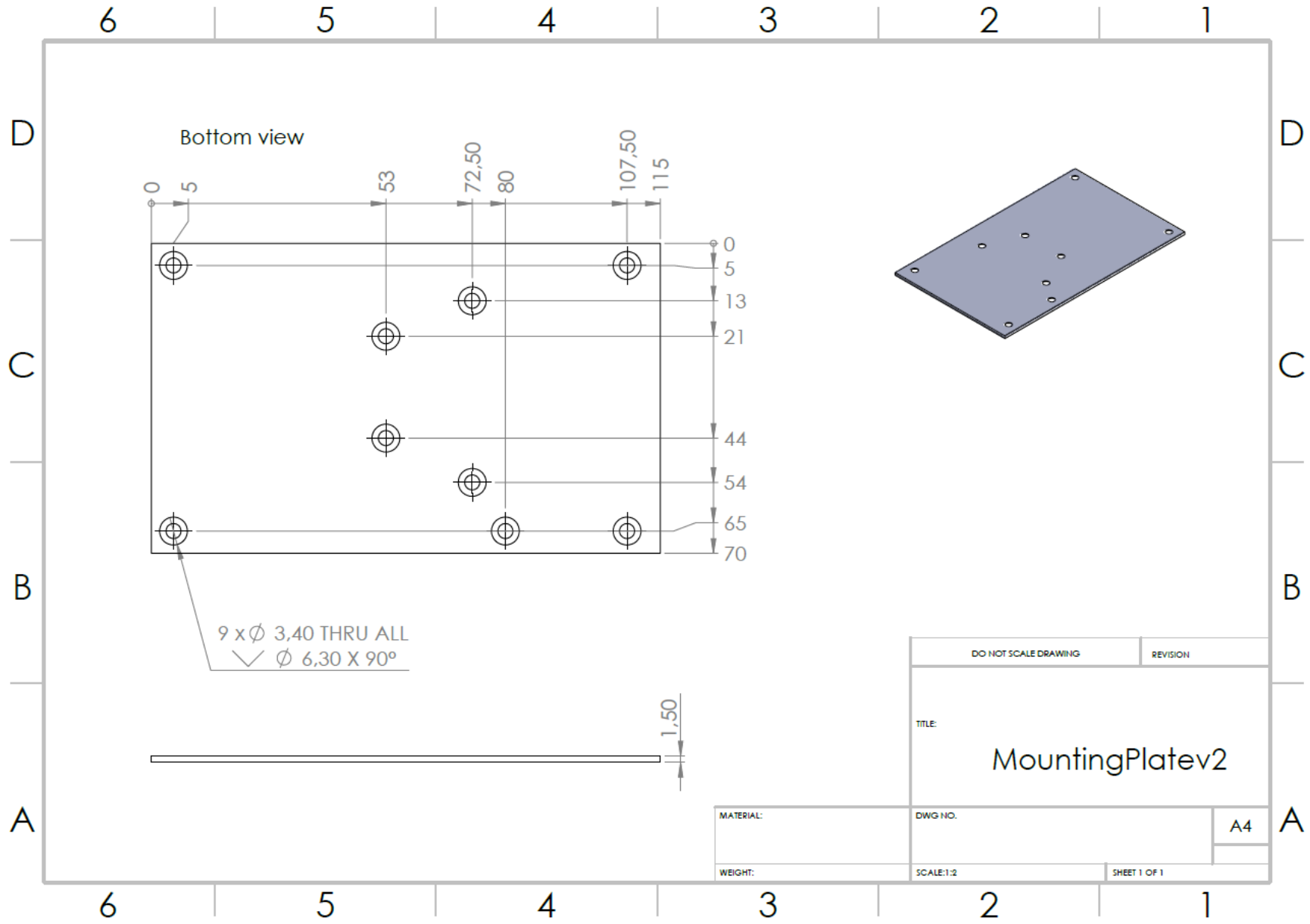
Bottom view
0
5
53
72,50
80
107,50
115
0
5
13
21
44
54
65
70
9 x∅ 3,40 THRU ALL
∅ 6,30 X 90°
1,50
DO NOT SCALE DRAWING
REVISION
TITLE:
MountingPlatev2
MATERIAL:
DWG NO.
A4
WEIGHT:
SCALE:1:2
SHEET 1 OF 1

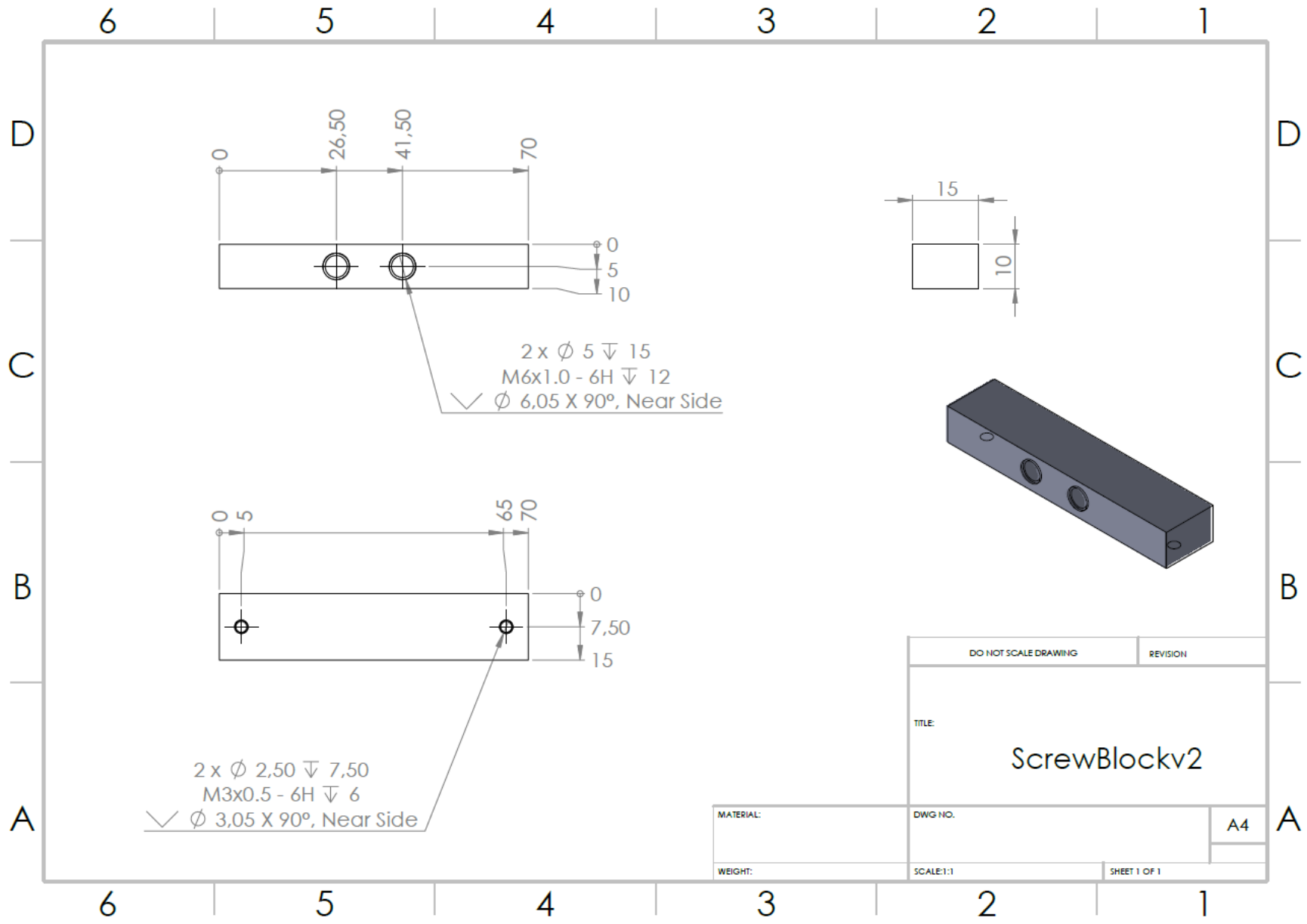
6
5
4
3
2
1
D
C
B
A
0
26,50
41,50
70
0
5
10
2 x ∅ 5 ↧ 15
M6x1.0 - 6H ↧ 12
∅ 6,05 X 90°, Near Side
15
10
0
5
65
70
0
7,50
15
2 x ∅ 2,50 ↧ 7,50
M3x0.5 - 6H ↧ 6
∅ 3,05 X 90°, Near Side
DO NOT SCALE DRAWING
REVISION
TITLE:
ScrewBlockv2
MATERIAL:
DWG NO.
A4
WEIGHT:
SCALE:1:1
SHEET 1 OF 1

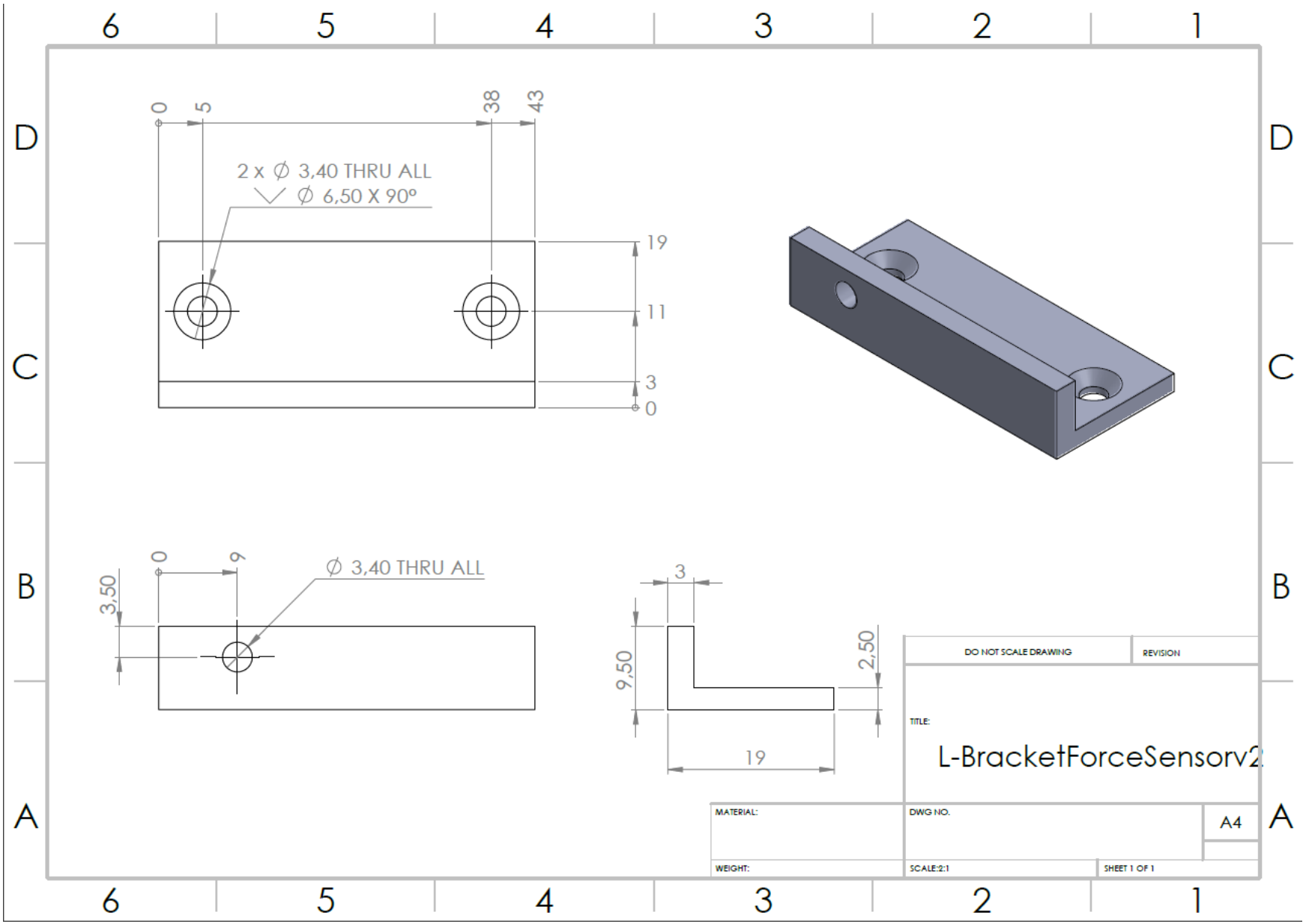
6
5
4
3
2
1
D
C
B
A
0
5
38
43
2 x ∅ 3,40 THRU ALL
∅ 6,50 X 90°
19
11
3
0
0
9
3,50
∅ 3,40 THRU ALL
3
9,50
2,50
19
DO NOT SCALE DRAWING
REVISION
TITLE:
L-BracketForceSensorv2
MATERIAL:
DWG NO.
A4
WEIGHT:
SCALE:2:1
SHEET 1 OF 1

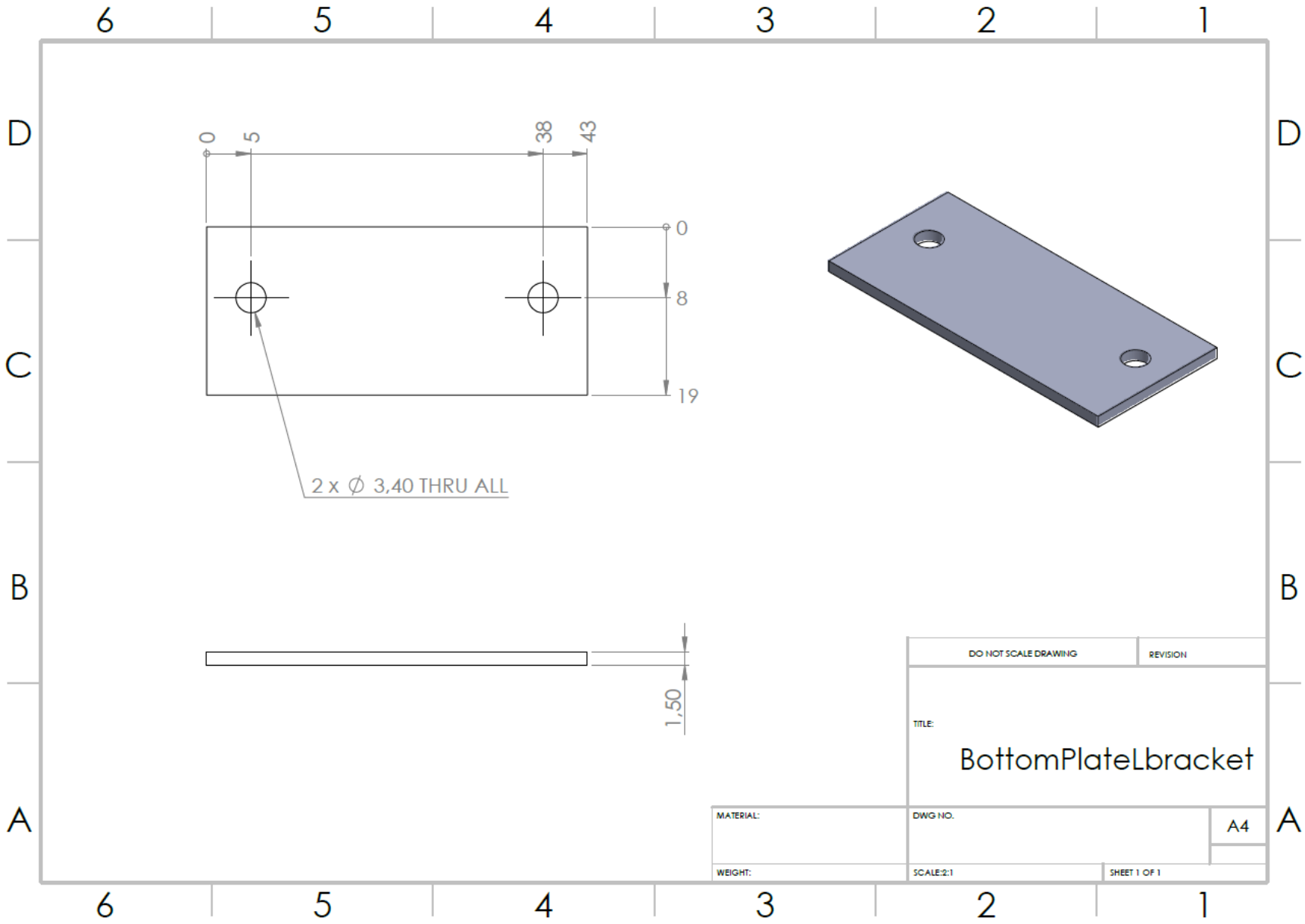
6
5
4
3
2
1
D
C
B
A
0
5
38
43
0
8
19
2 x ∅ 3,40 THRU ALL
1,50
DO NOT SCALE DRAWING
REVISION
TITLE:
BottomPlateLbracket
MATERIAL:
DWG NO.
A4
WEIGHT:
SCALE:2:1
SHEET 1 OF 1

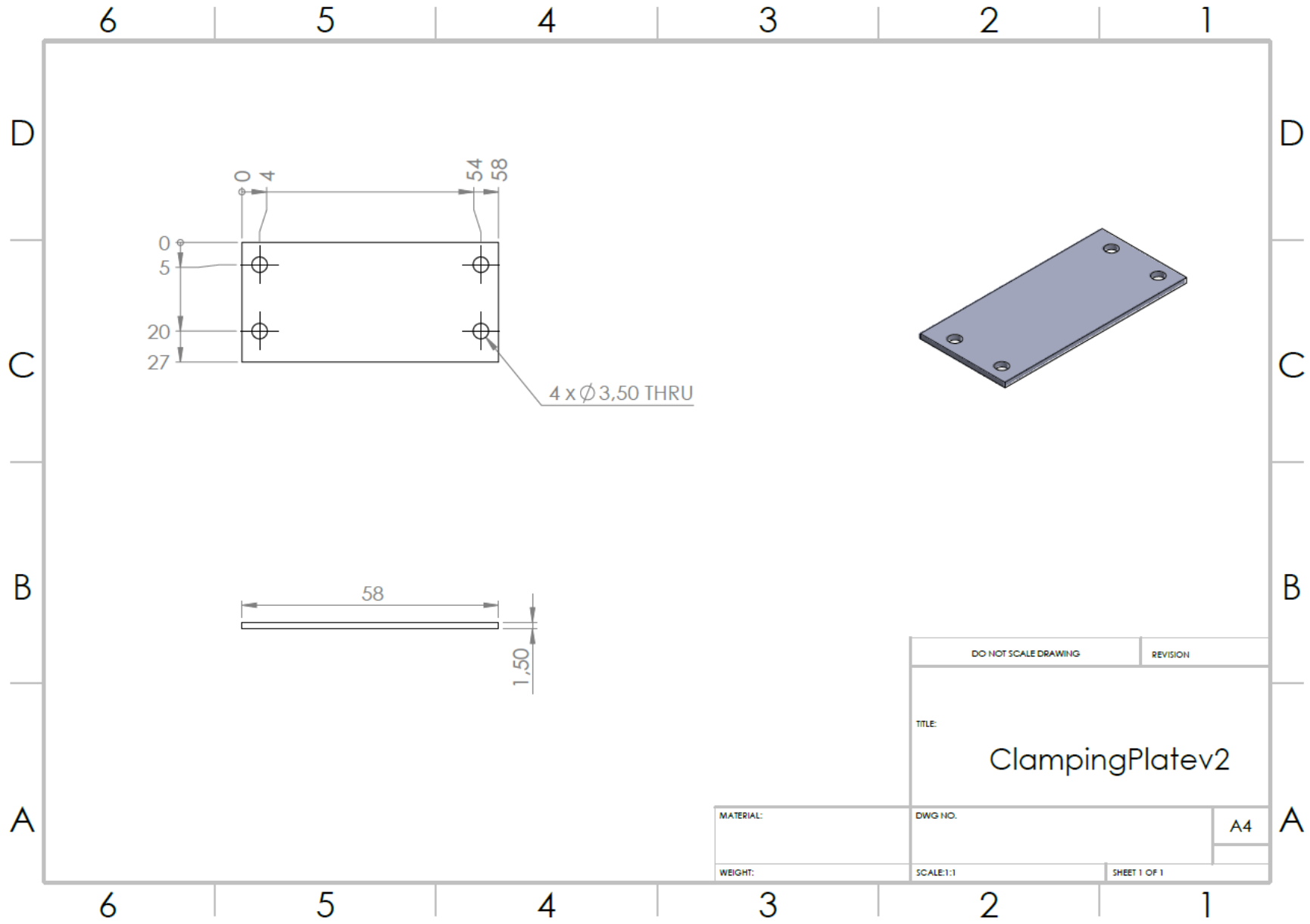
6
5
4
3
2
1
D
C
B
A
0
4
54
58
0
5
20
27
4 x ∅3,50 THRU
58
1,50
DO NOT SCALE DRAWING
REVISION
TITLE:
ClampingPlatev2
MATERIAL:
DWG NO.
A4
WEIGHT:
SCALE:1:1
SHEET 1 OF 1

14. Appendix E

This Appendix contains the interface and block diagram of the labview program that was used to collect the data during the displacement and force tests.

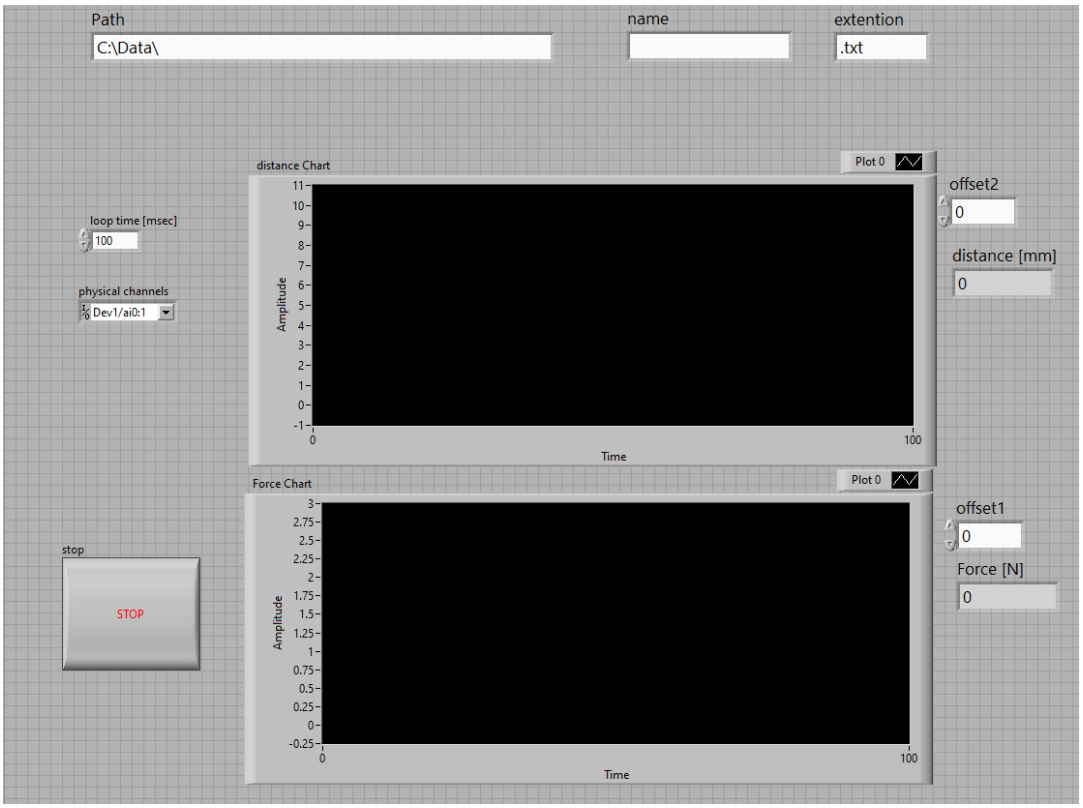

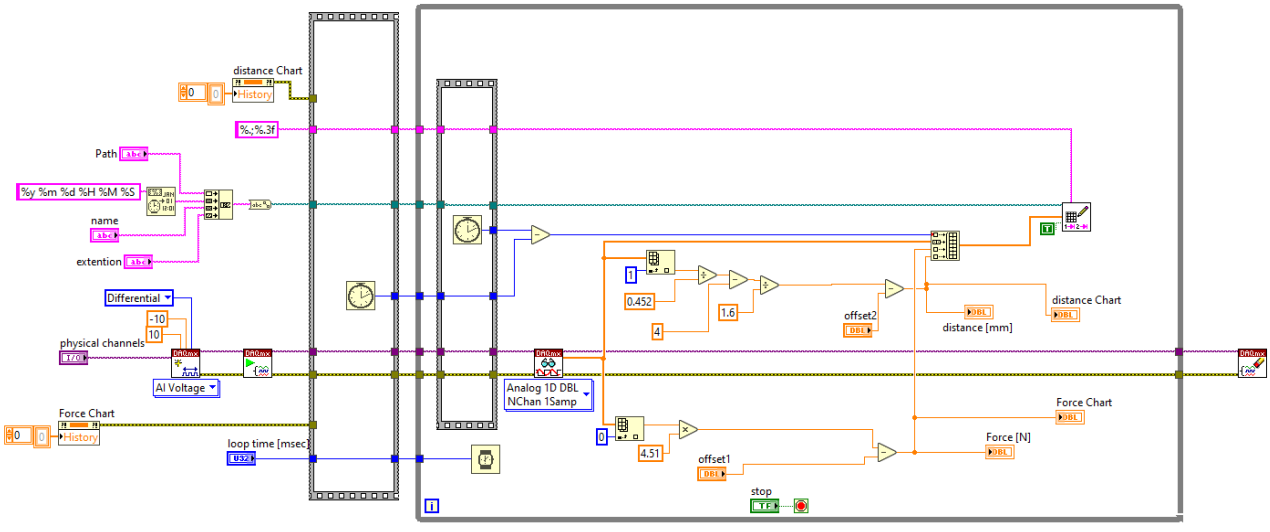

15. Appendix F

This appendix contains all the matlab code that was used to analyse the test data

Hysteresis test data analysis

```
%Load in the sampletypes of the hysteresis tests
load('SampleTypeHysteresis24072020.mat')
load('SampleOrientationHysteresis29072020.mat')

%load in the test data
load('HysteresisTestData24072020.mat')

%Trimming data at the end, zero is inserted at either the force or the
%extension, decided to trim the last data point from all measurements.
ForceHysteresis = ForceHysteresis(2:999,:);
ExtensionHysteresis = ExtensionHysteresis(2:999,:);

%Remove test data from test 7 and 21, failed tests
ForceHysteresis(:,1) = 0;
ExtensionHysteresis(:,1) = 0;
ForceHysteresis(:,11) = 0;
ExtensionHysteresis(:,11) = 0;


%measuring the size of the dataset
S = size(ExtensionHysteresis);

% Setting up the initial values for the counters that are used later in the
% script to sort the measurement data
a = 1;
b = 1;
c = 1;
d = 1;
e = 1;
fff = 1;
g = 1;
h = 1;
i = 1;

for q = 1:S(1,2)

    %Excluding the failed data of test 1 and 11
    if q == 1

    elseif q == 11

    else
    % Determine the cutoff point that is the start of the measurement, this
    % varied from measurement, end point is also determined.
    Positive = find(ForceHysteresis(:,q) > 0.03);
    CUTvec2(q) = Positive(1);
    Positive2 = find(ForceHysteresis(:,q) < 0.03);
    CUTvec3(q) = Positive2(end);

    % Determines the max force and max extension and the respective indices
    % of these values.
    maxForce(q) = max(ForceHysteresis(:,q));
    maxExtension(q) = max(ExtensionHysteresis(:,q));
```

```
    IndexMF = find(ForceHysteresis(:,q) == maxForce(q));
    IndexMaxForce(q) = IndexMF(1);
    IndexME = find(ExtensionHysteresis(:,q) == maxExtension(q));
    IndexMaxExtension(q) = IndexME(1);

    %Shifts the data in such a way that the displacement of the machine is
    %equal to the displacement of the mechanism.
    ExtensionHysteresis(:,q) = ExtensionHysteresis(:,q)-ExtensionHysteresis(CUTvec2(q),q);

    %Finds the force value for a displacement of 0.8 mm for each test that
    %was performed
    Bigger08 = find(ExtensionHysteresis(:,q) > 0.8);
    if Bigger08 > 0
    Index08Long = find(ExtensionHysteresis(1:CUTvec3(q),q) > 0.8);
    Index08(q,1) = Index08Long(1);
    Index08(q,2) = Index08Long(end);
    end

    %Plots the data of each individual test in a figure, hysteresis area,
    %spring energy, max force, and force at 0.8 mm are shown.

% figure
% hold on
% plot(ExtensionHysteresis(CUTvec2(q):CUTvec3(q),q),
ForceHysteresis(CUTvec2(q):CUTvec3(q),q))
% area(ExtensionHysteresis(CUTvec2(q):IndexMaxForce(q),q),
ForceHysteresis(CUTvec2(q):IndexMaxForce(q),q))
% area(ExtensionHysteresis(IndexMaxForce(q):CUTvec3(q),q),
ForceHysteresis(IndexMaxForce(q):CUTvec3(q),q))
% plot(ExtensionHysteresis(IndexMaxForce(q),q),maxForce(q),'k+')
% plot([0 ExtensionHysteresis(IndexMaxForce(q),q)],[0 maxForce(q)],'k-')
% plot(ExtensionHysteresis(Index08(q,1),q),ForceHysteresis(Index08(q,1),q),'ko')
% title(sprintf('Test %d', q))
% xlabel('Displacement [mm]')
% label('Force [N]')

    %Calculates the area in between the loading and unloading curves.
    HysteresisArea(q) = trapz(ExtensionHysteresis(CUTvec2(q):IndexMaxForce(q),q),
    ForceHysteresis(CUTvec2(q):IndexMaxForce(q),q)) -
    trapz(ExtensionHysteresis(IndexMaxForce(q):CUTvec3(q),q),
    ForceHysteresis(IndexMaxForce(q):CUTvec3(q),q));

    LFit(q) = maxForce(q)/ExtensionHysteresis(IndexMaxForce(q),q);

    clear Positive
    clear Positive2

    %The next section sorts the data according to the sample that was
    %tested.
    if SampleTypeHysteresis(q) == 1

    %Displacement vector:
    Agilus80VeroEXT{a} = ExtensionHysteresis(CUTvec2(q):CUTvec3(q),q);
    %Force data vector:
    Agilus80VeroF{a} = ForceHysteresis(CUTvec2(q):CUTvec3(q),q);
    %Force value at 0.8mm displacement (loading)
    Agilus80VeroF08(a) = ForceHysteresis(Index08(q,2),q);
```

```
%Vector containing the orientation data of the samples
OrientationAgilus80Vero(a) = SampleOrientation(q);
%Vector of the slope of the loading curve (Linear fit)
Agilus80VeroLFit(a) = LFit(q);
%Vector containing value of the area in between the loading and unloading
%curves
Agilus80VeroHA(a) = HysteresisArea(q);

%Counter to advance the value once a value has been added to the
%vector, prevents the creation of zero entries.
a = a+1;

elseif SampleTypeHysteresis(q) == 2

Agilus50VeroEXT{b} = ExtensionHysteresis(CUTvec2(q):CUTvec3(q),q);
Agilus50VeroF{b} = ForceHysteresis(CUTvec2(q):CUTvec3(q),q);
OrientationAgilus50Vero(b) = SampleOrientation(q);
Agilus50VeroF08(b) = ForceHysteresis(Index08(q,2),q);
Agilus50VeroLFit(b) = LFit(q);
Agilus50VeroHA(b) = HysteresisArea(q);

b = b+1;

elseif SampleTypeHysteresis(q) == 3

Agilus20VeroEXT{c} = ExtensionHysteresis(CUTvec2(q):CUTvec3(q),q);
Agilus20VeroF{c} = ForceHysteresis(CUTvec2(q):CUTvec3(q),q);
Agilus20VeroF08(c) = ForceHysteresis(Index08(q,2),q);
OrientationAgilus20Vero(c) = SampleOrientation(q);
Agilus20VeroLFit(c) = LFit(q);
Agilus20VeroHA(c) = HysteresisArea(q);

c = c+1;

elseif SampleTypeHysteresis(q) == 4

Agilus80Vero21EXT{d} = ExtensionHysteresis(CUTvec2(q):CUTvec3(q),q);
Agilus80Vero21F{d} = ForceHysteresis(CUTvec2(q):CUTvec3(q),q);
Agilus80Vero21F08(d) = ForceHysteresis(Index08(q,2),q);
OrientationAgilus80Vero21(d) = SampleOrientation(q);
Agilus80Vero21LFit(d) = LFit(q);
Agilus80Vero21HA(d) = HysteresisArea(q);

d = d+1;

elseif SampleTypeHysteresis(q) == 5

Agilus50Vero21EXT{e} = ExtensionHysteresis(CUTvec2(q):CUTvec3(q),q);
Agilus50Vero21F{e} = ForceHysteresis(CUTvec2(q):CUTvec3(q),q);
Agilus50Vero21F08(e) = ForceHysteresis(Index08(q,2),q);
OrientationAgilus50Vero21(e) = SampleOrientation(q);
Agilus50Vero21LFit(e) = LFit(q);
Agilus50Vero21HA(e) = HysteresisArea(q);

e = e+1;

elseif SampleTypeHysteresis(q) == 6
```

```
    Agilus20Vero21EXT{fff} = ExtensionHysteresis(CUTvec2(q):CUTvec3(q),q);
    Agilus20Vero21F{fff} = ForceHysteresis(CUTvec2(q):CUTvec3(q),q);
    Agilus20Vero21F08(fff) = ForceHysteresis(Index08(q,2),q);
    OrientationAgilus20Vero21(fff) = SampleOrientation(q);
    Agilus20Vero21LFit(fff) = LFit(q);
    Agilus20Vero21HA(fff) = HysteresisArea(q);

    fff = fff+1;

    elseif SampleTypeHysteresis(q) == 7

    Agilus80Vero22EXT{g} = ExtensionHysteresis(CUTvec2(q):CUTvec3(q),q);
    Agilus80Vero22F{g} = ForceHysteresis(CUTvec2(q):CUTvec3(q),q);
    Agilus80Vero22F08(g) = ForceHysteresis(Index08(q,2),q);
    OrientationAgilus80Vero22(g) = SampleOrientation(q);
    Agilus80Vero22LFit(g) = LFit(q);
    Agilus80Vero22HA(g) = HysteresisArea(q);

    g = g+1;

    elseif SampleTypeHysteresis(q) == 8

    Agilus50Vero22EXT{h} = ExtensionHysteresis(CUTvec2(q):CUTvec3(q),q);
    Agilus50Vero22F{h} = ForceHysteresis(CUTvec2(q):CUTvec3(q),q);
    Agilus50Vero22F08(h) = ForceHysteresis(Index08(q,2),q);
    OrientationAgilus50Vero22(h) = SampleOrientation(q);
    Agilus50Vero22LFit(h) = LFit(q);
    Agilus50Vero22HA(h) = HysteresisArea(q);

    h = h+1;

    elseif SampleTypeHysteresis(q) == 9

    Agilus20Vero22EXT{i} = ExtensionHysteresis(CUTvec2(q):CUTvec3(q),q);
    Agilus20Vero22F{i} = ForceHysteresis(CUTvec2(q):CUTvec3(q),q);
    Agilus20Vero22F08(i) = ForceHysteresis(Index08(q,2),q);
    OrientationAgilus20Vero22(i) = SampleOrientation(q);
    Agilus20Vero22LFit(i) = LFit(q);
    Agilus20Vero22HA(i) = HysteresisArea(q);

    i = i+1;
    end

  end

end
```

Calculating the average Hysteresis area of 1.3 mm extension test

```
MeanHystA20A80V21 = mean(Agilus80Vero21HA)
MeanHystA20A80V22 = mean(Agilus80Vero22HA(1:(end-3)))
MeanHystA50A50V = mean(Agilus50VeroHA)
MeanHystA50A50V21 = mean(Agilus50Vero21HA)
MeanHystA50A50V22 = mean(Agilus50Vero22HA(1:(end-3)))
MeanHystA80A20V = mean(Agilus20VeroHA)
MeanHystA80A20V21 = mean(Agilus20Vero21HA)
MeanHystA80A20V22 = mean(Agilus20Vero22HA(1:(end-3)))
```

```
% Calculating the average hysteresis are of tne 2.1 mm extension test
MeanHystA20A80V22_2mm = mean(Agilus80Vero22HA((end-2):end))
MeanHystA50A50V22_2mm = mean(Agilus50Vero22HA((end-2):end))
MeanHystA80A20V22_2mm = mean(Agilus20Vero22HA((end-2):end))

MeanHystA20A80V21 =

    9.6015


MeanHystA20A80V22 =

   10.1770


MeanHystA50A50V =

    4.9145


MeanHystA50A50V21 =

    4.1690


MeanHystA50A50V22 =

    4.8666


MeanHystA80A20V =

    3.9041


MeanHystA80A20V21 =

    3.6435


MeanHystA80A20V22 =

    4.0507


MeanHystA20A80V22_2mm =

   23.3892


MeanHystA50A50V22_2mm =

   15.0106


MeanHystA80A20V22_2mm =

   12.9343
```

Plotting the data of the 1.3 mm extension tests

```
%Plot the hysteresis data in a single figure with a separate colour for
%each of the three tested samples.
figure
hold on
title('Hysteresis Plot 1.3 mm extention tests')
xlabel('Displacement [mm]')
ylabel('Force [N]')
xlim([0 1.2])
ylim([0 14])

% The 20Agilus80Vero sample was leak when the tests were conducted
% therefore, results are
% omitted and not plotted.
% for yy = 1:length(OrientationAgilus80Vero)
% if OrientationAgilus80Vero(yy) == 1
%    plot(Agilus80VeroEXT{yy},Agilus80VeroF{yy},'c')
% else
%    plot(Agilus80VeroEXT{yy},Agilus80VeroF{yy},'g')
% end
% end

%Trimming the dataset to remove the 2.1 mm extension tests.
Agilus80Vero22LFit1mm = Agilus80Vero22LFit(1:(end-3));
Agilus50Vero22LFit1mm = Agilus50Vero22LFit(1:(end-3));
Agilus20Vero22LFit1mm = Agilus20Vero22LFit(1:(end-3));

%Calculating the average loading curve for all samples for the 1.3 mm
%extension tests
AVGforceLoading20A80V21 = mean(Agilus80Vero21LFit);
AVGforceLoading20A80V22 = mean(Agilus80Vero22LFit1mm);
AVGforceLoading50A50V = mean(Agilus50VeroLFit);
AVGforceLoading50A50V21 = mean(Agilus50Vero21LFit);
AVGforceLoading50A50V22 = mean(Agilus50Vero22LFit1mm);
AVGforceLoading80A20V = mean(Agilus20VeroLFit(2:end));
AVGforceLoading80A20V21 = mean(Agilus20Vero21LFit);
AVGforceLoading80A20V22 = mean(Agilus20Vero22LFit1mm);

%Multiplying the average loading curve gradient with a number array to
%easily plot a line
xPoints = linspace(0,2.2,100);
Fit20A80V21 = xPoints.*AVGforceLoading20A80V21;
Fit20A80V22 = xPoints.*AVGforceLoading20A80V22;
Fit50A50V = xPoints.*AVGforceLoading50A50V;
Fit50A50V21 = xPoints.*AVGforceLoading50A50V21;
Fit50A50V22 = xPoints.*AVGforceLoading50A50V22;
Fit80A20V = xPoints.*AVGforceLoading80A20V;
Fit80A20V21 = xPoints.*AVGforceLoading80A20V21;
Fit80A20V22 = xPoints.*AVGforceLoading80A20V21;

%Sorting the data according to the orientation of the sample, orientation 1 = forward.
%The data is plotted according to the orientation.
%The force values at a displacement of 0.8 mm are also sorted according to
%the orientation of the sample for later comparisson
for yy = 1:length(OrientationAgilus80Vero21)
```

```
if OrientationAgilus80Vero21(yy) == 1
 A20V80_F = plot(Agilus80Vero21EXT{yy},Agilus80Vero21F{yy},'c');
 A20V80_21F08(yy) = Agilus80Vero21F08(yy);
else
 A20V80_R = plot(Agilus80Vero21EXT{yy},Agilus80Vero21F{yy},'g');
 A20V80_21R08(yy) = Agilus80Vero21F08(yy);
end
end

for yy = 1:length(OrientationAgilus80Vero22)-3
if OrientationAgilus80Vero22(yy) == 1
   plot(Agilus80Vero22EXT{yy},Agilus80Vero22F{yy},'c')
   A20V80_22F08(yy) = Agilus80Vero22F08(yy);
else
   plot(Agilus80Vero22EXT{yy},Agilus80Vero22F{yy},'g')
   A20V80_22R08(yy) = Agilus80Vero22F08(yy);
end
end

for yy = 1:length(OrientationAgilus50Vero)
if OrientationAgilus50Vero(yy) == 1
 A50V50_F = plot(Agilus50VeroEXT{yy},Agilus50VeroF{yy},'m');
 A50V50_F08(yy) = Agilus50VeroF08(yy);
else
 A50V50_R = plot(Agilus50VeroEXT{yy},Agilus50VeroF{yy},'r');
 A50V50_R08(yy) = Agilus50VeroF08(yy);
end
end

for yy = 1:length(OrientationAgilus50Vero21)
if OrientationAgilus50Vero21(yy) == 1
   plot(Agilus50Vero21EXT{yy},Agilus50Vero21F{yy},'m')
   A50V50_21F08(yy) = Agilus50Vero21F08(yy);
else
   plot(Agilus50Vero21EXT{yy},Agilus50Vero21F{yy},'r')
   A50V50_21R08(yy) = Agilus50Vero21F08(yy);
end
end

for yy = 1:length(OrientationAgilus50Vero22)-3
if OrientationAgilus50Vero22(yy) == 1
   plot(Agilus50Vero22EXT{yy},Agilus50Vero22F{yy},'m')
   A50V50_22F08(yy) = Agilus50Vero22F08(yy);
else
   plot(Agilus50Vero22EXT{yy},Agilus50Vero22F{yy},'r')
   A50V50_22R08(yy) = Agilus50Vero22F08(yy);
end
end

for yy = 1:length(OrientationAgilus20Vero)
if OrientationAgilus20Vero(yy) == 1
A80V20_F = plot(Agilus20VeroEXT{yy},Agilus20VeroF{yy},'k');
A80V20_F08(yy) = Agilus20VeroF08(yy);
else
A80V20_R = plot(Agilus20VeroEXT{yy},Agilus20VeroF{yy},'b');
A80V20_R08(yy) = Agilus20VeroF08(yy);
end
end
```

```
for yy = 1:length(OrientationAgilus20Vero21)
if OrientationAgilus20Vero21(yy) == 1
   plot(Agilus20Vero21EXT{yy},Agilus20Vero21F{yy},'k')
   A80V20_21F08(yy) = Agilus20Vero21F08(yy);
else
   plot(Agilus20Vero21EXT{yy},Agilus20Vero21F{yy},'b')
   A80V20_21R08(yy) = Agilus20Vero21F08(yy);
end
end

for yy = 1:length(OrientationAgilus20Vero22)-3
if OrientationAgilus50Vero22(yy) == 1
   plot(Agilus20Vero22EXT{yy},Agilus20Vero22F{yy},'k')
   A80V20_22F08(yy) = Agilus20Vero22F08(yy);
else
   plot(Agilus20Vero22EXT{yy},Agilus20Vero22F{yy},'b')
   A80V20_22R08(yy) = Agilus20Vero22F08(yy);
end
end

%Plotting the average loading curve lines in the figure.
Fit = plot(xPoints,Fit20A80V21,'k-','LineWidth',1);
plot(xPoints,Fit20A80V22,'k-','LineWidth',1)
plot(xPoints,Fit50A50V,'k-','LineWidth',1)
plot(xPoints,Fit50A50V21,'k-','LineWidth',1)
plot(xPoints,Fit50A50V22,'k-','LineWidth',1)
plot(xPoints,Fit80A20V,'k-','LineWidth',1)
plot(xPoints,Fit80A20V21,'k-','LineWidth',1)
plot(xPoints,Fit80A20V22,'k-','LineWidth',1)

%Adding a legend
legend([A20V80_F(1) A20V80_R(1) A50V50_F(1) A50V50_R(1) A80V20_F(1) A80V20_R(1) Fit]
,'20Agilus80Vero-Front','20Agilus80Vero-Rear','50Agilus50Vero-Front'
,'50Agilus50Vero-Rear','80Agilus20Vero-Front','80Agilus20Vero-Rear'
,'Avg loading slope')
```

Calculating the mean force values for a displacement of 0.8 mm for all samples according to their orientation

```
%Trimming the zeros out of the vectors
A20V80_21R08(A20V80_21R08==0) = [];
A20V80_22R08(A20V80_22R08==0) = [];
A50V50_F08(A50V50_F08==0)=[];
A50V50_R08(A50V50_R08==0)=[];
A50V50_21F08(A50V50_21F08==0)=[];
A50V50_21R08(A50V50_21R08==0)=[];
A50V50_22F08(A50V50_22F08==0)=[];
A50V50_22R08(A50V50_22R08==0)=[];
A80V20_F08(A80V20_F08==0)=[];
A80V20_R08(A80V20_R08==0)=[];
A80V20_21F08(A80V20_21F08==0)=[];
A80V20_21R08(A80V20_21R08==0)=[];
A80V20_22F08(A80V20_22F08==0)=[];
A80V20_22R08(A80V20_22R08==0)=[];

%Calculating the average force at a displacement of 0.8 mm for all tested
%samples.

avg_A20V80_21R08 = mean(A20V80_21R08)
```

```
avg_A20V80_22R08 = mean(A20V80_22R08)
avg_A20V80_21F08 = mean(A20V80_21F08)
avg_A20V80_22F08 = mean(A20V80_22F08)
avg_A50V50_F08 = mean(A50V50_F08)
avg_A50V50_R08 = mean(A50V50_R08)
avg_A50V50_21F08 = mean(A50V50_21F08)
avg_A50V50_21R08 = mean(A50V50_21R08)
avg_A50V50_22F08 = mean(A50V50_22F08)
avg_A50V50_22R08 = mean(A50V50_22R08)
avg_A80V20_F08 = mean(A80V20_F08)
avg_A80V20_R08 = mean(A80V20_R08)
avg_A80V20_21F08 = mean(A80V20_21F08)
avg_A80V20_21R08 = mean(A80V20_21R08)
avg_A80V20_22F08 = mean(A80V20_22F08)
avg_A80V20_22R08 = mean(A80V20_22R08)
```

Calculating the average of the loading curves for the 2.1 mm extension tests.

```
Agilus80Vero22LFit2mm = Agilus80Vero22LFit((end-2):end);
Agilus50Vero22LFit2mm = Agilus50Vero22LFit((end-2):end);
Agilus20Vero22LFit2mm = Agilus20Vero22LFit((end-2):end);

AVGforceLoading20A80V22_2mm = mean(Agilus80Vero22LFit2mm);
AVGforceLoading50A50V22_2mm = mean(Agilus50Vero22LFit2mm);
AVGforceLoading80A20V22_2mm = mean(Agilus20Vero22LFit2mm);

Fit20A80V22_2mm = xPoints.*AVGforceLoading20A80V22_2mm;
Fit50A50V22_2mm = xPoints.*AVGforceLoading50A50V22_2mm;
Fit80A20V22_2mm = xPoints.*AVGforceLoading80A20V22_2mm;
```

Plotting the 2.1 mm extension tests

```
figure
hold on
title('Hysteresis Plot 2.1 mm extension tests')
xlabel('Displacement [mm]')
ylabel('Force [N]')
xlim([0 2.2])
ylim([0 20])

for yy = (length(OrientationAgilus80Vero22)-2):length(OrientationAgilus80Vero22)
if OrientationAgilus80Vero22(yy) == 1
   plot(Agilus80Vero22EXT{yy},Agilus80Vero22F{yy},'c')
else
A20V80_2mm = plot(Agilus80Vero22EXT{yy},Agilus80Vero22F{yy},'g');
end
end

for yy = (length(OrientationAgilus50Vero22)-2):length(OrientationAgilus50Vero22)
if OrientationAgilus50Vero22(yy) == 1
   plot(Agilus50Vero22EXT{yy},Agilus50Vero22F{yy},'m')
else
A50V50_2mm = plot(Agilus50Vero22EXT{yy},Agilus50Vero22F{yy},'r');
end
end

for yy = (length(OrientationAgilus20Vero22)-2):length(OrientationAgilus20Vero22)
if OrientationAgilus50Vero22(yy) == 1
   plot(Agilus20Vero22EXT{yy},Agilus20Vero22F{yy},'k')
```

```
else
A80V20_2mm = plot(Agilus20Vero22EXT{yy},Agilus20Vero22F{yy},'b');
end
end

Fit_2mm = plot(xPoints,Fit80A20V22_2mm,'k-','LineWidth',1);
plot(xPoints,Fit50A50V22_2mm,'k-','LineWidth',1)
plot(xPoints,Fit20A80V22_2mm,'k-','LineWidth',1)

legend([A20V80_2mm(1) A50V50_2mm(1) A80V20_2mm(1) Fit_2mm(1)],'20Agilus80Vero-Rear'
,'50Agilus50Vero-Rear','80Agilus20Vero-Rear','Avg loading slope')
```

Displacement Data Analysis script

```
clear all
close all

%Load in the pressure data for each of the displacement tests
%Load sample type used in each test, 1 = 20Agilus80Vero, 2= 50AGilus50Vero,
%3= 80Agilus20Vero
load('DisplacementTestingPRESSURE+SAMPLETYPE27072020.mat')

% Specify the folder where the files live.
myFolder = 'C:\Users\Maarten\Documents\Tu Delft\BME (Master)\MEP
(afstuderen)\Graduation Project\Testing Files\DATA-failsRemoved\AllDisplacementTests';
% Check to make sure that folder actually exists.  Warn user if it doesn't.
if ~isfolder(myFolder)
    errorMessage = sprintf('Error: The following folder does not exist:
    \n%s\nPlease specify a new folder.', myFolder);
    uiwait(warndlg(errorMessage));
    myFolder = uigetdir(); % Ask for a new one.
    if myFolder == 0
         % User clicked Cancel
         return;
    end
end

%Counters to regulate size of the storage of sample specific data
  g = 1;
  z = 1;
  zz = 1;
  zzz = 1;
  h = 1;
  t = 1;
  tt = 1;
  ttt = 1;
  w = 1;
  b = 1;
  bb = 1;
  bbb = 1;
  o = 1;
  qq = 1;
  pp = 1;
  ooo = 1;
  qqq = 1;
  ppp = 1;

% Get a list of all files in the folder with the desired file name pattern.
filePattern = fullfile(myFolder, '*.txt'); % Change to whatever pattern you need.
theFiles = dir(filePattern);

for k = 1 : length(theFiles)

    baseFileName = theFiles(k).name;
    fullFileName = fullfile(theFiles(k).folder, baseFileName);
    fprintf(1, 'Now reading %s\n', fullFileName);

    %load each individual measurement data set and extract the time and
    %displacement data
```

```
singleTestDATA = load(fullFileName);
%storing the time data from a single measurement in the time vector
Time = singleTestDATA(:,1);
%Converting the time vector to seconds instead of ms
Time = Time/1000;
%storing the displacement data of each single measurement in a vector
Displacement = singleTestDATA(:,5);

%correct displacement for standard distance between sensor and sample
%as well as for the fact that the needle moves towards the sensor, the
%data now shows the positive displacement of the needle.
CorrectedDisplacement= (Displacement-Displacement(5))*-1;

StartValues(k) = Displacement(5);
EndValues(k) = Displacement(end);

%apply a filter to the data to remove outliers and noise
 %coeff1sec = ones(1, 10)/10;
 %AVGDisp10measurements = filter(coeff1sec,1,CorrectedDisplacement);
 %fDelay = (10-1)/2;

%apply a median filter to see which filter type is best
MedFILTdisplacement = medfilt1(CorrectedDisplacement,10,'truncate');

%calculate the maximum displacement for each measurement
%MaxDisp(k)= max(AVGDisp10measurements);
MaxDisp(k)= max(MedFILTdisplacement);
%find the indices of the maximum values in the data
MaxIndex = find(MedFILTdisplacement == MaxDisp(k));


%find all the points that have a displacement greater than zero
PosDisplacement = find(MedFILTdisplacement > 0.02);
if PosDisplacement > 0
    if PosDisplacement(1) > 1
    StartIndex = PosDisplacement(1)-1;
    else
    StartIndex = PosDisplacement(1);
    end
    TimePos = Time(StartIndex:end);
    nonZeroVALUES = MedFILTdisplacement(StartIndex:end);
else
    TimePos = 0;
    nonZeroVALUES = 0;
end

EightMMDisp = find(MedFILTdisplacement > 0.8);
if EightMMDisp > 0
    Time08mm = Time(EightMMDisp(1));
else
EightMMDisp = 0;
Time08mm = 0;
end

%calculate the time it takes to reach 0.8mm from the start of the
%movement
TimetoEightMMDisp(k) = Time08mm-TimePos(1);
```

```
%Filter out all the negative data points, these are measurements where
%0.8 mm displacement was not reached.

if TimetoEightMMDisp(k)>0
    TimetoEightMMDisp(k) = TimetoEightMMDisp(k);
else
    TimetoEightMMDisp(k) = 0;
end


%Determine the time in between the start of the movement and the
%maximum displacement (first occurance of max disp)

TimetoMAXdisp(k) = Time(MaxIndex(1))-TimePos(1);

%Determine the time between the last maxIndex and the first zero value
%this gives a rough estimation of the time the mechanism takes to
%return to its zero position

LastmIndex = length(MaxIndex);
ZeroVector = find(MedFILTdisplacement < MedFILTdisplacement(2)+0.03);
FirstzeroIndex = find(ZeroVector > MaxIndex(LastmIndex));
zeroPoint(k) = ZeroVector(FirstzeroIndex(1));

Check = MedFILTdisplacement(MaxIndex(end):end) >
(MedFILTdisplacement(MaxIndex(end))-0.01);

if sum(Check) > 0

IndexBelowMax = find(MedFILTdisplacement > (MedFILTdisplacement(MaxIndex(end))-0.01));
dropPoint(k) = IndexBelowMax(end);

else

dropPoint(k) = MaxIndex(end);

end



ReturnTime(k) = Time(zeroPoint(k)) - Time(dropPoint(k));

EightmmPoints =  find(MedFILTdisplacement > 0.8);
EightmmBelowMaxDisp = MaxDisp(k)-0.8;
IndexEightmmBelowMaxDisp = find(MedFILTdisplacement > EightmmBelowMaxDisp);
Check2 = size(EightmmPoints);

if  Check2(:,1) > 1

Reverse08(k) = EightmmPoints(end);
ReturnTimelast08mm(k) = Time(zeroPoint(k)) - Time(Reverse08(k));
ReturnTimefirst08mm(k) = Time(IndexEightmmBelowMaxDisp(end)) - Time(dropPoint(k));

else

ReturnTimelast08mm(k) = 0;
ReturnTimefirst08mm(k) = 0;
```

```
end


%Plot each of the individual displacement measurements to examine them
if k == 175
figure
hold on
raw = plot(Time,CorrectedDisplacement,'b');
%plot(Time,MedFILTdisplacement)
pos = plot(TimePos,nonZeroVALUES,'c');
mx = plot(Time(MaxIndex),MaxDisp(k),'ro');
Eight = plot(Time08mm,0.8,'k*','MarkerSize',5,'LineWidth',2);
zp = plot(Time(zeroPoint(k)),MedFILTdisplacement(zeroPoint(k)),'ko',
'MarkerSize',5,'LineWidth',2);
dp = plot(Time(dropPoint(k)),MedFILTdisplacement(dropPoint(k)),'k+',
'MarkerSize',5,'LineWidth',2);
title(sprintf(baseFileName))
xlabel('Time [s]')
ylabel('Displacement [mm]')
legend([raw(1) pos(1) Eight(1) mx(1) zp(1) dp(1)],'Unfiltered Data',
'Positive Filtered Data','0.8 mm displacement','Max Displacement',
'Zero Position','Drop Point','location','northeast')
end


if SampleType(k) == 1
Agilus80Vero(g,1) = PressureVEC(k);
Agilus80Vero(g,2) = MaxDisp(k);
Agilus80Vero(g,3) = TimetoMAXdisp(k);

Agilus80VeroSTART(g,1) = StartValues(k);
Agilus80VeroEND(g,1) = EndValues(k);

    if TimetoEightMMDisp(k) > 0

        Agilus80VeroDisp08(pp,2) = TimetoEightMMDisp(k);
        Agilus80VeroDisp08(pp,1) = PressureVEC(k);
        Agilus80VeroRTL08(pp,2) = ReturnTimelast08mm(k);
        Agilus80VeroRTL08(pp,1) = MaxDisp(k);
        Agilus80VeroRTF08(pp,1) = MaxDisp(k);
        Agilus80VeroRTF08(pp,2) = ReturnTimefirst08mm(k);

        pp = pp+1;
    end



    if ReturnTime(k) > 0

        Agilus80VeroRT(ppp,2) = ReturnTime(k);
        Agilus80VeroRT(ppp,1) = PressureVEC(k);
        Agilus80VeroRT(ppp,3) = MaxDisp(k);

        ppp = ppp + 1;
    end

g = g+1;
```

```
elseif SampleType(k) == 4
Agilus80Vero21(z,1) = PressureVEC(k);
Agilus80Vero21(z,2) = MaxDisp(k);
Agilus80Vero21(z,3) = TimetoMAXdisp(k);

Agilus80Vero21START(z,1) = StartValues(k);
Agilus80Vero21END(z,1) = EndValues(k);

    if TimetoEightMMDisp(k) > 0

        Agilus80Vero21Disp08(zz,2) = TimetoEightMMDisp(k);
        Agilus80Vero21Disp08(zz,1) = PressureVEC(k);
        Agilus80Vero21RTL08(zz,2) = ReturnTimelast08mm(k);
        Agilus80Vero21RTL08(zz,1) = MaxDisp(k);
        Agilus80Vero21RTF08(zz,2) = ReturnTimefirst08mm(k);
        Agilus80Vero21RTF08(zz,1) = MaxDisp(k);

        zz = zz+1;
    end

    if ReturnTime(k) > 0

        Agilus80Vero21RT(zzz,2) = ReturnTime(k);
        Agilus80Vero21RT(zzz,1) = PressureVEC(k);
        Agilus80Vero21RT(zzz,3) = MaxDisp(k);

        zzz = zzz + 1;
    end

z = z+1 ;

elseif SampleType(k)==2
Agilus50Vero(h,1)= PressureVEC(k);
Agilus50Vero(h,2)= MaxDisp(k);
Agilus50Vero(h,3) = TimetoMAXdisp(k);

Agilus50VeroSTART(h,1) = StartValues(k);
Agilus50VeroEND(h,1) = EndValues(k);

    if TimetoEightMMDisp(k) > 0
        Agilus50VeroDisp08(qq,2) = TimetoEightMMDisp(k);
        Agilus50VeroDisp08(qq,1) = PressureVEC(k);
        Agilus50VeroRTL08(qq,2) = ReturnTimelast08mm(k);
        Agilus50VeroRTL08(qq,1) = MaxDisp(k);
        Agilus50VeroRTF08(qq,1) = MaxDisp(k);
        Agilus50VeroRTF08(qq,2) = ReturnTimefirst08mm(k);

        qq = qq+1;
    end

    if ReturnTime(k) > 0

        Agilus50VeroRT(qqq,2) = ReturnTime(k);
        Agilus50VeroRT(qqq,1) = PressureVEC(k);
        Agilus50VeroRT(qqq,3) = MaxDisp(k);
```

```
        qqq = qqq + 1;
    end

h = h +1;

elseif SampleType(k)== 5
Agilus50Vero21(t,1)= PressureVEC(k);
Agilus50Vero21(t,2)= MaxDisp(k);
Agilus50Vero21(t,3) = TimetoMAXdisp(k);

Agilus50Vero21START(t,1) = StartValues(k);
Agilus50Vero21END(t,1) = EndValues(k);

    if TimetoEightMMDisp(k) > 0
        Agilus50Vero21Disp08(tt,2) = TimetoEightMMDisp(k);
        Agilus50Vero21Disp08(tt,1) = PressureVEC(k);
        Agilus50Vero21RTL08(tt,2) = ReturnTimelast08mm(k);
        Agilus50Vero21RTL08(tt,1) = MaxDisp(k);
        Agilus50Vero21RTF08(tt,1) = MaxDisp(k);
        Agilus50Vero21RTF08(tt,2) = ReturnTimefirst08mm(k);

        tt = tt+1;
    end

    if ReturnTime(k) > 0

        Agilus50Vero21RT(ttt,2) = ReturnTime(k);
        Agilus50Vero21RT(ttt,1) = PressureVEC(k);
        Agilus50Vero21RT(ttt,3) = MaxDisp(k);

        ttt = ttt + 1;
end

t = t +1;

elseif SampleType(k) == 3
Agilus20Vero(w,1)= PressureVEC(k);
Agilus20Vero(w,2)= MaxDisp(k);
Agilus20Vero(w,3)= TimetoMAXdisp(k);

Agilus20VeroSTART(w,1) = StartValues(k);
Agilus20VeroEND(w,1) = EndValues(k);

    if TimetoEightMMDisp(k) > 0
        Agilus20VeroDisp08(o,2) = TimetoEightMMDisp(k);
        Agilus20VeroDisp08(o,1) = PressureVEC(k);
        Agilus20VeroRTL08(o,2) = ReturnTimelast08mm(k);
        Agilus20VeroRTL08(o,1) = MaxDisp(k);
        Agilus20VeroRTF08(o,1) = MaxDisp(k);
        Agilus20VeroRTF08(o,2) = ReturnTimefirst08mm(k);

        o = o+1;
    end

         if ReturnTime(k) > 0

        Agilus20VeroRT(ooo,2) = ReturnTime(k);
        Agilus20VeroRT(ooo,1) = PressureVEC(k);
```

```
            Agilus20VeroRT(ooo,3) = MaxDisp(k);

            ooo = ooo + 1;
        end

    w = w+1;

    elseif SampleType(k) == 6
    Agilus20Vero21(b,1)= PressureVEC(k);
    Agilus20Vero21(b,2)= MaxDisp(k);
    Agilus20Vero21(b,3)= TimetoMAXdisp(k);

    Agilus20Vero21START(b,1) = StartValues(k);
    Agilus20Vero21END(b,1) = EndValues(k);

        if TimetoEightMMDisp(k) > 0
            Agilus20Vero21Disp08(bb,2) = TimetoEightMMDisp(k);
            Agilus20Vero21Disp08(bb,1) = PressureVEC(k);
            Agilus20Vero21RTL08(bb,2) = ReturnTimelast08mm(k);
            Agilus20Vero21RTL08(bb,1) = MaxDisp(k);
            Agilus20Vero21RTF08(bb,1) = MaxDisp(k);
            Agilus20Vero21RTF08(bb,2) = ReturnTimefirst08mm(k);

            bb = bb+1;
        end

             if ReturnTime(k) > 0

            Agilus20Vero21RT(bbb,2) = ReturnTime(k);
            Agilus20Vero21RT(bbb,1) = PressureVEC(k);
            Agilus20Vero21RT(bbb,3) = MaxDisp(k);

            bbb = bbb + 1;
        end

    b = b+1;

    end


end

Agilus80VeroSTART = Agilus80VeroSTART(:,1) - Agilus80VeroSTART(1,1);
Agilus50VeroSTART = Agilus50VeroSTART(:,1) - Agilus50VeroSTART(1,1);
Agilus20VeroSTART = Agilus20VeroSTART(:,1) - Agilus20VeroSTART(1,1);

%Create three separate figures for the three samples that were tested
    figure
    hold on
    title('Pressure vs Max Displacement 20Agilus80Vero')
    xlabel('Pressure [Pa]')
    ylabel('Displacement [mm]')
    plot(Agilus80Vero(:,1),Agilus80Vero(:,2),'g-*')
    %plot(Agilus80Vero(:,1),Agilus80VeroSTART(:,1),'k-+')
    plot(Agilus80Vero21(:,1),Agilus80Vero21(:,2),'g-+')


    figure
```

```
hold on
title('Pressure vs Max Displacement 50Agilus50Vero')
xlabel('Pressure [Pa]')
ylabel('Displacement [mm]')
plot(Agilus50Vero(:,1),Agilus50Vero(:,2),'r-*')
plot(Agilus50Vero21(:,1),Agilus50Vero21(:,2),'r-+')
%plot(Agilus50Vero(:,1),Agilus50VeroSTART(:,1),'k-+')


figure
hold on
title('Pressure vs Max Displacement 80Agilus20Vero')
xlabel('Pressure [Pa]')
ylabel('Displacement [mm]')
plot(Agilus20Vero(:,1),Agilus20Vero(:,2),'b*-')
plot(Agilus20Vero21(:,1),Agilus20Vero21(:,2),'b+-')
%plot(Agilus20Vero(:,1),Agilus20VeroSTART(:,1),'k+-')


figure
hold on
title('Pressure vs Max Displacement all Samples')
xlabel('Pressure [Pa]')
ylabel('Displacement [mm]')

plot(Agilus80Vero(:,1),Agilus80Vero(:,2),'g*-')
plot(Agilus50Vero(:,1),Agilus50Vero(:,2),'r*-')
plot(Agilus20Vero(:,1),Agilus20Vero(:,2),'b*-')
plot(Agilus80Vero21(:,1),Agilus80Vero21(:,2),'g-+')
plot(Agilus50Vero21(:,1),Agilus50Vero21(:,2),'r-+')
plot(Agilus20Vero21(:,1),Agilus20Vero21(:,2),'b+-')

legend('20Agilus80Vero','50Agilus50Vero','80Agilus20Vero','20Agilus80Vero-2.1',
'50Agilus50Vero-2.1','80Agilus20Vero-2.1','Location','northeast')

figure
hold on
title('Pressure vs Time to reach 0.8 mm ')
xlabel('Pressure [Pa]')
ylabel('Time to reach 0.8 mm [s]')

plot(Agilus80VeroDisp08(:,1),Agilus80VeroDisp08(:,2),'g*-')
plot(Agilus50VeroDisp08(:,1),Agilus50VeroDisp08(:,2),'r*-')
plot(Agilus20VeroDisp08(:,1),Agilus20VeroDisp08(:,2),'b*-')
plot(Agilus80Vero21Disp08(:,1),Agilus80Vero21Disp08(:,2),'g+-')
plot(Agilus50Vero21Disp08(:,1),Agilus50Vero21Disp08(:,2),'r+-')
plot(Agilus20Vero21Disp08(:,1),Agilus20Vero21Disp08(:,2),'b+-')
legend('20Agilus80Vero','50Agilus50Vero','80Agilus20Vero','20Agilus80Vero-2.1',
'50Agilus50Vero-2.1','80Agilus20Vero-2.1','Location','northwest')

figure
plot3(Agilus80Vero(:,1),Agilus80Vero(:,2),Agilus80Vero(:,3),'g-*')
title('20Agilus80Vero')
xlabel('Pressure [Pa]')
ylabel('Displacement [mm]')
zlabel('Time to reach max Disp [s]')

view([40 41]);
```

```
grid('on');

figure
plot3(Agilus50Vero(:,1),Agilus50Vero(:,2),Agilus50Vero(:,3),'r-*')
title('50Agilus50Vero')
xlabel('Pressure [Pa]')
ylabel('Displacement [mm]')
zlabel('Time to reach max Disp [s]')

view([40 41]);
grid('on');

figure
plot3(Agilus20Vero(:,1),Agilus20Vero(:,2),Agilus20Vero(:,3),'b-*')
title('80Agilus20Vero')
xlabel('Pressure [Pa]')
ylabel('Displacement [mm]')
zlabel('Time to reach max Disp [s]')

view([40 41]);
grid('on');

figure
hold on
plot3(Agilus80Vero(:,1),Agilus80Vero(:,2),Agilus80Vero(:,3),'g-*')
plot3(Agilus50Vero(:,1),Agilus50Vero(:,2),Agilus50Vero(:,3),'r-*')
plot3(Agilus20Vero(:,1),Agilus20Vero(:,2),Agilus20Vero(:,3),'b-*')
title('Pressure vs Total Displacment vs Time to max Displacement')
xlabel('Pressure [Pa]')
ylabel('Displacement [mm]')
zlabel('Time to reach max Disp [s]')
grid('on');
xlim([0 210000])
view([40 41]);

figure
hold on
plot( Agilus80VeroRT(:,3), Agilus80VeroRT(:,2),'g*-')
plot( Agilus50VeroRT(:,3), Agilus50VeroRT(:,2),'r*-')
plot( Agilus20VeroRT(:,3), Agilus20VeroRT(:,2),'b*-')
plot( Agilus80Vero21RT(:,3), Agilus80Vero21RT(:,2),'g+-')
plot( Agilus50Vero21RT(:,3), Agilus50Vero21RT(:,2),'r+-')
plot( Agilus20Vero21RT(:,3), Agilus20Vero21RT(:,2),'b+-')
title('Max displacement vs return time to initial position')
xlabel('Max displacement [mm]')
ylabel('Return time [s]')
legend('20Agilus80Vero','50Agilus50Vero','80Agilus20Vero','20Agilus80Vero-2.1',
'50Agilus50Vero-2.1','80Agilus20Vero-2.1','Location','northeast')

figure
hold on
plot( Agilus80VeroRTF08(:,1),Agilus80VeroRTF08(:,2),'g*-')
plot( Agilus80Vero21RTF08(:,1),Agilus80Vero21RTF08(:,2),'g+-')
plot( Agilus50VeroRTF08(:,1),Agilus50VeroRTF08(:,2),'r*-')
plot( Agilus50Vero21RTF08(:,1),Agilus50Vero21RTF08(:,2),'r+-')
plot( Agilus20VeroRTF08(:,1),Agilus20VeroRTF08(:,2),'b*-')
plot( Agilus20Vero21RTF08(:,1),Agilus20Vero21RTF08(:,2),'b+-')
title('Max displacement vs time to move first 0.8 mm from Max')
```

```
xlabel('Max displacement [mm]')
ylabel('Time [s]')
xlim([0.8 2])
ylim([0 5])
legend('20Agilus80Vero','20Agilus80Vero-2.1','50Agilus50Vero','50Agilus50Vero-2.1,
'80Agilus20Vero','80Agilus20Vero-2.1','Location','northeast')

figure
hold on
plot( Agilus80VeroRTL08(:,1),Agilus80VeroRTL08(:,2),'g*-')
plot( Agilus80Vero21RTL08(:,1),Agilus80Vero21RTL08(:,2),'g+-')
plot( Agilus50VeroRTL08(:,1),Agilus50VeroRTL08(:,2),'r*-')
plot( Agilus50Vero21RTL08(:,1),Agilus50Vero21RTL08(:,2),'r+-')
plot( Agilus20VeroRTL08(:,1),Agilus20VeroRTL08(:,2),'b*-')
plot( Agilus20Vero21RTL08(:,1),Agilus20Vero21RTL08(:,2),'b+-')
title('Max displacement vs time to move the last 0.8 mm to the base value')
xlabel('Max displacement [mm]')
ylabel('Time [s]')
legend('20Agilus80Vero','20Agilus80Vero-2.1','50Agilus50Vero','50Agilus50Vero-2.1,
'80Agilus20Vero','80Agilus20Vero-2.1','Location','northeast')
```

Force data analysis

```
clear all
close all

%Load in the pressure data for each of the displacement tests
%Load sample type used in each test, 1 = 20Agilus80Vero, 2= 50AGilus50Vero,
%3= 80Agilus20Vero
load('ForceDirectContactPRESSURE+SAMPLETYPE05082020.mat')

% Specify the folder where the files live.
myFolder = 'C:\Users\Maarten\Documents\Tu Delft\BME (Master)\MEP
(afstuderen)\Graduation Project\Testing Files\DATA-failsRemoved\Force Testing';
% Check to make sure that folder actually exists.  Warn user if it doesn't.
if ~isfolder(myFolder)
    errorMessage = sprintf('Error: The following folder does not exist:\n%s
    \nPlease specify a new folder.', myFolder);
    uiwait(warndlg(errorMessage));
    myFolder = uigetdir(); % Ask for a new one.
    if myFolder == 0
         % User clicked Cancel
         return;
    end
end

a = 1;
b = 1;
bb = 1;
c = 1;
cc = 1;

% Get a list of all files in the folder with the desired file name pattern.
filePattern = fullfile(myFolder, '*.txt'); % Change to whatever pattern you need.
theFiles = dir(filePattern);
for k = 1 : length(theFiles)
    baseFileName = theFiles(k).name;
    fullFileName = fullfile(theFiles(k).folder, baseFileName);
    fprintf(1, 'Now reading %s\n', fullFileName);

    %load each individual measurement data set and extract the time and
    %displacement data
    singleTestDATA = load(fullFileName);
    %storing the time data from a single measurement in the time vector
    Time = singleTestDATA(:,1);
    %Converting the time vector to seconds instead of ms
    Time = Time/1000;
    %storing the displacement data of each single measurement in a vector
    Force = singleTestDATA(:,4);

    %correct measured force by removing the base force value, yields a force difference
    ForceCorrected = Force - Force(3);

    %apply a filter to the data to remove outliers and noise
%     coeff1sec = ones(1, 10)/10;
%     AVGFORCE10measurements = filter(coeff1sec,1,Force);
%     fDelay = (10-1)/2;

    FilteredData = medfilt1(ForceCorrected,10,'truncate');
```

```
Cutoffpoint = max(Time)/2; % cutoff point to filter out early peaks likely
occurring due to the PACE 5000 stabilizing the pressure at the set value.
IndexCut = find(Time > Cutoffpoint);
MaxForce(k)= max((FilteredData(IndexCut(1):end)));
MaxIndex = find(FilteredData == MaxForce(k));

%Plot each of the individual force measurements to examine them
if k == 101
Cutoffpoint = max(Time)/3; % cutoff point to filter out early peaks likely
occurring due to the PACE 5000 stabilizing the pressure at the set value.
IndexCut = find(Time > Cutoffpoint);
MaxForce(k)= max((FilteredData(IndexCut(1):end)));
MaxIndex = find(FilteredData == MaxForce(k));
end

if k == 160
figure
hold on
Frce = plot(Time,ForceCorrected);
Filtd = plot(Time,FilteredData);
Mx = plot(Time(MaxIndex),MaxForce(k),'ro');
title(sprintf(baseFileName))
xlabel('Time [s]')
ylabel('Force [N]')
legend([Frce(1) Filtd(1) Mx(1)],'Raw Data','Filtered Data','Max Force',
'location','northwest')
end


if SampleTypes(k) == 1
Agilus80VeroForce(a,1) = PressureValues(k);
Agilus80VeroForce(a,2) = MaxForce(k);

a = a+1;


elseif SampleTypes(k) == 2
Agilus50VeroForce(b,1) = PressureValues(k);
Agilus50VeroForce(b,2) = MaxForce(k);

b = b+1;

elseif SampleTypes(k) == 8
Agilus50VeroForce22(bb,1) = PressureValues(k);
Agilus50VeroForce22(bb,2) = MaxForce(k);

bb = bb+1;

elseif SampleTypes(k) == 6

Agilus20VeroForce21(c,1) = PressureValues(k);
Agilus20VeroForce21(c,2) = MaxForce(k);

c = c+1;

elseif SampleTypes(k) == 9
```

```
    Agilus20VeroForce22(cc,1) = PressureValues(k);
    Agilus20VeroForce22(cc,2) = MaxForce(k);

    cc = cc+1;

    end

end


figure
hold on
title('Pressure vs Max Force all Samples')
xlabel('Pressure [Pa]')
ylabel('Force [N]')

plot(Agilus80VeroForce(:,1),Agilus80VeroForce(:,2),'g*-')
plot(Agilus50VeroForce(:,1),Agilus50VeroForce(:,2),'r*-')
plot(Agilus50VeroForce22(:,1),Agilus50VeroForce22(:,2),'ro-')
plot(Agilus20VeroForce21(:,1),Agilus20VeroForce21(:,2),'b+-')
plot(Agilus20VeroForce22(:,1),Agilus20VeroForce22(:,2),'bo-')
legend('20Agilus80Vero','50Agilus50Vero','80Agilus20Vero-2.1','80Agilus20Vero-2.2',
'Location','southeast')
```

Calculations of theoretical force values.

```
%Material properties of TangoBlackPlus

%Large diaphragm
Dcl = 14*10^-3; % [m] Outside diameter large diaphragm
Dpl = 6.5*10^-3;  % [m] Piston diameter large diaphragm
(Thickened part is referred to as piston)
nDl = Dcl/Dpl;  % Ratio between piston diameter and the outer clamping diameter
Tdl = 2.3*10^-3;  % [m] Thickness of the large diaphragm

%Small diaphraagm
Dcs = 7*10^-3; % [m] Outside diameter small diaphragm
Dps = 3*10^-3; % [m] Piston diameter small diaphragm
nDs = Dcs/Dps; % Ratio between piston diameter and the outer clamping diameter
Tds = 1*10^-3; % [m] Thickness of the small diaphragm

%Pressure parameters
AmbientP = 101325;       % [Pa] Ambient atmospheric pressure

%Calculation of effective area of Large diaphragm
% Assumption to define the effective area is that the displacement is less
% than the diaphragm thickness and the diaphragm is clamped on the inner
% and outside edges.

Aeffl = (pi*((Dcl)^2)*((nDl^2)-1)*((nDl^4)-1-4*(nDl^2)*log(nDl)))/(12*(nDl^2)*
((nDl^4)-2*(nDl^2)+1-4*(nDl^2)*(log(nDl)^2)));

%Effective diaphragm surface contributing to the generated force.
Al2 = Aeffl - pi*((3/2000)^2);

%calculating the effective area according to giovanni et al. (large
%diaphragm)
Apl = (1/16)*(1-((1/nDl)^4)-(4*((1/nDl)^2)*log(nDl)));
Afl = (1/pi)*((((nDl^2)-1)/(4*nDl^2))-((log(nDl)^2)/((nDl^2)-1)));
```

```
Acl = (Afl/Apl)*pi*((Dcl/2)^2);
Acl2 = Acl - pi*((3/2000)^2) ;

Aml = pi*((((Dcl/2)+(Dpl/2))/2)^2);
Aml2 = Aml - pi*((3/2000)^2);

%calculating the conventional area of a round surface
AnL1 = (pi*((7/1000)^2));
AnL2 = (pi*((7/1000)^2)) - pi*((3/2000)^2);

%calculating the effective area according to giovanni et al. (small
%diaphragm)
Aps = (1/16)*(1-((1/nDs)^4)-4*((1/nDs)^2)*log(nDs));
Afs = (1/pi)*((((nDs^2)-1)/(4*nDs^2))-((log(nDs)^2)/((nDs^2)-1)));
Acs = (Afs/Aps)*pi*((Dcs/2)^2);
Acs2 = Acs - pi*((3/2000)^2) ;

Ams = pi*((((Dcs/2)+(Dps/2))/2)^2);
Ams2 = Ams - pi*((3/2000)^2);

%calculating the conventional area of a round surface
AnS1 =  (pi*((3.5/1000)^2));
AnS2 = (pi*((3.5/1000)^2)) - pi*((3/2000)^2);

%Pressure force relationship

Ppulse = [0 100000 200000 300000 400000 500000];


for i = 1:length(Ppulse)

Fnet(i) = (Acl2*Ppulse(i)-Acl*AmbientP)-(Acs2*Ppulse(i)-Acs*AmbientP);

end

%convert applied pressure to absolute pressure in chamber
AbsoluteP = Agilus80VeroForce(:,1) + AmbientP;
AbsoluteP2 = Agilus50VeroForce(:,1) + AmbientP;
AbsoluteP3 = Agilus20VeroForce21(:,1) + AmbientP;
AbsoluteP4 = Agilus20VeroForce22(:,1) + AmbientP;
AbsoluteP5 = Agilus50VeroForce22(:,1) + AmbientP;
```

Plotting of the figure that shows the theoretical force and the measured force.

```
figure
hold on
plot(Ppulse,Fnet,"k-")
plot(AbsoluteP5,Agilus50VeroForce22(:,2),'ro-')
plot(AbsoluteP3,Agilus20VeroForce21(:,2),'b+-')
plot(AbsoluteP4,Agilus20VeroForce22(:,2),'bo-')
plot(AbsoluteP,Agilus80VeroForce(:,2),'g*-')
plot(AbsoluteP2,Agilus50VeroForce(:,2),'r*-')
title('Pressure vs Developed force')
xlabel('Pressure [Pa]')
ylabel('Force [N]')
legend('Calculated Force','Measured Data 50Agilus50Vero-2.2','Measured Data
80Agilus20Vero-2.1','Measured Data 80Agilus20Vero-2.2','Measured Data
20Agilus80Vero','Measured Data 50Agilus50Vero','location','northwest')
```